

A TIME-DOMAIN PANEL METHOD FOR OSCILLATING  
PROPULSORS WITH BOTH CHORDWISE AND  
SPANWISE FLEXIBILITY

CENTRE FOR NEWFOUNDLAND STUDIES

**TOTAL OF 10 PAGES ONLY  
MAY BE XEROXED**

(Without Author's Permission)

PENGFEE LIU







A TIME-DOMAIN PANEL METHOD  
FOR OSCILLATING PROPULSORS WITH BOTH  
CHORDWISE AND SPANWISE FLEXIBILITY

By

Pengfei Liu, B. Eng., M. Eng., P. Eng.

A DISSERTATION  
SUBMITTED TO THE SCHOOL OF GRADUATE STUDIES  
IN PARTIAL FULFILLMENT OF THE REQUIREMENTS  
FOR THE DEGREE OF  
DOCTOR OF PHILOSOPHY

Faculty of Engineering & Applied Science  
Memorial University of Newfoundland  
St. John's, Newfoundland, Canada



National Library  
of Canada

Acquisitions and  
Bibliographic Services Branch

395 Wellington Street  
Ottawa, Ontario  
K1A 0N4

Bibliothèque nationale  
du Canada

Direction des acquisitions et  
des services bibliographiques

395, rue Wellington  
Ottawa (Ontario)  
K1A 0N4

Your file    Votre référence

Our file    Notre référence

The author has granted an irrevocable non-exclusive licence allowing the National Library of Canada to reproduce, loan, distribute or sell copies of his/her thesis by any means and in any form or format, making this thesis available to interested persons.

L'auteur a accordé une licence irrévocable et non exclusive permettant à la Bibliothèque nationale du Canada de reproduire, prêter, distribuer ou vendre des copies de sa thèse de quelque manière et sous quelque forme que ce soit pour mettre des exemplaires de cette thèse à la disposition des personnes intéressées.

The author retains ownership of the copyright in his/her thesis. Neither the thesis nor substantial extracts from it may be printed or otherwise reproduced without his/her permission.

L'auteur conserve la propriété du droit d'auteur qui protège sa thèse. Ni la thèse ni des extraits substantiels de celle-ci ne doivent être imprimés ou autrement reproduits sans son autorisation.

ISBN 0-612-13919-0

Canada

© Copyright 1996

by

Pengfei Liu, B. Eng., M. Eng., P. Eng.

To my teachers, including my parents, who enlightened, fostered,  
guided and instructed me, throughout kindergarten, primary school,  
high school and university

*Learning without thought is labour lost;  
thought without learning is perilous.*

Confucius

*The whole of science is nothing more than a refinement  
of everyday thinking.*

Albert Einstein

## Abstract

A time domain panel method was formulated and a computer program package, OSFBEM, was developed to evaluate the propulsive performance of oscillating propulsors.

This method was designed, and is able, to obtain hydrodynamic properties for an unsteady, 3-D flexible wing. A number of features were implemented including the geometry of both 2-D and arbitrary 3-D planforms; a non-zero thickness foil section and a section with a thickness as thin as 2% of the chord; large amplitude pitch and heave motions; non-zero trailing edge thickness; flexible motion and geometry parameters such as steady flow, unsteady motion, chordwise and spanwise flexibility; and prediction of skin friction and qualitative examination of sectional flow patterns in terms of boundary layer growth. Major limitations of this method include the inability to precisely predict separation, stall and hydrodynamic characteristics of a foil with a very small aspect ratio.

A large amplitude theory was developed and used to analyze the propulsive efficiency and thrust. An instantaneous angle of attack of the oscillating foil and a large amplitude feathering parameter were defined for this study. As a result of this theoretical establishment, the thrust was identified to be directly related to the instantaneous angle of attack. Most importantly, the best efficiency was obtained at the maximum instantaneous angle of attack of about  $10^\circ$ , for any combination of motion parameters and any shape of planforms with and without flexibility that were examined in this research.

Most previous numerical predictions on 3-D unsteady oscillating foils were based on the small amplitude theory. The present method, instead, is based on the finite amplitude theory and it also takes the sectional thickness distribution, planform shape and skin friction, etc., into account. Therefore, a parametric study was also conducted for rigid planforms to give results from a more realistic model.

The chordwise and spanwise flexibility were implemented by using a positive approach, i.e., different amplitudes of deflexion and shape functions were predetermined, to simulate a fin whale's flukes. Two non-dimensional parameters, the spanwise and

chordwise deflexion amplitude factors, together with another two parameters, the spanwise and chordwise deflexion phase angles relative to the pitch were defined. A parametric study was then conducted in terms of these parameters.

A numerical procedure was also established to determine the angle of zero lift for a foil due to the chordwise flexibility and, this angle of angle of zero lift was then used to modify the instantaneous pitch angle to obtain the instantaneous angle of attack at each time step. A numerical scheme was also formulated for foils with spanwise flexibility in calculating the efficiency in which case the heave amplitude had a variation across the span.

Major findings include the limitation and validity of the small amplitude theory obtained from a large amplitude analysis; determination of the instantaneous angle of attack of rigid and flexible oscillating foils; the relation between the maximum instantaneous angle of attack and the thrust; the instantaneous angle of attack for the best efficiency; sectional thickness ratio effect on efficiency and thrust; skin friction effect on the propulsive performance; pressure distribution and validity of the steady Kutta condition for an unsteady oscillating foil with both chordwise and spanwise flexibility; the chordwise and spanwise deflexion phase angles and their effects on the efficiency and thrust; and the effect of the spanwise deflexion amplitude on efficiency and thrust.

Conclusions were drawn from these predicted results and suggestions on the geometry and motion parameters in oscillating foil design were also made.

# Contents

Abstract	vi
List of Tables	xii
List of Figures	xiii
Acknowledgement	xx
Nomenclature and Abbreviations	xxii
<b>1 Introduction</b>	<b>1</b>
1-A Wings in the natural world and in engineering . . . . .	1
1-B Oscillating foils as an alternative to screw propellers . . . . .	5
1-B-1 About screw propellers . . . . .	5
1-B-2 Some marine oscillatory propulsors . . . . .	7
1-C Objective of this research . . . . .	11
1-D Perspective of this research program . . . . .	13
<b>2 Review of Literature</b>	<b>16</b>
2-A Historical Review . . . . .	16
2-A-1 Lifting surface theory . . . . .	17
2-A-2 Panel methods . . . . .	18
2-B Technical Review . . . . .	21
2-B-1 Three basic formulations . . . . .	22

2-B-2	The Kutta condition . . . . .	23
2-B-3	The uniqueness of the solution . . . . .	26
2-B-4	Wake considerations . . . . .	28
<b>3</b>	<b>Formulation of the method</b> . . . . .	<b>37</b>
3-A	Physical aspects of the lifting flow domain . . . . .	37
3-B	Formulation of the potential based panel method . . . . .	39
3-C	Numerical implementation . . . . .	44
3-C-1	The method of numerical solution . . . . .	44
3-C-2	The matrix solver . . . . .	53
3-C-3	Calculation of hydrodynamic forces . . . . .	55
3-C-4	Consideration of viscous effects and skin friction coefficient $C_f$ . . . . .	58
3-C-5	Efficiency and mean thrust calculation . . . . .	61
3-C-6	Computing considerations and the procedure . . . . .	62
<b>4</b>	<b>Results and discussion: convergence and computing efficiency</b> . . . . .	<b>68</b>
4-A	Panel density effects for a steady foil calculation . . . . .	69
4-B	Convergence study for an oscillating foil . . . . .	81
4-B-1	Computing efficiency and conservation of resources . . . . .	87
4-B-2	Summary . . . . .	87
<b>5</b>	<b>Results and discussion: verifications and comparisons</b> . . . . .	<b>89</b>
5-A	Pressure distribution and lift coefficient of a 2-D foil . . . . .	89
5-B	Pressure distribution at the tip of a 3-D foil . . . . .	91
5-C	Pressure distribution of a swept and tapered foil with 2% maximum thickness . . . . .	93
5-D	Efficiency and thrust from an oscillating foil . . . . .	95
<b>6</b>	<b>Results and discussion: parametric analysis for rigid planforms</b> . . . . .	<b>99</b>
6-A	A note on large amplitude theory . . . . .	101
6-B	Effect of heave amplitude on the efficiency and thrust . . . . .	105
6-C	Effect of apparent pitch amplitude on the efficiency and thrust . . . . .	108

6-D	Effect of pitching axis position factor on the efficiency and thrust . . .	111
6-E	Effect of phase angle on the efficiency and thrust . . . . .	112
6-F	Effect of sectional thickness on the efficiency and thrust . . . . .	114
6-G	Efficiency and thrust from a lunate planform . . . . .	116
6-G-1	Present method versus lifting surface theory for a man-made lunate tail . . . . .	118
6-G-2	Effect of the man-made lunate planform on efficiency and thrust	119
6-II	Efficiency and thrust from a fin whale's flukes . . . . .	121
6-II-1	Present method versus lifting surface theory for the flukes of a fin whale . . . . .	121
6-II-2	Effect of a natural lunate tail on efficiency and thrust . . . . .	124
6-I	Effect of skin friction on efficiency and thrust . . . . .	126
<b>7</b>	<b>Results and discussion: flexible oscillating foils</b>	<b>128</b>
7-A	Selection of chordwise and spanwise deflexion equations . . . . .	129
7-A-1	Deflexion equations for chordwise flexibility . . . . .	129
7-A-2	Deflexion equations for spanwise flexibility . . . . .	131
7-A-3	Determination of instantaneous effective angle of attack . . . . .	132
7-A-4	Graphical representation of fin whale flukes in motion . . . . .	134
7-B	Effect of the chordwise deflexion phase angle on efficiency and thrust	137
7-C	Effect of the spanwise deflexion phase angle on efficiency and thrust .	139
7-D	Effect of the chordwise deflexion amplitude on efficiency and thrust .	142
7-E	The effect of spanwise deflexion amplitude on efficiency and thrust . .	146
7-F	Propulsive performance of a rectangular flexible foil . . . . .	149
7-G	Propulsive performance of a fin whale's flukes . . . . .	153
<b>8</b>	<b>Conclusions</b>	<b>158</b>
8-A	About the method . . . . .	160
8-B	Verification of the method . . . . .	163
8-C	Large amplitude analysis and parametric study of a rigid oscillating propeller . . . . .	164

8-D About flexible oscillating planforms . . . . .	168
<b>References</b>	<b>171</b>
<b>Appendices</b>	<b>179</b>
<b>A Determination of doublet/source coefficient matrices</b>	<b>179</b>
<b>B Graphical presentation of some oscillating propellers in motion</b>	<b>191</b>
B-A Instantaneous positions and wake paths of a fin whale's flukes . . . . .	191
B-B Variation of phase angle of chordwise deflexion . . . . .	204
B-C Variation of phase angle of spanwise deflexion . . . . .	208
B-C-1 Small change in phase angle for a rectangular foil . . . . .	208
B-C-2 Large change in spanwise deflexion phase angle for a fin whale's flukes . . . . .	212
<b>Bibliography</b>	<b>220</b>

# List of Tables

1.1	Speeds of some of the fastest on-the-wing animals . . . . .	2
6.1	Comparison of the maximum instantaneous angle of attack . . . . .	103
6.2	Results of changing the heave amplitude . . . . .	106
6.3	Results of changing the apparent pitch amplitude . . . . .	108
6.4	Advance ratio $J$ versus other motion parameters for a fin whale's flukes	122
7.1	Comparison of nineteen combinations of deflexion equations . . . . .	135
7.2	Determination of an appropriate pitch amplitude for the flexible planforms . . . . .	154
7.3	Propulsive performance of the fin whale's flukes without an active control of spanwise deflexion . . . . .	155
7.4	Propulsive performance of the fin whale's flukes with an active control	155
A.1	Offsets of a 3-D body . . . . .	180

# List of Figures

1.1	Insect fly mechanism . . . . .	3
1.2	Sculling propulsion . . . . .	7
1.3	Schematic diagrams of a trochoidal propeller in operation . . . . .	9
1.4	Some shapes and sections of cetacean fluke planforms . . . . .	10
1.5	A trace of a sinusoidally oscillating foil . . . . .	10
2.1	A foil with a wake vortex sheet in a lifting flow . . . . .	24
2.2	Presentation of shed vortices due to variation of circulation around a foil section . . . . .	30
2.3	Generation of the trailing vortices due to variation of the spanwise circulation . . . . .	33
2.4	Formation of vortex rings by bound vortices, trailing vortices and starting vortices of a 3-D steady foil . . . . .	34
2.5	Shed vortices of a 3-D foil due to variation of the instantaneous circulation	35
2.6	Schematic diagram of a vortex sheet roll-up process for a 3-D foil in a steady flow . . . . .	36
3.1	Boundary conditions of velocity potential and normal velocity . . . .	41
4.1	The panel geometry of a 3-D foil . . . . .	69
4.2	The foil with its shed wake . . . . .	70
4.3	The instantaneous foil positions in motion at each time step. . . . .	70
4.4	$C_l$ convergence behaviour of the chordwise intervals at a fixed number of the spanwise intervals at NSpInt=6 . . . . .	71

4.5	$C_{di}$ and $C_m$ convergence behaviour of the chordwise intervals at a fixed number of the spanwise intervals at NSpInt=6 . . . . .	71
4.6	$C_l$ convergence behaviour of the spanwise intervals at a fixed number of the chordwise intervals at NChInt=6 . . . . .	71
4.7	$C_{di}$ and $C_m$ convergence behaviour of the spanwise intervals at a fixed number of the chordwise intervals at NChInt=6 . . . . .	72
4.8	$C_l$ convergence behaviour of the chordwise intervals at a fixed number of the spanwise intervals at NSpInt=10 . . . . .	72
4.9	$C_{di}$ and $C_m$ convergence behaviour of the chordwise intervals at a fixed number of the spanwise intervals at NSpInt=10 . . . . .	73
4.10	$C_l$ convergence behaviour of the spanwise intervals at a fixed number of the chordwise intervals at NChInt=10 . . . . .	73
4.11	Time convergence behaviour with regard to the number of time steps and the time step size . . . . .	74
4.12	$C_{di}$ and $C_m$ convergence behaviour of the spanwise intervals at a fixed number of the chordwise intervals at NChInt=10 . . . . .	74
4.13	$C_l$ convergence behaviour of the number of the chordwise intervals the same as the spanwise intervals . . . . .	75
4.14	$C_{di}$ and $C_m$ convergence behaviour of the number of the chordwise intervals the same as the spanwise intervals . . . . .	75
4.15	$C_l$ convergence behaviour of the number of cosine chordwise intervals the same as the number of the uniform spanwise intervals . . . . .	76
4.16	$C_{di}$ and $C_m$ convergence behaviour of the number of cosine chordwise intervals the same as the number of the uniform spanwise intervals . . . . .	76
4.17	$C_l$ convergence performance of NSpInt(uniform)=2.4*NChInt(cosine)	77
4.18	$C_{di}$ and $C_m$ at NSpInt(uniform)=2.4*NChInt(cosine) . . . . .	77
4.19	A log spacing arrangement for a rectangular foil with an aspect ratio of 3 . . . . .	78
4.20	Instantaneous position of an oscillating foil: side view . . . . .	81

4.21	Instantaneous position and panel geometry of an oscillating foil: perspective view . . . . .	82
4.22	An oscillating foil with its shed wake in fluid. . . . .	82
4.23	Time convergence study of the efficiency $\eta$ and the thrust coefficient $C_t$ vs. the total number of time steps . . . . .	85
4.24	The efficiency $\eta$ and the thrust coefficient $C_t$ vs. the total number of panels . . . . .	86
4.25	Required DRAM and elapsed time vs. the total number of panels . . . . .	87
5.1	Verification of pressure distribution for a NACA 0012 foil section . . . . .	90
5.2	Verification of pressure distribution. . . . .	91
5.3	A 3-D surface panel geometry of a swept wing . . . . .	93
5.4	Verification of pressure distribution on a swept wing. . . . .	94
5.5	Comparison of lifting surface theory and the present panel method in calculating efficiency . . . . .	95
5.6	Comparison of lifting surface theory and present panel method in calculating the thrust coefficient . . . . .	96
6.1	A graphical explanation of the instantaneous angle of attack using a large amplitude theory . . . . .	101
6.2	Effect of heave amplitude on the propulsive efficiency and thrust . . . . .	105
6.3	Effect of the apparent pitch amplitude on the propulsive efficiency and thrust . . . . .	109
6.4	Effect of pitching axis position factor on the propulsive efficiency and thrust . . . . .	111
6.5	Effect of phase angle on the propulsive efficiency and thrust . . . . .	112
6.6	Effect of sectional thickness on the propulsive efficiency and thrust . . . . .	114
6.7	3-D geometry of a man-made lunate planform . . . . .	116
6.8	Efficiency of a man-made lunate planform with an aspect ratio of 8 . . . . .	118
6.9	Thrust of a man-made lunate planform with an aspect ratio of 8 . . . . .	119
6.10	Efficiency $\eta$ of a man-made lunate planform and a rectangular oscillating foil . . . . .	119

6.11	Thrust coefficient of a man-made lunate planform and a rectangular oscillating foil . . . . .	120
6.12	Three dimensional geometry of a fin whale's flukes . . . . .	121
6.13	Propulsive efficiency of rigid fin whale's flukes . . . . .	122
6.14	Thrust coefficient of rigid fin whale's flukes . . . . .	123
6.15	Efficiency of the flukes of a fin whale and a rectangular oscillating foil . . . . .	124
6.16	Thrust coefficient of the flukes of a fin whale and a rectangular oscillating foil . . . . .	124
6.17	Effect of skin friction on efficiency of a rectangular oscillating foil with an aspect ratio of 8 . . . . .	126
6.18	Effect of skin friction on thrust of a rectangular oscillating foil with an aspect ratio of 8 . . . . .	126
6.19	Effect of skin friction on efficiency of a lunate oscillating foil with an aspect ratio of 8 . . . . .	127
6.20	Effect of skin friction on thrust of a lunate oscillating foil with an aspect ratio of 8 . . . . .	127
7.1	Shapes of chordwise deflexions determined by six equations . . . . .	130
7.2	Shapes of spanwise deflexions determined by five equations . . . . .	131
7.3	Effect of the chordwise deflexion phase angle $\Phi_c$ on the efficiency $\eta$ and the thrust coefficient $C_t$ . . . . .	137
7.4	Effect of the spanwise deflexion phase angle on $\eta$ and $C_t$ . . . . .	140
7.5	Effect of the chordwise deflexion factor on $\eta$ and $C_t$ . . . . .	142
7.6	Pressure distribution at zero chordwise deflexion . . . . .	143
7.7	Pressure distribution $C_p$ at a 20% chordwise deflexion . . . . .	145
7.8	Pressure distribution $C_p$ at a 28% chordwise deflexion . . . . .	145
7.9	Effect of the spanwise deflexion factor on $\eta$ and $C_t$ . . . . .	147
7.10	Effect of the spanwise deflexion factor and the phase angle on $\eta$ and $C_t$ . . . . .	147
7.11	Efficiency of a rectangular rigid/elastic propulsor calculated by different approaches . . . . .	149

7.12	Thrust coefficient of a rectangular propulsor calculated by different approaches . . . . .	150
7.13	Comparison of the instantaneous angle of attack, lift and thrust between a rigid and flexible (5% chord) rectangular foil . . . . .	150
7.14	Comparison of the instantaneous angle of attack, lift and thrust between a rigid and flexible (2% chord) rectangular foil . . . . .	151
7.15	Pressure distribution of a fin whale's flukes at $\Phi_s = -30^\circ$ and $t = 17.4948$ sec (the 240th time step) . . . . .	156
7.16	Pressure distribution of a fin whale's flukes at $\Phi_s = 180^\circ$ and $t = 37.5$ sec 157	
A.1	Schematic diagram for coordinate transformation from the global frame to the panel local frame. . . . .	181
B.1	Deflexion of a fin whale's flukes by a combination of C0 and S0 . . .	193
B.2	Deflexion of a fin whale's flukes by a combination of C1 and S1 . . .	193
B.3	Deflexion of a fin whale's flukes by a combination of C1 and S2 . . .	194
B.4	Deflexion of a fin whale's flukes by a combination of C1 and S3 . . .	194
B.5	Deflexion of a fin whale's flukes by a combination of C2 and S1 . . .	195
B.6	Deflexion of a fin whale's flukes by a combination of C2 and S2 . . .	195
B.7	Deflexion of a fin whale's flukes by a combination of C2 and S3 . . .	196
B.8	Deflexion of a fin whale's flukes by a combination of C3 and S1 . . .	196
B.9	Deflexion of a fin whale's flukes by a combination of C3 and S2 . . .	197
B.10	Deflexion of a fin whale's flukes by a combination of C3 and S3 . . .	197
B.11	Deflexion of a fin whale's flukes by a combination of C4 and S1 . . .	198
B.12	Deflexion of a fin whale's flukes by a combination of C4 and S2 . . .	198
B.13	Deflexion of a fin whale's flukes by a combination of C4 and S3 . . .	199
B.14	Deflexion of a fin whale's flukes by a combination of C5 and S1 . . .	199
B.15	Deflexion of a fin whale's flukes by a combination of C5 and S2 . . .	200
B.16	Deflexion of a fin whale's flukes by a combination of C5 and S3 . . .	200
B.17	Deflexion of a fin whale's flukes by a combination of C6 and S1 . . .	201
B.18	Deflexion of a fin whale's flukes by a combination of C6 and S2 . . .	201
B.19	Deflexion of a fin whale's flukes by a combination of C6 and S3 . . .	202

B.20 Path of the flukes with their wake by deflexion equations $C0$ and $S0$ .	202
B.21 Path of the flukes with their wake by deflexion equations $C1$ and $S1$ .	203
B.22 Path of the flukes with their wake by deflexion equations $C1$ and $S2$ .	203
B.23 Instantaneous positions of a rectangular foil with a semichord deflexion at $0^\circ$ phase lag . . . . .	205
B.24 Instantaneous positions of a rectangular foil with a semichord deflexion at $-20^\circ$ phase lag . . . . .	205
B.25 Instantaneous positions of a rectangular foil with a semichord deflexion at $-40^\circ$ phase lag . . . . .	206
B.26 Wake and path of a rectangular foil with a semichord deflexion at $0^\circ$ phase lag . . . . .	206
B.27 Wake and path of a rectangular foil with a semichord deflexion at $-20^\circ$ phase lag . . . . .	207
B.28 Wake and path of a rectangular foil with a semichord deflexion at $-40^\circ$ phase lag . . . . .	207
B.29 Instantaneous positions of a rectangular foil with a spanwise deflexion at $0^\circ$ phase lag . . . . .	209
B.30 Instantaneous positions of a rectangular foil with a spanwise deflexion at $-30^\circ$ phase lag . . . . .	209
B.31 Instantaneous positions of a rectangular foil with a spanwise deflexion at $-50^\circ$ phase lag . . . . .	210
B.32 Wake and path of a rectangular foil with a spanwise deflexion at $0^\circ$ phase lag . . . . .	210
B.33 Wake and path of a rectangular foil with a spanwise deflexion at $-30^\circ$ phase lag . . . . .	211
B.34 Wake and path of a rectangular foil with a spanwise deflexion at $-50^\circ$ phase lag . . . . .	211
B.35 Instantaneous positions of a fin whale's flukes with a spanwise deflexion at $-180^\circ$ phase angle . . . . .	213

B.36 Instantaneous positions of a fin whale's flukes with a spanwise deflexion at $-120^\circ$ phase angle . . . . .	213
B.37 Instantaneous positions of a fin whale's flukes with a spanwise deflexion at $-60^\circ$ phase angle . . . . .	214
B.38 Instantaneous positions of a fin whale's flukes with a spanwise deflexion at $0^\circ$ phase angle . . . . .	214
B.39 Instantaneous positions of a fin whale's flukes with a spanwise deflexion at $60^\circ$ phase angle . . . . .	215
B.40 Instantaneous positions of a fin whale's flukes with a spanwise deflexion at $120^\circ$ phase angle . . . . .	215
B.41 Instantaneous positions of a fin whale's flukes with a spanwise deflexion at $180^\circ$ phase angle . . . . .	216
B.42 Wake and its path of a fin whale's flukes with a spanwise deflexion at $-180^\circ$ phase angle . . . . .	216
B.43 Wake and its path of a fin whale's flukes with a spanwise deflexion at $-120^\circ$ phase angle . . . . .	217
B.44 Wake and its path of a fin whale's flukes with a spanwise deflexion at $-60^\circ$ phase angle . . . . .	217
B.45 Wake and its path of a fin whale's flukes with a spanwise deflexion at $0^\circ$ phase angle . . . . .	218
B.46 Wake and its path of a fin whale's flukes with a spanwise deflexion at $60^\circ$ phase angle . . . . .	218
B.47 Wake and its path of a fin whale's flukes with a spanwise deflexion at $120^\circ$ phase angle . . . . .	219
B.48 Wake and its path of a fin whale's flukes with a spanwise deflexion at $180^\circ$ phase angle . . . . .	219

## Acknowledgment

I wish to express my sincere appreciation to my major professor, Dr. Neil Bose, for his initiation of the research project and for his help and guidance in my graduate career. He also provided partial support of software and hardware to the computing facilities, which enabled me to finish this research project timely.

I am grateful to the members of the PhD Supervisory Committee, Professors M.R. Haddara and D. Bass, for their instructions and comments in the course of my graduate study.

Professor Xiuheng Wu and Qian GuiJun at Wuhan Jiao Tong University are also acknowledged for their encouragement.

Thanks are extended to Eastern College, Burin Campus for providing me an engineering technology teaching position. In past four years, campus professional development and teaching duties substantially improved my computer software and hardware skills; the remuneration enabled me to purchase books and the major computing equipment so that I was able to conduct the research away from the University; the computer facilities on the College's campus were also helpful.

The educational network in this province, the *Stem ~ Net*, provided me with an access to the Internet and a series of professional seminars, which were very helpful to the research work. I am grateful to its staff.

I thank Dr. Min Hu, at the Department of Computer Science, University of Toronto, Dr. Qi Xu, who formerly worked with the IMD of the NRC in St. John's, Mr. Michael Vest, a doctoral student under Professor J. Katz at San Diego State University, and Mr. Jim Fraser under Brian Maskew at Analytical Methods Inc., for their discussions or information, at the beginning of this project.

In past years, many friends and colleagues, including Mr. Sandy Donahue, the former Supervisor of Instruction of the College, have kindly provided me with a variety of assistance in many different ways in the course of the thesis; I would like to thank them too.

I am deeply indebted to my son, Ming, for his love and a long term support.

Since five years ago at the age of six, Ming has been sitting next to me in front of the computer watching me doing the work, in the evenings. Ming has done a huge amount of work in proofreading and in helping to program and plot the graphics. I am also grateful to my wife Lihua, for her continuous love, encouragement and support.

# Nomenclature and Abbreviations

## Nomenclature

$A_{foil}$	...	area of the wing
$S$	...	span of the wing
$C_r$	...	root chord length, also the reference length
$M$	...	aspect ratio of the wing, $M = S^2/A_{foil}$
$V_{flight}$	...	foil forward swim speed (m/sec)
$V_{flight}^*$	...	normalized foil forward swim speed (1/sec)
$\vec{V}_{trans}$	...	kinematic velocity due to translation of the foil
$\vec{V}_{rot}$	...	kinematic velocity due to revolution about the pitching axis
$\vec{V}_{flex}$	...	kinematic velocity due to deflexion of a flexible foil
$\vec{V}_{\infty}$	...	total kinematic velocity of a panel ( $\vec{V}_{\infty} = \vec{V}_{trans} + \vec{V}_{rot} + \vec{V}_{flex}$ )
$\vec{V}_{doub}^*$	...	perturbation velocity due to a unit doublet on foil body panel
$\vec{V}_{wake}^*$	...	perturbation velocity due to a unit doublet on shed wake panel
$\vec{V}_{source}^*$	...	perturbation velocity due to a unit source on foil body panel
$\omega$	...	frequency of the oscillation in rad/sec.
$k$	...	reduced frequency, $k = \omega C_r / V_{flight} = \omega / V_{flight}^*$
$h_{heave}$	...	heave amplitude
$h_o$	...	non-dimensional heave amplitude $h_o = h_{heave} / C_r$
$\alpha$	...	instantaneous pitch angle referred to the horizon
$\alpha_o$	...	absolute angular amplitude of pitch
$\alpha_{zro}$	...	angle of zero lift of a section due to chordwise flexibility
$\alpha_v$	...	instantaneous angle of the kinematic velocity of the pitching axis, $\alpha_v = [\tan^{-1}(\omega h_o \sin[\omega t - \Phi_{phase}] / V_{flight}^*)]$
$\alpha_{instant}$	...	instantaneous angle of attack $\alpha_{instant} = \alpha_v - \alpha$
$\alpha_{instant,max}$	...	maximum instantaneous angle of attack
$\theta$	...	small amplitude feathering parameter, $\theta = \alpha_o V_{flight}^* / \omega h_o$
$\Theta$	...	large amplitude feathering parameter, $\Theta = \alpha_o [\tan^{-1}(\omega h_o / V_{flight}^*)]$
$\Theta_{instant}$	...	instantaneous large amplitude feathering parameter,

		$\Theta_{instant} = \alpha/\alpha_v$
$J$	...	advance ratio, $J = \pi V_{flight}^* / \omega h_a = \pi / [kh_a] = \theta\pi/\alpha_o$
$J^*$	...	flexible foil advance ratio, $J^* = \frac{V_{flight}}{\omega C_r}$
$\Phi_{phase}$	...	phase angle (pitch leading heave)
$\Phi_c$	...	phase angle (chordwise deflexion relative to pitch)
$\Phi_s$	...	phase angle (spanwise deflexion relative to pitch)
$\delta_{co}$	...	chordwise deflexion amplitude factor based on chord
$\delta_{so}$	...	spanwise deflexion amplitude factor based on half span $l = S/2$
$x, y, z$	...	Cartesian coordinates moving with the wing
$\rho$	...	mass density of the fluid
$\mu$	...	viscosity of the fluid
$Re$	...	Reynolds number, $Re = \rho V_{flight} C_r / \mu$
$\gamma(x, y)$	...	circulation at control point
$\Gamma(y)$	...	sectional or total circulation
$\Phi$	...	constant doublet velocity potential
$C_p$	...	pressure coefficient at panel control point
$c_l$	...	sectional lift coefficient
$c_m$	...	sectional pitching moment coefficient
$c_t$	...	sectional thrust coefficient
$C_t$	...	mean total thrust coefficient
$C_{L_i}$	...	lift coefficient at the $i$ -th time step
$C_M$	...	instantaneous pitching moment coefficient
$C_T$	...	transient thrust coefficient
$\eta$	...	propulsive efficiency
NChInt	...	number of the chordwise panel intervals
NSpInt	...	number of the spanwise panel intervals
NTSM	...	number of time steps in motion

## Other Abbreviations

NACA	...	United States National Advisory Committee for Aeronautics
NASA	...	United States National Aeronautics and Space Administration
FEM	...	finite element method
FDM	...	finite difference method
BEM	...	boundary element method
P.D.E.	...	partial differential equation
L.P.D.E.	...	linear partial differential equation
LHS	...	the left-hand-side of a linear equation system
RHS	...	the right-hand-side of a linear equation system
DRAM	...	dynamic random access memory
Mb	...	megabytes, $1 Mb = 2^{10} \cdot 2^{10} = 1,048,576$ bytes
MB	...	motherboard, mainboard
OSF/BEM	...	oscillating foil boundary element method, a Fortran 77 program written for fulfilling the computing tasks for this research program
CISC	...	complex instruction-set computing
RISC	...	reduced instruction-set computing
DXF	...	drawing exchange file

# Chapter 1

## Introduction

### 1-A Wings in the natural world and in engineering

Birds fly and fish swim. They are on-the-wing creatures. In the flapping flight of birds and insects, wings provide both lift and thrust to their bodies; when gliding, wings act as a lifting device. In the aquatic kingdom, flukes of a whale power the motion, while dorsal fins and pectoral fins help to control the course of the navigation. Penguins use flapping flippers; so do sea lions.

There are some extraordinary facts recorded on these animals. These facts though questionable in reliability (Matthews et al. 1993), present a perspective on the speed categories of certain on-the-wing creatures (Table 1.1). In air, the smallest, but one of the greatest fliers, the bee hummingbirds (*Mellisuga helenae*), measuring only three inches to four inches from bill to tail, have a wing beating rate of fifty-five to seventy-five times a second. This so called “acrobat” in the bird world has high manoeuvrability at high speed in darting and dipping. However, the fastest fliers are the peregrine falcons (*Falco peregrinus*): at a  $30^\circ$  angle of descent and a  $45^\circ$  angle of ascent, their maximum velocity reaches 168 mph (270 km/h) and 217 mph (349 km/h) respectively. In level flight, the fastest creatures are those from the duck and

On-The-Wing Animals		speed (mph)	speed (knots)	condition of flight
Birds	Blue Hummingbird	superior manoeuvrability		
	Peregrine Falcon	168/217	146/188	30° descent/45° ascent
	Duck, Goose	65	56	level flight
Insects	Hawkmoth, Horsefly	24	21	maintainable speed
	Australian Dragonfly	36	31	burst speed
Aquatic Animals	Bull Killer Whale	34.5	30 knots	burst speed
	Cosmopolitan Sailfish	68	60 knots	burst speed
Fastest on-the-leg animal, cheetah		60	52 knots	burst speed

Table 1.1: Nautical speeds of some fastest on-the-wing animals, after Matthews et al. (1993)

goose families. These powerful animals can fly at a speed of 65 mph (104 km/h). In the insect world, hawkmoths (*Sphingidae*) and horseflies (*Tabanus bovicus*) are able to maintain a speed of 24 mph (39 km/h); the burst speed of the Australian dragonfly (*Austriophlabia costalis*) reaches 36 mph (58 km/h). In the ocean, fast swimmers include whales and dolphins, and some lunate-tailed fishes such as the shark, tuna and sailfish. A 20 ft (6 m) long bull killer whale (*Orcinus orca*) was recorded swimming at a speed of 34.5 mph (30 knots). Surprisingly, the fastest on-the-wing swimmer in the water is even faster than the highest speed “on-the-legs” animal on land: a cosmopolitan sailfish (*Istiophorus platypterus*) can swim at a highest speed of 68 mph (110 km/h) over a short distance, while a cheetah (*Acinonyx jubatus*) runs at maximum speed of 60 mph (97 km/h) for a short while.

These biological facts in the living world are interesting and are probably one of the motives behind bio-mechanical studies. In adapting to their environment, birds, insects, marine mammals and fishes have different wing structures and therefore varied manoeuvrability and speed. Different wing-body structures lead to a different wing-control mechanism. Usually, fast and high manoeuvrability birds have a larger wing to body ratio (the ratio of the area of the wing to the weight of the body). Birds in hovering flight have an ornithopter mechanism. Long distance travelling birds

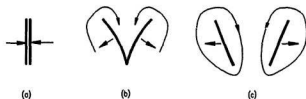


Figure 1.1: Insect fly mechanism after Acheson (1990). (a) clap, (b) fling (c) parting of the wings. The thick arrows stand for the motion of the wings and the thin curved arrows denote the circulation.

often have a higher wing aspect ratio to obtain larger lift/drag ratio and therefore a smaller wing area to save muscle power. The smaller wing area and higher sweep angle at the leading edge also have less drag, especially in glide flight (van Dam 1986): Arctic terns<sup>1</sup> and swallows are examples. On the other hand, some insects have quite different wing-body combinations and hence a special wing-control mechanism. The Weis-Fogh mechanism (Acheson 1990) was derived from the hovering motion of a chalcid wasp (*Encarsia formosa*). The sequence of the Weis-Fogh mechanism is clap, fling and parting (see figure 1.1). In flight, the span of wings is more parallel than perpendicular to the motion. Underwater, swimming is another story. Most fast aquatic animals have propulsors of large aspect ratio with a high sweep angle (called lunate-tail swimmers). These swimmers are distinguished by their mode of propulsion. Unlike those that undulate their body to generate thrust, and the other modes such as carangiform (Hoar and Randall 1978): where both the body and tail contribute to propulsion; fast swimmers manoeuvre their flukes or tails in a thuniform mode (the sub-mode of the carangiform). In swimming, the majority of their bodies remain straight with only the rear part in oscillation. The thuniform mode of propulsion is widely recognized as the best form for high efficiency (Lai 1990).

Bio-mechanical remarkableness provides a clue in human being's simulation and

<sup>1</sup>The Arctic terns (*Sterna paradisica*) are recorded as the longest distance fliers. An Arctic tern was timed in a flight covering a distance of 14,000 miles (22,500 kilometres) over about a 10-month time period.

invention. One of the best examples of simulating natural phenomena in engineering is probably the first airplane built by the Wright brothers in 1903. Examples of wing theory in engineering applications are many: wings are pure lifting devices for airplanes; blades of turbines and windmills serve as torque absorbers and thus energy transformers; blades of screw propellers, cycloidal propellers, foils of oscillating propellers, sails and sculls are thrust generators. Rudders on ships control the course of travel and Magnus effect cylinders<sup>2</sup> pushing a vessel are also wing theory applications. A successful recent wing theory application is the wing-in-ground effect wingship. With 30 tons of payload, and flying over wavetops, this kind of flyer (see the *Orlyonok* described by Dane, 1992) could reach 250 mph (400 km/h) like a jetliner but has a fuel cost as low as the same sized steam ship.

Application of wing theory to marine transportation has its own economical importance. Compared with a commercial aircraft or a land container truck, an ocean cargo carrier is superior in terms of ton-mileage cost, especially in cargoes consisting of massive bulk quantities or huge packed volume, though there is still much room to improve energy efficiency. On the other hand, the cost of propulsion is a major cost in water transportation and the screw propeller has long had a main role in marine propulsion. Nevertheless, it is difficult to improve efficiency of screw propellers, because the maximum efficiency for any kind of propulsor is dependent upon its mode or nature of propulsion: different propulsion modes result in different ranges of loading conditions; the higher the load of a propulsor, the lower the highest possible efficiency. For a screw propeller, as it is highly loaded in most cases, this peak value is about 70% to 80% and most marine propellers are working at about 50% efficiency. Therefore, scientists and marine engineers have put forward many alternatives for propulsion devices, including some oscillatory propulsors.

---

<sup>2</sup>The Magnus effect is derived from the circulation theorem based on wing theory (Acheson 1990). An authentic application of this effect may be described as: "At the coming 1933 World's Fair, we were told, the wind would whip across Lake Michigan to drive three rotating wings on a 70-ft. cabin cruiser. Mounted like masts, the 25-ft.-high aluminum rotors would provide four times the propulsion power of conventional sails and act as stabilizers in choppy water. After the sunset, coloured lights splashed across the spinning rotors, offering a scintillating effect, visible for miles." *Popular Mechanics*, June 1933.

## 1-B Oscillating foils as an alternative to screw propellers

For on-the-wing animals, wing-body structure determines the wing-control mechanism, hence the manoeuvrability, speed and required muscle power; in propulsor design, different wing structures need different motion control devices to obtain a desired propulsion mode. A good marine propulsor under specified working conditions generally has both large thrust (coefficient) and efficiency (the ratio of useful power to input power), though in most cases increasing the thrust lowers the efficiency and vice versa. A propeller having very high efficiency but little thrust will not be useful at all; a propeller having high thrust with poor efficiency will result in an unaffordable operating cost. Increasing both thrust and efficiency (with the consideration of noise, vibration and environmental issues) is the main focus of the development of propulsion technology.

### 1-B-1 About screw propellers

Since the invention of the steam engine and screw propeller in the eighteenth and nineteenth century respectively<sup>3</sup>, tremendous efforts have been made to improve the propulsive performance of the propulsors of marine vehicles. Studies in this area have been both theoretical and experimental. In the past century, many studies of propulsive devices have been done and some of these devices have been installed in ship propulsion systems. Among a number of propulsors studied, the screw propeller has proved to be the most energy efficient. However, the efficiency of many ordinary screw propellers is about fifty to sixty percent, especially those on smaller vessels. In a few cases, the propulsive efficiency of the screw propeller may reach as high as 70 percent. Searching for a high efficiency propeller is a problem that still remains,

---

<sup>3</sup>According to Johnson et al. (1989), the modern condensing and double-acting steam engine was invented by James Watt in 1782, following the atmospheric steam engine by Thomas Newcomen in 1705 and the pumping-water steam engine by Savery Newcomen; the first steamship was invented by Claude de Jouffroy d'Abbans, 1783 and the first screw propeller was invented independently by Sir Francis P. Smith in 1836 and John Ericsson, 1837.

and previous studies have shown that the efficiency of a screw propeller will not increase greatly unless the propulsion mode is changed, because of certain limitations in propeller design.

These limitations on the propulsive efficiency from a screw propeller for a required amount of thrust include the following.

- As thrust is achieved by rotating the blades to obtain the inflow velocity for the wing sections, the rotation of the blades causes a number of problems.
  1. The wake at the trailing edge is in a helical form, and the whole wake of the propeller is rotating. Rotational energy losses occur behind the propeller. Some techniques can be applied to reduce these kinds of energy loss (Lee et al. 1990) such as coaxial contrarotating propellers, propellers with free-running vane wheel, preswirl devices and postswirl devices. There is no solution which completely eliminates these energy losses.
  2. As the blade of a screw propeller is radially placed, the inflow velocity varies spanwise. According to the flow conditions, the geometry of the propeller, and the thrust requirement, a larger pitch angle is required at the root of the blade and vice versa at the tip of the blade. It is known that the efficiency is restricted in propeller design: the angle of attack at the root section cannot be as large as it should be due to the separation at the trailing edge; the angle of attack at the tip has to be close to zero degrees to avoid cavitation (Lee et al. 1990).
  3. The blade of a screw propeller is a kind of low aspect ratio wing. The lift/drag ratio is small for low aspect ratio wings. Better efficiency is expected for wings with a high aspect ratio. The geometry limitations at the stern of a ship place a restriction on diameter and do not allow large aspect ratio blades. Ducted propellers increase the efficiency under heavy load conditions; however, these do not eliminate the aspect ratio problem, as a gap exists between the blade tip and the duct.

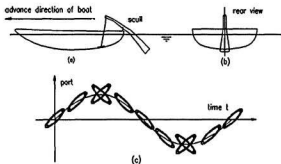


Figure 1.2: Sculling propulsion. (a) a scull in a boat from side view, (b) a scull at the stern of a boat from rear view and (c) sinusoidal motion of the scull in propulsion (plan view)

- As the blades are solid and the loading conditions like a cantilever beam in deflection and torsion, certain related structural problems exist.
  1. The root blade sections have to be very thick to balance the spanwise deflection loading and the torsional moment between the hydrodynamical centre and the elastic axis. Too much thickness reduces the efficiency of the foil and adds drag to the propulsor.
  2. The blade vibrates due to the fluctuating pressure caused by uneven flow velocity distribution at the vicinity of the propeller. If the frequency of the fluctuating pressure is close to the natural frequency of the blade, resonance will occur. Besides the structural strength (repeating, shock loads, and fatigue etc.) concerns, the stern wake pattern has to be improved and sometimes the optimized rotational speed and the geometry parameters of a propeller have to be sacrificed to reduce the noise and vibration due to shaft excitation. This also constrains the achievement of the maximum possible efficiency.

## 1-B-2 Some marine oscillatory propulsors

The scull was probably the earliest oscillating propulsor. Being vertically fixed at the stern of a boat, a scull creates thrust by sculling the water sideways, periodically back and forth. In sculling motion, both the sway and the yaw of a scull have an oscillatory variation with time. Oscillation of a scull gives a high propulsive efficiency, possibly the highest among all propulsion devices (Potze 1986); efficiency in an ideal fluid was calculated to be above 90% when two sculls with an aspect ratio of four were fixed at the stern of a ship. Figure 1.2 shows the motion of a manually operated scull. The motion of the scull is a form of oscillating foil propulsion. However, the motion of the manually operated scull shown in figure 1.2 is different from the descriptions of oscillating propellers found in most existing publications. The difference is that the wing planform in sculling motion will alternatively change its leading edge and trailing edge. Another difference is the spanwise sway oscillation, i.e., the inflow velocity is different at the leading edge along the span. So far, a systematic study for this kind of propulsion has not been conducted. A mechanically driven scull has not been developed. Manually operated scull boats are popular in Eastern Asia, such as on the north-east coast of China and in Japan.

The trochoidal propeller is another example of oscillating foil propulsion. This propulsor is also called a vertical axis propeller, though it can also be mounted horizontally on a ship. Operation diagrams are presented in figure 1.3.

Figure 1.3 *a* shows the side view of the propeller. The blades are installed perpendicular to the horizontal. In figure 1.3 *b*, the base rotates while the blades are pitching. Rotation of the base, the magnitude of the pitch and heave, together with the oscillating frequency, are adjusted to enable the blades to have an appropriate angle of attack for the best thrust and efficiency. Thrust is obtained from the forward force component due to the lift (figure 1.3 *c*). The experimental efficiency of a propeller of this type with highly loaded high aspect ratio blades is about 70% although frictional losses in the blade control mechanism are large and this effectively reduces the efficiency in practice (Bose and Lai 1989).

Oscillating foil propulsion, the objective of this research project, is used by most fast swimming marine animals and flying birds. Since a long time ago, scientists

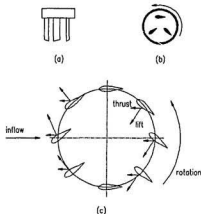


Figure 1.3: Schematic diagrams of a trochoidal propeller in operation. *a.* Side view; *b.* Section view; and *c.* Thrust creation.

have marvelled that with such a small area of tail compared with that of their bodies, marine swimmers (whales, dolphins, tuna etc.) move fast, and have remarkable manoeuvrability. On the body of a whale, the propulsor is mainly the flukes. These flukes have a hydrodynamic wing section with swept leading and trailing edges. Some wing sections and planforms of marine cetaceans are shown in figure 1.4; these have been taken from Bose et al. 1990. These planforms have different aspect ratios and different leading and trailing edge sweep angles. Predictions of propulsive performance of these planforms in an ideal fluid were made by Liu and Bose (1993) by using a linearized thin wing lifting surface theory with a rigid planform assumption. As the flukes are elastic, hydroelastic theory for an oscillating foil is expected to provide more accurate predictions; allowances for real viscous flow should also be made. Motion of the flukes is periodical in both pitch and heave. The traces of the foil in both heave and pitch, are shown in figure 1.5.

Propulsive performance is evaluated in terms of the efficiency and thrust coefficient. Generally, the highest efficiency is desired. However, for a given planform, the

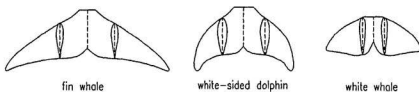


Figure 1.4: Some shapes of cetacean fluke planforms, after Bose et al., 1990.

higher the efficiency, the lower the thrust coefficient obtained. When the span of the foil is limited, the required thrust in some cases can be reached by increasing the area of the foil (by adding chord length) and by increasing the heave amplitude (see Chapter 6).

Compared with the screw propeller, the oscillating foil is lightly loaded, which is the main reason for its high hydrodynamical efficiency. A high aspect ratio, rigid oscillating foil in an ideal fluid, when the oscillating parameters are optimized, will give as high as 80% propulsive efficiency (Liu and Bose 1991). A 2-D flexible oscillating foil is expected to achieve a higher efficiency but with a decrease in the thrust coefficient (Wu 1971, Katz and Weihs 1989).

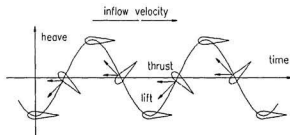


Figure 1.5: A trace of a sinusoidally oscillating foil.

## 1-C Objective of this research

The aim of this work was to evaluate the performance of flexible oscillating foils. The numerical model is based on boundary element theory with a time-domain approach. The method of formulation, special treatments, verifications and comparisons are as follows.

**2-D, steady, rigid foil:** The constant doublet velocity potential panel method was used to start the study, for an infinite span foil at constant angle of attack. The method and results were verified against Moran (1984). This 2-D steady method and its results were a starting point and they are not discussed.

**3-D, steady, rigid foil:** This is the extension of the 2-D steady rigid foil case. Results were checked against data from the literature. A number of numerical approaches were developed and combined into a new system of solution. These schemes include: applying the BiCGSTAB method to solve the system of linear equations with a consideration of both accuracy and computing speed on machines with or without sufficient dynamic random access memory; polyfitting the strength of the doublet to quadratic functions then differentiating them exactly in the calculation of the tangential velocities and applying a method that takes the jump of the trailing edge velocity potential into consideration in order to improve the results for a foil with a non-zero thickness trailing edge.

An extensive convergence study was performed with regard to the time step size, total number of time steps, number of chordwise and spanwise panels and their type of spacing arrangement, such as log, cosine and uniform grids.

**3-D, unsteady, rigid foil:** The 3-D steady case was further extended to the unsteady case. Verification was done corresponding to the previous results that were available. Mathematical formulation of thrust and efficiency and implementation of the computer program were also accomplished. The results were compared against those by Chopra and Kambe (1977) and Liu & Bose (1991).

Several numerical schemes were developed to improve the validity of the application of the steady Kutta condition, including the scheme of determination of the time step size, total number of time steps based on the newly defined total oscillating period and polyfit of the time variant doublet strength.

**Large amplitude consideration and analysis:** A practical large amplitude theory for oscillating foils was established. An analysis of large amplitude considerations was performed and it was used to explain the properties of the propulsive performance of an oscillating foil.

Being the first kind of such theoretical establishment, this analysis provided a powerful tool in the study of the nature of oscillating propulsion.

**3-D unsteady, flexible foil:** This is a modelling of an elastic foil with an arbitrary planform shape. The effect of both the chordwise and the spanwise flexibility and sweep angle on hydrodynamic characteristics were also considered.

A system combining both theoretical and numerical approaches was developed. A couple of phase angles of deflexion were defined to explore the possible motions of a flexible oscillating propulsor. A numerical method was also developed to calculate the angle of zero lift for both symmetric and asymmetric foil sections under chordwise deformation.

**Skin drag analysis:** Results predicted including effects of frictional shear stress were compared with those from the ideal flow model. An existing system of methods for a 2-D rigid foil for the calculation of skin friction coefficient and boundary layer growth was extended and applied to the 3-D flexible foils. The prediction of the boundary layer growth provided the qualitative evaluation and the comparison of the flow around a rigid and a flexible foil.

**Parametric investigation of performance:** Based on the large amplitude theory, a series of parametric studies of propulsive performance were done. Parameters included the variation of efficiency and thrust with changes in flexibility of the foil, the heave and pitch amplitudes, phase between the pitch and heave, etc.

## 1-D Perspective of this research program

Though many methods are available to solve the unsteady lifting problem, probably none of them are able to solve for a flexible, arbitrary planform exactly. Therefore, to predict the hydrodynamic characteristics of an oscillating flexible foil propeller with different planform configurations, numerical methods need to be applied. This increases the versatility of the computation and hence saves cumbersome mathematical formulation. Predictions of the propulsive performance of an oscillating foil can be done by a number of numerical methods. These methods divide themselves into four families: numerical methods based on boundary element theory (panel methods); those based on unsteady thin wing theory; those based on momentum theory (Glauret 1926, Moran 1984); and many applications in Navier-Stokes solvers. Unsteady thin wing theory has been used extensively in the aerodynamic community for more than half a century. Examples of these methods include lifting-line theory and lifting-surface theory. Both of them study the vortices in the flow that represent the foil. Lifting-line theory is appropriate only for foils with large aspect ratio planforms, because this theory was established by assuming the chord of the foil to be negligibly small. The accuracy of the predictions from lifting-line theory for low aspect ratio foils is questionable. As in most cases, especially in oscillating foil propulsion, the wings to be used are not of very large aspect ratio, the lifting-surface method such as the unsteady QVLM (Quasi-Vortex-Lattice-Method, Lan 1979) is a good choice. However, as for any numerical method, the unsteady QVLM has its own disadvantages. These shortcomings are as follows (Liu 1991).

- The unsteady QVLM is mainly an analytical solution. The spanwise integration for the downwash over each element is conducted analytically. An analytical formulation was primarily used, but a number of non-integrable integrands were replaced by quadratic functions in the last step of the solution. This adds difficulties in computer programming and mathematical formulation but gains a slight improvement in accuracy compared with the VLM method. This improvement cannot be made when a foil is in large amplitude motion.

- It was assumed that the trailing vortices extend from the trailing edge of the foil to infinity on the undisturbed  $x$ -plane (i.e., there is no oscillating wake). This assumption is basically a small amplitude theory, so that it is not realistic if this method is applied to large amplitude motion of an oscillating foil.
- When a wing having a large swept leading edge is under consideration, the ratio of the number of chordwise lattices to the number of spanwise lattices needs to be adjusted to maintain accuracy; this is similar to the problem identified by Albano and Rodden (1969). This reduces the reliability of the results, because the ratio is determined by a rough estimation.
- The QVLM is good for rigid, planar planforms. However, when a flexible wing is considered, further work on the formulation is needed, because Lan (1979) did not solve propulsion problems for a three dimensional unsteady elastic lifting surface.

The methods derived from unsteady lifting surface theory mentioned above are solutions in the frequency domain (time,  $t$ , is eliminated by using a harmonic complex variable). Frequency domain solutions are able to deal with wings in harmonic motions, but are limited to only certain types of motions, such as sinusoidal oscillations. It is difficult for these frequency domain solutions to deal with arbitrary motions, because the frequency is not obtainable from irregular motions and hence the irregular motion cannot be expressed as functions of the complex exponent, i.e., the harmonic function, and hence the kernel function. Some lifting surface methods have been designed to solve for the lift from a wing in the time domain. These kinds of methods reduce the complexity of the formulation of the method, by adding many steps to the calculation as it is repeated at each time step. Examples of these are described by Frydenlund and Kerwin (1977) and Katz and Plotkin (1991). Though the thickness problem in lifting surface theory can also be solved by placing sources along the element (Kinnas 1992), lifting-surface theory is not able to deal with wing-body combination problems, which are important for the overall evaluation of the hydrodynamic characteristics of a body in a fluid.

Moreover, the leading edge suction problem that occurs in lifting-surface theory, being an important problem in oscillating foil propulsion, is largely unresolved in time domain lifting surface theory. Although the time domain lifting surface approach has been applied in screw propeller design, the accuracy of blade loading predictions without an accurate calculation of the leading edge suction, especially in unsteady cases, is questionable, though the efficiency and the torque of the propeller were close to experimental data, for instance, in Kerwin and Lee (1978). This can be reasoned as: even without the contribution of the leading edge suction, the lift is probably not changed much and this will not greatly affect the thrust; the drag (torque) can be adjusted largely by changing the drag coefficient to cancel a contribution to the thrust by the leading edge suction which exists in practice. When the leading edge panel discretization is carefully arranged, a time-domain panel method is able to take both thickness and wing-body combinations into account, as well as the leading edge suction. The leading edge suction is included inherently in a panel method, though some say the velocities, and hence the suction, are over-predicted at the leading edge.

In this research work, a time domain panel method was applied and it was extended to cover a 3-D flexible oscillating propeller. Establishment of this unsteady 3-D flexible panel method enables us not only to evaluate the performance of oscillating foil propulsion, but also to use this to simulate the flying and swimming of animals in bio-mechanical research and to calculate other unsteady moving bodies in large amplitude motion in engineering applications.

## Chapter 2

# Review of Literature

### 2-A Historical Review

Theoretical studies in unsteady aerodynamics have been conducted since the late 1920s. The initiation of this subject was to predict the lift variation on wing surfaces subjected to flutter and gusts. In these unsteady flows, the circulation and aerodynamic characteristics of a moving foil change from instant to instant; these changes in lift, moment, and drag have an impact on the structural dynamic design of a wing and fuselage. Before the widespread use of powerful computers, analytical study of the aerodynamic characteristics of oscillating wings was well developed. Pioneer works presented in the 1930s include those by von Kármán and Burgers (1935), Theodorsen (1935), and von Kármán and Sears (1938). With the development of digital computer technology and techniques of computational fluid dynamics (CFD), numerical methods to treat complex wing configurations and unsteady flows became popular. These methods mainly fall into three categories: lifting-surface methods, panel methods, plus the recent study of Navier-Stokes solvers. As lifting surface theory for both steady and unsteady flows was reviewed and investigated previously (Liu 1991), the major part of this discussion will be devoted to panel methods.

### 2-A-1 Lifting surface theory

Some of the earliest studies in three dimensional lifting surface theory are credited to Falkner (1943) and Multhopp (1950). Falkner's (1943) presentation was the prototype of the vortex-lattice-method. The "quarter-chord and three-quarter-chord rule" (loading location and downwash location respectively) of subsonic lifting surface theory was initiated in his study. Following Multhopp (1950), many works in unsteady lifting surface theory were done based on the kernel function theory. Kernel functions are the expressions of linearized boundary value problems derived from the theoretical aerodynamics of lifting surface theory in a potential flow field. The singularities of the kernel function as an integrand make it difficult to obtain exact solutions (Watkins et al. 1955).

Richardson (1955) extended the subsonic kernel function to the sonic and supersonic ranges for the unsteady case. Before 1960, predictions of unsteady wing properties by using the unsteady kernel function method were not popular because of the primitive state of development of computing technology.

Since the early 1960s, a variety of numerical methods, mainly the lifting-surface method, have been presented to solve unsteady aerodynamical problems. These computer-implemented works based on lifting surface theory include those by Davies (1965), Albano and Rodden (1969), Lan (1979) and Frydenlund and Kerwin (1977). In most of these works the classical numerical procedure was used: that is, the unsteady kernel function was solved in the frequency domain. Frydenlund and Kerwin (1977), however, used a time domain scheme to predict propeller performance; so did Kerwin and Lee (1978). As the time interval was discretized in the computation, the formulation of the method was much more simple than that of the classical approach to the unsteady problem.

As lifting surface theory is based on a wing of zero thickness, predictions of aerodynamic characteristics of thick wings are inevitably inaccurate, especially when the thickness ratio (a ratio of the maximum thickness to the chord length of a foil)  $t/c$  is greater than 6%. In this case modification is usually required. This modification is often necessary because the thickness ratios of most wing structures in engineering

applications are greater than 6%. Meanwhile, according to classical lifting surface theory, modification of thickness is effective only for asymmetric wings. In other words, the lift predicted by classical lifting surface theory has the same value at different thicknesses if a wing section is symmetric (Bisplinghoff et al. 1955). This means that the difference in pressure distribution between symmetric thin and thick wings is neglected. For asymmetric wings, such as some propeller blades, modification of lift or loading can be done by superposition of source singularities and vortices to improve accuracy (Thwaites 1960, p. 366). However, calculation of leading edge suction remains a difficult problem, which is important in oscillating foil propulsion. When the normal inflow velocity is modified by adding the induced velocities due to camber and thickness, lifting surface theory obtains a realistic normal inflow velocity and loading distribution (Hsin et al. 1991). Nevertheless, accurate inflow normal velocity does not guarantee a realistic surface velocity distribution, which is the resultant of normal, tangential and transverse (spanwise) components. Accurate prediction of the velocity distribution, and hence pressure distribution, is not only essential to obtain the loading of a wing, especially oscillating foil thrust, but it is also useful to estimate boundary layer separation and transition from laminar flow to turbulent flow.

## 2-A-2 Panel methods

The panel method, also referred to as the boundary integral method or boundary element method, solving potential flow problems was initiated in 1962 after a pioneer work, known as the Douglas Neumann program, by Hess and Smith (Hess and Smith 1962). Their constant-strength source panel method can solve only nonlifting problems, though the versatility includes three-dimensional arbitrary body configurations. In 1967, Hess and Smith (1967) presented their continuing study covering both two- and three-dimensional bodies and lifting problems. The computation of forces on lifting bodies by using panel methods became possible. However, the analysis of the flow about arbitrary 3-D shapes, including lift and effects of thickness, in terms of source panel and vortex lattice presented by Rubbert and Saaris (1967) is probably the first use of a panel method for lifting problems. Their solutions to potential flow

problems include velocities and pressures at all collocation points; three-component forces and moments on each panel surface; velocity and pressure distribution in the flow field; and streamlines on the panel and in the field (Rubbert and Saaris 1972).

Before their engineering applications became widespread in the early 1980s, panel methods used to solve for aerodynamic characteristics mainly concentrated on distribution of sources and vortices (Hess 1975). Panel methods were often proposed to substitute for finite element and finite difference methods in calculations involving complicated geometric configurations, especially for external flows, in which case the grid generation to fit a 3-D shape was often difficult. The fundamental study of these methods in a mathematical sense and numerical principles remained mainly the concern of mathematicians and physicists (Brebbia and Dominguez 1989). After Ilunt (1980) and Banerjee and Butterfield (1981), systematic analysis of the mathematical formulation of boundary integral methods in both solid and fluid mechanics became familiar to engineers. Ilunt explained the physical problem using mathematical expressions; discussed the boundary conditions and also the uniqueness and existence of the solution to the Laplace equation, though without presenting strict mathematical evidence; and applied Green's theorems to solve Laplace's equation in single, multiple domains, thin surfaces and open surfaces. In Ilunt's study, surface singularities such as surface sources, surface doublets, surface vorticity and their combinations to solve potential flow problems, including the uniqueness of solutions under different singularity combinations and Neumann and Dirichlet boundary conditions in the steady flow case, were discussed.

In the early 1980s, there existed a variety of similar panel methods for the steady flow case, with differences in the order of panel strength distribution, singularity combinations, grid shapes and schemes for matrix iteration and inversion. Though not an exclusive list, these previous works include work by Johnson et al. (1982), Yen et al. (1981), Maskew (1982), Johnston et al. (1985), and Clark (1985).

After the middle 1980s, steady surface panel methods were also extensively applied to the calculation of wake simulations (Mracek and Mook 1988). The boundary integral method was first applied to marine propeller design in 1985 by Hess and Valarezo

(1985). In their study, the helical wake, the far wake behind a screw propeller, and the pressure distribution along the leading edge of the blades were predicted. Following Hess and Valarezo (1985), Kerwin et al. (1987), Koyama et al. (1986), Hoshino (1989), Valarezo and Liebeck (1988) and Hsin et al. (1991) used similar panel methods in marine propeller calculations.

Extensive applications of unsteady 3-D panel methods to aerodynamic problems started in the late 1980s. Solutions include both time domain and frequency domain methods. In the frequency domain, examples are work by Ruiz-Calavera and Geissler (1988), Rokhsaz et al. (1989) and Appa and Smith (1989). The use of 3-D time-domain panel methods became popular later. The studies by Blair and Williams (1989), Katz and Plotkin (1991), Kinnas and Hsin (1992) are examples. Three-dimensional time domain panel methods were extended to the calculation of multiple bodies and various paths only recently in a paper by Richson and Katz (1993).

Two dimensional unsteady panel methods have been in use for a long time e.g., Giesing (1968) and Basu and Hancock (1978). A time domain 2-D panel method to solve flexible wing propulsion problems was developed relatively recently by Bose (1992, 1993). In Bose's studies, the chordwise flexibility of foils was governed by a cubic function along the chord, and the tangential velocity at the elements on the wing surface was corrected in terms of deflection displacement of the element and the value at the foil surface between time intervals.

## 2-B Technical Review

As it can be seen in many mathematical physics texts, the boundary integral method is so called because it was used originally to solve linear partial differential equations (L.P.D.E.s) by integrating these equations within the domain of interest. The resultant integral is then solved by imposing sufficient boundary conditions. In fact, these L.P.D.E.s usually have no physical meaning unless variables in the L.P.D.E.s are assigned as certain physical properties for a particular physical problem. For example, for a L.P.D.E. in a form of Laplace's equation,

$$\frac{\partial^2 \phi}{\partial x_1^2} + \frac{\partial^2 \phi}{\partial x_2^2} + \frac{\partial^2 \phi}{\partial x_3^2} = 0, \quad (2.1)$$

if the potential  $\phi$  denotes heat, current or velocity potential, the flux

$$V_i = -k_{i,j} \frac{\partial \phi}{\partial x_j}, \quad (2.2)$$

where  $k_{i,j}$ , the second-rank tensor, denotes permeability in a homogenous region,  $V_i$  is then heat flux, current density, and fluid velocity in the directions of  $i = 1, 2, 3$ , respectively (Banerjee and Butterfield 1981).

Unlike finite element or finite difference methods that solve the governing equations (usually L.P.D.E.s) approximately by discretizing these L.P.D.E.s or by using the variational principle (Shaw 1978), boundary element methods solve the governing equations by direct integration and then solve the integro-differential equation either analytically or numerically. In boundary element methods, the formulation of the integro-differential equation can be done in different ways, depending on how the integro-differential equation is formulated. On the other hand, in formulating any boundary integral method, there should be the existence and uniqueness of the solution so that this formulation can be useful. Moreover, different formulations or schemes need to be employed to solve particular engineering problems. For example, for lifting problems, the Kutta condition needs to be used in the numerical process to obtain a unique solution; for unsteady lifting flows, both the Kutta condition and a proper vortex approach such as discretization and history of the wake need to be

taken into account to predict the flow on both surfaces of the wing and in the wake; for viscous and separated flows, formulation of the BEM has to be revised or the BEM has to be coupled with other method(s) such as finite element or finite difference methods. For shear flow and flow with separation, the BEM based on Navier-Stokes equations is also frequently used (see Shaw 1978, Morino 1989, Wu 1989, Hsiao and Porter 1989, Watts and Juang 1989, and Patterson et al. 1989). The above points were investigated and are briefly discussed below.

### 2-B-1 Three basic formulations

According to Banerjee and Butterfield (1981), to solve different engineering problems, there are basically three kinds of formulations in boundary element methods. They are the direct, semi-direct and indirect formulations.

#### The direct formulation

Application of this formulation is often found in solid mechanics problems, such as elasticity and elastoplasticity. The essence of this formulation is to integrate the governing equation directly. Banerjee and Butterfield (1981) indicated that in the process of integration, the flux (or velocity) or potential (or force in solid mechanics) in the field are found in the resultant integral in terms of all boundary values (see Banerjee and Butterfield, 1981, p. 26-30). This integration process will finally yield unknown boundary values with some other known boundary values. The velocities and potentials in the field can be determined by substituting all known boundary values into the velocity and potential integrals. A disadvantage of the direct formulation is that although the flux and potential are determined directly at boundaries, the values of variables at interior points are more difficult to find (Banerjee and Butterfield 1981). Another disadvantage is that this formulation is less accurate, for which the reasons are unknown (O'Brien and Geers 1989).

### **The semi-direct formulation**

In this kind of formulation, the integrand in the integral equation consists of an unknown function analogous to stress functions or stream functions (Banerjee and Butterfield 1981). Stress distribution or streamlines will be obtained by differentiating the solution of the boundary integral equation. There are not many applications of this approach.

### **Indirect formulation**

This formulation is also called the Green's function method, which is widely used in computational fluid dynamics. In this formulation, the governing equation, for instance, Laplace's equation for potential flow, is not directly integrated to form an integro-differential equation. Instead, a unit singular or a combination of several unit singular density function(s), which are fictitious with unknown density (Brebbia and Walker 1978), are placed on the boundaries of the domain as unknowns in the integrand of the integro-differential equation. This equation is then formed by using Green's Identity. Boundary values are determined by substituting given boundary conditions. As this formulation is important to this work, it will be discussed in detail in Chapter III.

### **2-B-2 The Kutta condition**

The steady Kutta condition assumes that, for a foil section in a steady, inviscid fluid flow, the stream leaves the sharp trailing edge of the foil smoothly and the velocity there is finite. This condition is also called the Joukowski's hypothesis from von Mises (1945). This hypothesis states that, the circulation of a foil with a sharp trailing edge, in its working range of incidence (attached flow), always adjusts itself so that the fluid speed at the trailing edge is finite. In Joukowski's conformal mapping of a circle onto a foil, a unique value of circulation must be chosen to obtain a stagnation point on the circle corresponding to the sharp trailing edge of the Joukowski profile (Milne-Thomson 1958, p.114-115). The Kutta conditions make the solution

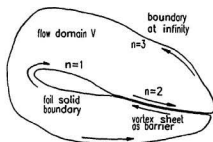


Figure 2.1: A foil with a wake vortex sheet in a lifting flow. Arrows stand for the path of the integration.  $\vec{n} = 1$ ,  $\vec{n} = 2$ , and  $\vec{n} = 3$  denote the boundaries—the foil surface, the surface of wake vortex sheet and the flow domain extending to infinity.

to lifting potential flow possible. The significance of the Kutta condition is illustrated as follows.

### The usefulness of the Kutta Condition

For a lifting foil whose circulation is not zero, the velocity potential has multiple values, in which case, the Kutta condition must be accomplished to obtain a unique solution. Due to viscous effects, there is a shear layer behind the trailing edge which extends to infinity (see figure 2.1). If the BEM method is based on potential flow, the flow domain must exclude the shear layer to satisfy the potential assumption. Meanwhile, if this layer is treated as a barrier, a doubly connected region of a 2-D flow domain can be changed into a simply connected region. However, because of the existence of this barrier, the velocity potential, as the solution of Laplace's equation, has no single value, i.e., the solution is not unique (Katz and Plotkin 1991, p. 35). The amount of circulation then cannot be determined without using the Kutta condition. In a different procedure, Moran (1984) showed that by specifying the circulation around a curve  $c$ , around the 2-D foil

$$\Gamma = - \oint_c \vec{\nabla} \phi \cdot d\vec{l}, \quad (2.3)$$

the solution of Laplace's equation, with the boundary condition of  $\nabla\phi \rightarrow V_\infty$  far from the foil (this foil is fixed at a point in a moving fluid at a speed of  $V_\infty$ ) and  $\vec{\nabla} \cdot \vec{n} = 0$  on the foil surface (normal velocity on the boundary is zero), is unique.

### The validity of the unsteady Kutta condition

The steady Kutta condition can also be applied in unsteady flow, but care must be taken. For instance, an unsteady foil moving at either high reduced frequency ( $k = \frac{\omega c}{2U}$ , where  $\omega$ ,  $c$  and  $U$  are oscillating frequency, chord length and forward velocity of the wing respectively), or large pitch or heave amplitude, will cause separation at the trailing edge. This means that the local flow passing the trailing edge is not smooth (streamlines are not departing parallel to the trailing edge) and hence this flow may violate the Kutta condition. Experiments (Katz and Plotkin 1991) indicated that slight trailing edge separation (when  $\frac{\omega c}{2U}$  is just greater than 0.6) does not have a noticeable effect on lift and in this case, the unsteady Kutta condition is still valid. Katz and Plotkin (1991) analyzed the validity of the Kutta condition and gave some boundaries for the validity of an unsteady Kutta condition, under the assumption of small-amplitude oscillation, as follows.

- For the steady flow case, large angles of attack should be carefully controlled to avoid a serious separation at the trailing edge or even at the leading edge (another problem: stall). In unsteady flow, the pitch amplitude should be carefully controlled.
- Again, to avoid large scale separation, the heave amplitude should be reduced when the reduced frequency increases. For example, to have a reasonable thrust level (the reduced frequency at its practical range from 0.5 to 1.0), when the reduced frequency reaches its upper practical limit  $k = \frac{\omega c}{2U} = 1$ , it allows the maximum amplitude up to  $h_o = 0.1 c$ , where  $h_o$  is heave amplitude in the heave motion equation, for example,  $h = h_o \cos(\omega t)$ . The feathering parameter (see Nomenclature), either the one under the small amplitude assumption or the one based on the larger amplitude assumption, cannot be used in this kind of

analysis, because the same value of this parameter has an infinite number of combinations of the instantaneous angle of attack (by adjusting the product of pitch amplitude and the forward flight speed).

- The non-dimensional vertical velocity should be  $V_k = \frac{\dot{h}}{V} \ll 1$ . This limits the vertical displacement of the trailing edge. This may become a problem when the foil is used as an oscillating propulsor.
- Separation at the trailing edge due to viscous effects will cause lag in the aerodynamic loads (see Katz and Plotkin 1992).

In addition, the pitching axis position may affect the degree of the validity. A pitch axis at the trailing edge will be better than one far ahead of the trailing edge, as trailing edge separation is more likely to be avoided. However, this may create early separation at the leading edge, which violates the attached flow assumption. In three-dimensional, large amplitude motion, the shape of the planform, the pitching axis position,  $P$ , the oscillating frequency,  $\omega$ , the advance speed,  $V_\infty$ , the heave amplitude,  $h_0$ , and the pitch amplitude,  $\alpha_0$ , do jointly influence the flow at the trailing edge and elsewhere. Analysis of the validity of the Kutta condition becomes more complicated.

The Kutta condition should be applied carefully to avoid errors in prediction of the loads on an oscillating foil. Without careful consideration, the predicted loads could lose their accuracy and reliability.

Different assumptions made by previous studies, however, also exist. In the Triantafyllou brothers' experimental studies at MIT (Triantafyllou and Triantafyllou 1995), they argued that the hydrodynamic loads, especially the thrust of a fish tail or an oscillating foil were mainly due to the vortex "jets" behind the propulsor created by its oscillating motion. Their assumption has not been yet implemented into any type of theoretical or numerical model.

### 2-B-3 The uniqueness of the solution

For a high Reynolds number (greater than  $10^6$ ), the boundary layer is thin so that the flow outside of the boundary layer can be treated as potential flow. For such a

potential flow, reasons supporting the validity of the approach are as follows.

- *Uniqueness of irrotational flow in a singly-connected region.* For an irrotational, single-connected region, a velocity potential  $\phi$  must exist. An irrotational, incompressible flow in a singly-connected region is unique (Lighthill 1986, p. 85).
- *Supplementary conditions for a doubly-connected region.* A doubly-connected region in a lifting flow domain, for example, a 2-D foil with its wake, can be transferred to a singly-connected region if the wake is to be treated as a barrier (see figure 2.1). However, in the singly-connected region, the circulation by a potential solution, is  $k\Gamma$  ( $k$  is an arbitrary constant), which has multiple values (see p. 93-94, Moran 1984). A supplementary condition is needed to provide the uniqueness of the solution to the velocity field for this singly-connected region that is transformed from the doubly-connected region (Lighthill 1986, p. 95-96). This supplementary condition, for an airfoil section with its wake, is the Kutta condition. When the Kutta condition is imposed in the solution, this modified doubly-connected region of a flow around a foil has a unique velocity distribution.
- *Uniqueness of the solution to an unsteady flow in a singly-connected region.* When a solid body is moving in an irrotational flow (in a singly-connected region), or this body is stationary in a moving fluid, the flow field can be determined uniquely by using the instantaneous velocity normal to the surface of the body (Batchelor 1967, p. 104). This indicates that the velocity profile of the flow field can be predicted uniquely and this prediction is dependent upon the instantaneous boundary condition only; the acceleration of the body and the motion history of the body have no effect on the prediction of velocity potential. However, the history of wake vortices cannot be neglected. In other words, a steady flow problem in a singly-connected region can be extended to an unsteady case as long as the instantaneous boundary condition is used. Therefore, a time-domain scheme can be employed in the unsteady singly-connected region. For example, at each time step in a numerical process, for a given boundary

condition (velocity normal to the surface of the wing), the flow field can be solved uniquely.

- *Uniqueness of the solution to a doubly-connected region in the unsteady case.* Bachelor (1967, p. 112) pointed out that an irrotational, unsteady, solenoidal flow in a doubly-connected region can be determined uniquely when the required boundary conditions for uniqueness of flow in a singly-connected region are imposed (wake as a barrier) and the cyclic constant is specified (by imposing the Kutta condition). This indicates that for an unsteady flow around an airfoil (doubly-connected region) when the unsteady Kutta condition is imposed, the unsteady potential flow of an airfoil can be solved by a time-domain scheme. Again, for the lifting problem, the induced velocity on the foil from wake vortices and their historic changes should be taken into account.
- *Force calculation from an unsteady potential flow solution.* As unsteady potential flow can be solved in the time domain, the obtained velocity potential and local velocity along the surface of the airfoil can be used to calculate aerodynamic forces. At each time step, the velocity potential  $\phi$  is unique; therefore, its derivatives  $\frac{\partial \phi}{\partial x_j}$  are unique. The velocity potential changes with time steps, hence  $\frac{\partial \phi}{\partial t}$  can be obtained. Therefore, the instantaneous local pressure can be determined from the unsteady Bernoulli equation.

## 2-B-4 Wake considerations

As the local velocity around a 2-D foil, which is moving in a static, incompressible fluid, varies with changes in pitch (instantaneous angular velocity of the foil, hence the angle of attack), heave (instantaneous vertical velocity and also the instantaneous angle of attack), forward flight speed, and/or part or all of these changes, the total circulation  $\Gamma$  of this section is changing. This circulation  $\Gamma$ , which is proportional to the lift ( $L = \rho U \Gamma$ ), is then a function of time  $t$ .

### Form of the wake behind a 2-D foil in unsteady flight

According to Kelvin's theorem

$$\frac{D\Gamma}{Dt} = 0 \quad (2.4)$$

in a flow domain. The development of a wake behind a wing section is simply described as follows.

- At time  $t = 0^+$ , for a wing section starting from rest with a moderate angle of attack, a starting vortex  $\Gamma_{start}$  at the trailing edge and a vortex  $\Gamma$  of total circulation of the section are created at the same time. Generation of this starting vortex is due to viscous effects at the trailing edge. The strengths of these two vortices are the same but opposite in direction to give

$$\frac{D\Gamma}{Dt} = \frac{D[\Gamma + \Gamma_{start}]}{Dt} = 0$$

(Batchelor 1967, p.440).

- If the wing section moves at a constant forward velocity, the total circulation  $\Gamma$  is constant and the starting vortex  $\Gamma_{start}$  once shed, is constant (Helmholtz theorem). In this case, there is no trailing vortex shed by the foil at the trailing edge because the span is infinite and then the change in spanwise circulation is zero (this will be discussed later in detail in the case of steady 3-D flow).
- When there is an increase in circulation around the foil section, from  $\Gamma$  to  $\Gamma + \Delta\Gamma$  due to an unsteady effect, to keep  $\frac{D\Gamma}{Dt} = 0$  in the entire flow domain ( $-\infty < x < +\infty$ ,  $-\infty < y < +\infty$ ), there must be a decrease of the strength of the vortices in the wake  $\Gamma_{start} - \Delta\Gamma$ , and this  $-\Delta\Gamma$  is the strength of a newly shed vortex. Similarly, decrease in circulation will produce a shedding vortex with an equivalent intensity but a counter circulation by the wing.

Figure 2.2 shows the variation of wake vortices shed at the trailing edge with changes in circulation of an oscillating foil. When the time is  $t = 0^+$ , those two vortices  $\Gamma_{t=0}$  and  $\Gamma_{start}$  are shed. From Kelvin's theorem,  $\Gamma_{t=0} + \Gamma_{start} = 0$ . If circulation of



and the strength of shed vortex at time  $t_i$  is then (Katz and Plotkin 1991, p.447)

$$\Gamma_{w,i} = -[\Gamma_i - \Gamma_{i-1}] = -\left\{ \Gamma_i + \sum_{k=1}^{i-1} \Gamma_{w,k} \right\}. \quad (2.6)$$

It is noted that from Helmholtz's theorems, in an ideal flow, where there is no diffusion, the strengths of shed vortices in the wake at any time, once shed, are constant. As a vortex wake is also force-free, this wake moves with the local velocity. The local velocity either on the wing surface or in the wake is the resultant velocity from which the velocity is induced by vortices on the wing surface and by all shed vortices in wake, i.e., all vortices in the flow domain.

### The influence of the wake on forces on a wing section

Forces on a 2-D foil include total lift<sup>1</sup> at an angle of attack<sup>2</sup>; moment about the leading edge; and thrust or drag along the direction of the mean motion of the wing. For a 2-D foil section in steady flow, there is no induced drag. Total drag consists of form drag and frictional drag.

von Kármán and Sears (1938) pointed out that lift and moment are the functions of the location and strength of wake vortices. They expressed the momentum on a foil section as the sum of momentums of vortex pairs (the product of the circulation and the distance between the individual vortices  $\Gamma_i(x_{i+1} - x_i)$ ). According to their work, vortices are laid both on the wing surface and are shed in the wake. Therefore, throughout the flow domain, the total momentum is  $\sum \Gamma_i x_i$ . As the wake vortices are continuously shed due to the change in strength of vortices on the wing (circulation), the total momentum  $\sum \Gamma_i x_i$  and the total moment of momentum  $\sum \Gamma_i x_i^2$  varies with that change. The lift and moment per unit area on the section were then expressed as the rate of the change in momentum and in moment of the momentum by

$$L = -\rho \frac{d}{dt} \sum \Gamma_i x_i, \quad (2.7)$$

<sup>1</sup>Total lift is the sum of all thrust components perpendicular to the velocity vector, acting on the wing (von Mises 1945).

<sup>2</sup>The angle of attack is the angle  $\alpha$  between the velocity  $V_\infty$  and an arbitrary chosen direction in the median plane of the foil; the angle of incidence is the angle of attack at zero lift direction (von Mises 1945).

and

$$M = -\rho \frac{d}{dt} \sum \Gamma_i x_i^2. \quad (2.8)$$

This indicates that the lift and moment are influenced by the wake vortices and this is one of several ways to obtain the lift and pitching moment.

In addition, there is no force acting on the surface of the wake. However, in the calculation of forces on the wing, the wake layer is moving with the local fluid, and the wake vortices are the history of the lift and moment changes on the wing. The effect of wake vortices on the instantaneous lift should be taken into account.

### Unsteady solenoidal flow around a finite aspect ratio foil

The spanwise lift distribution  $l_c(y)$  of a finite span foil can be represented in terms of the spanwise circulation distribution,  $l_c(y) = \rho U \Gamma(y)$ , where  $l_c(y)$  is sectional lift,  $\rho$  is density of fluid and  $\Gamma(y)$  is spanwise circulation distribution. For a rectangular lifting foil, the circulation  $\Gamma$  at the wing tips is zero, and gradually increases to its maximum value at the root chord section. The curvature of the circulation curve along the span is dependent upon the aspect ratio, the shape of the planform and the tip condition, etc. An elliptical planform moving at constant velocity in a static fluid with an elliptic spanwise circulation distribution is schematically shown in figure 2.3.

As circulation around adjacent sections varies, according to Kelvin's theorem, trailing vortices must be shed and these vortices move with the fluid; they cannot terminate (Lighthill, 1986). The strength per unit area of the trailing vortex filament should be equal to the rate of change in the spanwise circulation, i.e.,  $\gamma(y) = -\frac{d\Gamma(y)}{d|y|}$ , where the negative sign denotes that the strength of  $\Gamma(y)$  decreases when the value of  $|y|$  increases. This infinite number of vortex lines make a wake vortex sheet behind the foil (constructed by the broken lines in figure 2.3). According to Kelvin's theorem, these trailing vortices must go through the starting vortices so that each vortex filament has the form of a closed vortex ring starting from the bound vortices on the surface of the wing to the starting vortices via the trailing vortices in the

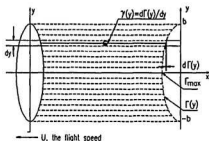


Figure 2.3: Generation of the trailing vortices due to variation of the spanwise circulation.

wake (figure 2.4). As these trailing vortices get longer with time, but their strength is constant, there is a drag, or induced drag, as associated with their formulation.

As the slope of the spanwise circulation curve at the tips for most wing planforms is steepest, the trailing vortex density  $\gamma(y)$  per unit length along the span reaches its maximum value at the tips. Near the root chord, the slope is gentle. For an infinite aspect ratio foil, this slope  $\frac{\Gamma(y)}{dy}$  is zero ( $\Gamma(y) = \text{constant}$  there). This is the reason why for a two dimensional foil in a steady flow, the trailing vortex strength is zero (the slope for an infinite span foil in the steady flow is zero, i.e., this trailing vortex strength,  $\frac{\Gamma(y)}{dy}$ ). For a qualitative analysis, the thickness of the vortex sheet is used to express the intensity of a local trailing vortex filament  $\gamma(y)$ , and the distribution of  $\gamma(y)$  for a foil in steady motion is shown in figure 2.4. The strength distribution of trailing vortices is also shown in figure 2.4 for different times in a short time of history before vortex sheet distortion occurs (for example, at  $t_1$  and  $t_2$ , these distributions are the same). Theoretically, in an inviscid fluid, though the vortex sheet distorts, the strength of each local vortex filament is constant. In certain cases, the vortex filaments join or form instabilities in the wake.

- *Unsteady spanwise lift distribution and form of the wake.* The spanwise circulation curve keeps changing due to the motion of the foil (yaw, roll, surge, pitch,

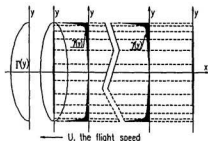


Figure 2.4: Formation of vortex rings by bound vortices, trailing vortices and starting vortices of a 3-D steady foil. Spanwise trailing vortex distribution is equated to the slope of the local circulation curve  $\Gamma(y)$  and this strength is expressed as the thickness of the vortex sheet.

leave and sway) at any instant. Changes in circulation from instant to instant, according to Kelvin's theorem, cause vortices to be shed from the trailing edge of the foil. A time dependent form of the wake is illustrated in figure 2.5. When the local sectional circulation  $\Gamma(y, t)$  increases at an amount from  $\Gamma(y, t_{i-1})$  to  $\Gamma(y, t_i)$  which is  $+\Delta\Gamma$ , there must be a shed vortex with its strength equalling  $+\Delta\Gamma$  being shed by the trailing edge of this section. Then the strength of the vortex currently shed is

$$\gamma(y, t) = \frac{\Gamma(y, t_i) - \Gamma(y, t_{i-1})}{t_i - t_{i-1}}. \quad (2.9)$$

In figure 2.5,  $\gamma_y(x, y)$ , or the strength of the shed vortex, has value equal to the negative slope of the spanwise circulation distribution  $\Gamma(y)$ , i.e.,  $-\frac{\partial\Gamma(y)}{\partial y}$  (by vortex continuity) and  $\gamma_x(x, y)$  has a value equal to the negative of the rate of change in the magnitude of  $\Gamma(y)$  with respect to travel distance ( $U \cdot t$ ), i.e.,  $-\frac{\partial\Gamma(y)}{\partial x}$ . These two vortex vectors are orthogonal to each other. The shed vortex  $\gamma_y(x, y)$  contributes to the roll-up of the vortex sheet at tip-to-tip as it is shown in figure 2.6; and the shed vortex  $\gamma_x(x, y)$  will affect the far wake roll-up starting at the starting vortex.

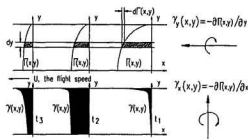


Figure 2.5: Shed vortices of a 3-D foil due to variation of the instant circulation. The local strength of circulation  $\gamma_y(x,y)$  is the rate of change of spanwise circulation with respect to the span location, and  $\gamma_x(x,y)$  in the wake is the rate of change of the sectional circulation with respect to the travel distance, or the time  $t$ .

In any numerical process, the slope of the circulation curve is discretized in steps to simulate the continuous vortices in the wake.

- *Roll-up of a vortex sheet behind a 3-D steady foil.* Roll-up of the vortex sheet in a wake can be described as follows.

As the wake vortex lines move with fluid (force free), and the local fluid velocity is induced by both bound vortices on the surface of the foil and by trailing vortices in the wake, the vortex sheet will be distorted with the motion of foil. In other words, the local velocity changes as the wing moves away and trailing vortices are continuously shed. The cross section of the vortex sheet ( $y - z$  plane) from the position close to the wing at  $x_1$  to a position far downstream at  $x_5$  in figure 2.6 shows the process of roll-up the vortex sheet, for a wing in steady motion (Lighthill 1986).

Induced by newly shed vortices and existing vortices on the planform and wake, the center part of the vortex sheet has a greater downwash as this downwash is contributed to by all vortices along the span with the same downward direction. Therefore, the center part of the vortex sheet moves downward due to the highly

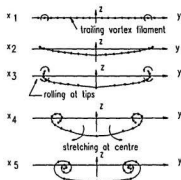


Figure 2.6: Schematic diagram of a vortex sheet roll-up process for a 3-D foil in a steady flow (Lighthill 1986). Induced by all vortices in the wake and on the wing, part of the vortex sheet in the wake close to the root chord goes downward; vortex filaments depart at the root chord towards the tips; and tip vortices are rolling up due to the induction of the inward vortices.

induced downwash. Meanwhile, affected by the downwash, vortex filaments close to and on the left and right-hand sides of the root chord will also go towards the left and right-hand tips respectively. With the continuing motion of the vortices, the local tip vortices are bent into two curled tubes. Within a limited distance from the foil, these tubes are cones. However, in the far wake, they will break due to instability and diffuse due to dissipation of viscous energy.

## Chapter 3

### Formulation of the method

This chapter presents the assumptions and a brief discussion of the formulation of the methods and solution procedures used in this research.

#### 3-A Physical aspects of the lifting flow domain

The flow around the foil was considered to be inviscid, incompressible and irrotational. The physical assumptions are as follows.

1. The Reynolds number  $Re$  is assumed to be high enough so that the boundary layer thickness is small. The attached boundary layers on the upper and lower surfaces of the foil meet at the trailing edge. The magnitudes of the vorticity shed by the upper and lower boundary layers are usually not equal to each other unless the foil is in steady motion; the sum of these two generated vortices equals the wake vorticity and this wake vorticity leaves the trailing edge of a moving foil. This wake vorticity assumed to be a sheet or thin layer; this sheet increases its size when the foil moves and it moves with the local fluid and rolls up. The difference in pressure across the sheet and normal velocity of the whole sheet are both equal to zero. Across this vortex sheet there is a discontinuity in the tangential velocity; hence the velocity potential across it is discontinuous.

2. As the flow is irrotational,

$$\vec{\nabla} \times \vec{V} = 0. \quad (3.1)$$

Therefore, there must be a flow potential to express the flow velocities,  $V_i = \frac{\partial \phi}{\partial x_i}$ , i.e.,  $\vec{V} = \vec{\nabla} \cdot \phi$ . On the other hand, the incompressibility of the fluid yields:

$$\text{div} \vec{V} = \vec{\nabla} \cdot \vec{V} = \frac{\partial V_1}{\partial x_1} + \frac{\partial V_2}{\partial x_2} + \frac{\partial V_3}{\partial x_3} = 0. \quad (3.2)$$

This guarantees the flow being potential, and if it exists, it must be

$$\frac{\partial^2 \phi}{\partial x_1^2} + \frac{\partial^2 \phi}{\partial x_2^2} + \frac{\partial^2 \phi}{\partial x_3^2} = \nabla^2 \phi = 0. \quad (3.3)$$

3. The boundary conditions for equation (3.3) are a) the velocity at infinity is zero, yielding  $\vec{V}_\infty = \vec{\nabla} \cdot \phi = 0$ , and b) the normal velocity passing through the boundary of the foil section is zero, i.e.,

$$V_n = \frac{\partial \phi}{\partial n} = \vec{n} \cdot \vec{V} = 0. \quad (3.4)$$

This is a “Neumann exterior” problem (Katz and Plotkin 1991) and the unique solution to equation (3.3) does not exist unless a physical boundary condition is imposed. This boundary condition, as discussed on page 26, is the Kutta condition. In most panel methods for solving lifting flow problems, the Neumann exterior problem is solved by using Green’s identity method and imposing the Kutta condition.

### 3-B Formulation of the potential based panel method

In classical mathematical physics, there exist several approaches to solving a L.P.D.E. They are typically the standing-wave scheme (separating variables and Fourier techniques); frequency spectrum approach (Fourier and Laplace transformations); progressive wave analysis (D'Alembert theorem) and the source-doublet method (Green's identity application). Procedures of the indirect formulation of the potential based method are discussed below.

The procedure and applications of Green's identities only are briefly discussed here. Considering a three-dimensional potential flow domain, if the velocity potential is  $\phi_1$  at one point and  $\phi_2$  at another, and these velocity potentials are harmonics, Green's first identity yields

$$\iiint_V \phi_1 \nabla^2 \phi_2 dV = \iint_S \phi_1 \frac{\partial \phi_2}{\partial n} dS - \iiint_V \nabla \phi_1 \cdot \nabla \phi_2 dV, \quad (3.5)$$

where  $S$  and  $V$  denote the domains of the integration.  $S$  is a closed surface enclosing the finite volume  $V$  of the flow domain and  $S$  must be an orientable surface.  $\phi_1$  and  $\phi_2$  are harmonics, eq. (3.5) can be interchangeably rewritten as

$$\iiint_V \phi_2 \nabla^2 \phi_1 dV = \iint_S \phi_2 \frac{\partial \phi_1}{\partial n} dS - \iiint_V \nabla \phi_2 \cdot \nabla \phi_1 dV. \quad (3.6)$$

Subtracting eq. (3.6) from eq. (3.5) yields

$$\iiint_V (\phi_1 \nabla^2 \phi_2 - \phi_2 \nabla^2 \phi_1) dV = \iint_S (\phi_1 \frac{\partial \phi_2}{\partial n} - \phi_2 \frac{\partial \phi_1}{\partial n}) dS. \quad (3.7)$$

eq. (3.7) is Green's second identity. It can be written alternatively via  $\frac{\partial}{\partial n} = \nabla \cdot \vec{n}$  as

$$\iiint_V (\phi_1 \nabla^2 \phi_2 - \phi_2 \nabla^2 \phi_1) dV = \iint_S (\phi_1 \nabla \phi_2 - \phi_2 \nabla \phi_1) \cdot \vec{n} dS, \quad (3.8)$$

which is eq. 3.4 in Katz and Plotkin (1991). Eq. (3.8) can also be obtained by defining a velocity vector

$$\vec{V} = (\phi_1 \nabla \phi_2 - \phi_2 \nabla \phi_1), \quad (3.9)$$

and applying the divergence theorem (Moran 1984)

$$\iiint_V \text{div} \vec{V} dV = \iint_S \vec{n} \cdot \vec{V} dS. \quad (3.10)$$

The significance of Green's second identity, is that the values of  $\phi_1$  and  $\phi_2$  at any position  $(x, y, z)$  within the flow domain can be expressed as a surface integral, and  $\phi_1$  and  $\phi_2$  in the surface integral are the values on the boundary(s) of the flow domain. In other words,  $\phi_1(x, y, z)$ ,  $\phi_2(x, y, z)$ ,  $\nabla^2\phi_1(x, y, z)$  and  $\nabla^2\phi_2(x, y, z)$  have certain relations governed by Green's second identity with the boundary values of  $\phi_1(a, b, c)$ ,  $\phi_2(a, b, c)$ ,  $\frac{\partial\phi_1(a, b, c)}{\partial n}$  and  $\frac{\partial\phi_2(a, b, c)}{\partial n}$ , where  $a$ ,  $b$ , and  $c$  are coordinates on the boundary. Though Green's second identity reveals those relations, it cannot be used directly to solve the boundary value problems.

Green's third identity in three dimensional cases states

$$\phi(p) = \frac{-1}{4\pi} \iint_S \left[ \frac{1}{r} \frac{\partial\phi_Q}{\partial n} - \phi_Q \frac{\partial}{\partial n} \left( \frac{1}{r} \right) \right] dS. \quad (3.11)$$

For multibody problems, as Laplace's equation is linear, a solution can be obtained by superposition. Therefore, eq. (3.11) can be applied generally as

$$\phi(P) = \frac{-1}{4\pi} \sum_{n=1}^N \iint_S \left[ \frac{1}{r} \frac{\partial\phi_Q}{\partial n} - \phi_Q \frac{\partial}{\partial n} \left( \frac{1}{r} \right) \right] dS. \quad (3.12)$$

In a lifting flow, where a foil has a wake extending downstream,  $N = 3$  is defined for the surface boundary of the foil surface, the wake vortex sheet surface and the infinity boundary surface (see figure 2.1).

Considering a solid foil boundary (figure 3.1), the differences in velocity potential and velocity between the inside and outside of the boundary at point  $Q$  are

$$\phi_Q = \phi_{in} - \phi_{out}, \quad (3.13)$$

and

$$\frac{\partial\phi_Q}{\partial n} = \frac{\partial\phi_{in} - \partial\phi_{out}}{\partial n} \quad (3.14)$$

respectively. As the velocity potential of a unit doublet  $\phi_{doublet}$  is equal to  $\frac{\partial\phi_{doublet}}{\partial n}$  (see Katz and Plotkin 1992),  $\phi_Q$  and  $\frac{\partial\phi_Q}{\partial n}$  can be equalized as

$$\phi_Q = \phi_{in} - \phi_{out} = \sigma \quad (3.15)$$

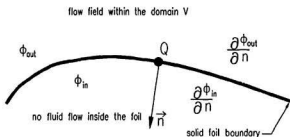


Figure 3.1: Boundary conditions of velocity potential and normal velocity. Velocity potential across the solid foil boundary has a jump, which is discontinuous, and normal velocity across the boundary is continuous, which is zero.

and

$$\frac{\partial \phi_Q}{\partial n} = \frac{\partial \phi_{in} - \partial \phi_{out}}{\partial n} = \mu, \quad (3.16)$$

where  $\sigma$  and  $\mu$  are the strength of the source and doublet respectively. With the unknown strengths of the source and doublet being placed in the integral of Green's third identity, the potential flow based boundary integral method finally follows

$$\phi(P) = \frac{-1}{4\pi} \sum_{n=1}^N \iint_S \left[ \sigma \frac{1}{r} - \mu \frac{\partial}{\partial n} \left( \frac{1}{r} \right) \right] dS. \quad (3.17)$$

According to the boundary conditions for the potential lifting flow assumed on page 37-38, both sources  $\sigma$  and doublets  $\mu$  are allowed to exist on the surface of the foil, though either one or both can be placed alternatively; on the wake vortex sheet, as normal velocity  $v_n = \frac{\partial \phi}{\partial n}$  is continuous and velocity potential has discontinuity (jump on the boundary), only doublets are allowed on the sheet surface; at infinity, as  $r \rightarrow \infty$ , both terms in the integral vanish, hence  $\phi(P)$  at  $n = 3$  (boundary is taken as infinity) is a constant, or  $\phi_\infty(P)$ . The known velocity potential  $\phi(P)$  of a unit source and/or doublet at point  $P$ , has an influence on the boundary. This influence can be determined in terms of the unknown strengths of these doublets and sources

being placed on the boundary and the distance,  $r$ , from point  $Q$  on the boundary to point  $P$  in the domain, with an unknown potential  $\phi(P)$ . However, if  $P$  is chosen inside the foil,  $\phi(P)$  is zero—this will significantly simplify the solution procedure (see Katz and Plotkin 1991). In three dimensional cases for the foil, wake and the flow boundary at infinity, the following relation exists

$$\phi(P) = \frac{-1}{4\pi} \iint_{\text{foil}} \left[ \sigma \frac{1}{r} - \mu \frac{\partial}{\partial n} \left( \frac{1}{r} \right) \right] dS + \frac{1}{4\pi} \iint_{\text{wake}} \mu \frac{\partial}{\partial n} \left( \frac{1}{r} \right) dS + \phi_{\infty}(P), \quad (3.18)$$

which is eq.3.13 in Katz and Plotkin (1991). Similarly, the boundary integral in the two dimensional case is then in the form of Katz and Plotkin (1991) as

$$\phi(P) = \frac{1}{2\pi} \oint_{\text{foil}} \left[ \sigma \ln r - \mu \frac{\partial}{\partial n} (\ln r) \right] dS - \frac{1}{2\pi} \oint_{\text{wake}} \mu \frac{\partial}{\partial n} (\ln r) dS + \phi_{\infty}(P). \quad (3.19)$$

A minus sign has been added to equation 3.19 due to a different assumption of the direction of the normal vector of the foil's surface.

Similarly, if a source and/or doublet is placed on the foil surface, the velocity potential and induced velocity at an arbitrary point  $P$  in the domain (point  $P$  can also be placed on the boundary) will also have the same relation as given in eq. (3.18) or eq. (3.19). This relation allows application of the boundary integrals above to solve practical problems. When eq. (3.18) or eq. (3.19) is to be solved numerically, a number of source and/or doublet elements are placed on the foil outer surface, a number of doublet elements<sup>1</sup> are placed on the inner surface of the barrier (wake vortex sheet). In addition, for a flow around a fixed foil,  $\phi_{\infty}(P) = U_{\infty}x + V_{\infty}y + W_{\infty}z$ , is not constant; for a foil moving in a static fluid, the velocity potential  $\phi_{\infty}(P)$  is constant and, as a reference point, this constant can be taken. However, the mean velocity of the foil implies that there are velocity components added to the moving body, i.e., an additional

$$\vec{V}_{a,d,t} = U_{\infty}\vec{i} + V_{\infty}\vec{j} + W_{\infty}\vec{k}. \quad (3.20)$$

Solution of eq. (3.18) and eq. (3.19) falls into three categories: Dirichlet problems ( $\phi$  is given at the boundary as a function), Neumann problems (the derivative of  $\phi$

<sup>1</sup>A doublet distribution has the same velocity potential as the vortex ring does, if they are placed properly. See Moran 1984.

with respect to the normal, or the normal velocity  $\frac{\partial \phi}{\partial n}$  is known at the boundary) and Robin problems (boundary values are given as mixed Dirichlet and Neumann conditions). Again, for lifting problems they cannot be solved uniquely unless a Kutta condition is imposed.

## 3-C Numerical implementation

### 3-C-1 The method of numerical solution

By applying the Dirichlet boundary condition, a combination of source and doublet distributions was used for the solution. By setting the inner velocity potential as constant, eq. (3.18), referring to the body frame, yields a zero value at each panel:

$$\frac{-1}{4\pi} \iint_{\text{foil}} \sigma \frac{1}{r} dS + \frac{-1}{4\pi} \iint_{\text{foil}} \mu \frac{\partial}{\partial n} \left( \frac{1}{r} \right) dS + \frac{-1}{4\pi} \iint_{\text{wake}} \mu \frac{\partial}{\partial n} \left( \frac{1}{r} \right) dS = 0. \quad (3.21)$$

For this to be valid, as was discussed in the previous section, the unit source strength has to be set as (p.241 Katz and Plotkin 1991):

$$\sigma = \vec{n} \cdot \vec{V}_\infty, \quad (3.22)$$

where  $\vec{n}$  is the normal vector of the foil's surface.

It is noted that  $\vec{V}_\infty$  is the total kinematic velocity due to the motion of the foil, not the forward swim speed  $V_{\text{flight}}$ , which was often expressed as  $V_\infty$  in the literature.

A number of surface panels were placed on the body of the foil and the shed wake. For each panel, three influence coefficients, corresponding to the three terms of eq. (3.21) were obtained. For the two doublet influence coefficients (wake and foil), the numerical solution was obtained through the following steps (Newman 1986):

1. The analytical result of the integration over a polygonal surface panel

$$\Phi_{\text{doublet}} = \frac{z\mu}{4\pi} \iint_S \left[ (x - \xi)^2 + (y - \eta)^2 + z^2 \right]^{-3/2} d\xi d\eta \quad (3.23)$$

is used. Here, the domain of integration  $S$  is divided by an infinite number of elements  $d\xi d\eta$ .

2. For each panel where the influence coefficients are to be sought, the coordinates<sup>2</sup>

<sup>2</sup>In this thesis,  $x$ ,  $y$  and  $z$  represent the values in body frame;  $X$ ,  $Y$ , and  $Z$  represent inertia frame and  $\xi$  and  $\eta$  are panel coordinates. Because the panel was assumed flat, the vertical ordinate of the panel is zero.

$X$ ,  $Y$ , and  $Z$  of the control point of each panel were transferred to a Cartesian coordinate system that is established on the local panel. In the process of evaluation of the influence coefficient, the local panel coordinate system is the reference frame and this panel is the one which makes the contribution to the influence.

3. The influence coefficient at a point (usually the control point of a quadrilateral panel) due to a unit doublet on another quadrilateral panel was obtained by integrating along the other panels's four sides. A numerical form of eq. (3.23) that was presented by Newman (1986) was then used:

$$\Phi_{doublet} = \frac{z\mu}{4\pi} \sum_{n=1}^4 \left[ \tan^{-1} \frac{\delta\eta_n[(x - \xi_n)^2 + z^2] - \delta\xi_n(x - \xi_n)(y - \eta_n)}{R_n z \delta\xi_n} - \tan^{-1} \frac{\delta\eta_n[(x - \xi_{n+1})^2 + z^2] - \delta\xi_n(x - \xi_{n+1})(y - \eta_{n+1})}{R_{n+1} z \delta\xi_n} \right], \quad (3.24)$$

where  $\delta\eta_n = \eta_{n+1} - \eta_n$ ,  $\delta\xi_n = \xi_{n+1} - \xi_n$  with cyclic convention;  $R_n$  was the distance from the  $n$ -th corner point to point  $P(X, Y, Z)$ , the control point, where the influence coefficient is found. A schematic diagram is presented in figure A.1 in Appendix A.

The source influence coefficients at each panel were calculated as follows:

1. The analytical solution to the first term of eq. (3.23) was presented by Newman (1986):

$$\Phi_{source} = - \int_z^{\infty} z d\Phi_{doublet} - z\Phi_{doublet}. \quad (3.25)$$

2. Newman (1986) obtained a numerical form of eq. (3.25) for sources on a quadrilateral panel as:

$$\Phi_{\text{source}} = -\frac{z\sigma}{4\pi} \sum_{n=1}^4 \{(x - \xi_n) \sin \theta_n - (y - \eta_n) \cos \theta_n\} \ln \frac{R_n + R_{n+1} + s_n}{R_n + R_{n+1} - s_n} - z\Phi_{\text{doublet}}, \quad (3.26)$$

where  $\sin \theta_n = \frac{y - \eta_n}{s_n}$  and  $\cos \theta_n = \frac{x - \xi_n}{s_n}$  and  $s_n$  is the length of the  $n$ -th side of the panel.

To numerically evaluate eq. (3.24), in the summation of the values of the inverse tangent functions, when the panel angle  $n$  is in the range of  $(-\pi, \pi)$ , has to be dealt with carefully. To do this, Newman (1986) combined the two terms of eq. (3.24) by

$$\begin{aligned} \tan^{-1}\left(\frac{s_1}{c_1}\right) - \tan^{-1}\left(\frac{s_2}{c_2}\right) &= \tan^{-1}\left(\frac{s_3}{c_3}\right); \\ s_3 &= s_1 c_2 - s_2 c_1; \\ c_3 &= c_1 c_2 - s_1 s_2. \end{aligned} \quad (3.27)$$

For a foil body having  $N$  panels, the influence coefficient matrices, due to the doublet and the source on the solid boundary, have an order of  $N$ . They were labelled as follows:

$$\begin{bmatrix} d_{1,1} & d_{1,2} & \cdots & \cdots & d_{1,N} \\ d_{2,1} & d_{2,2} & \cdots & \cdots & d_{2,N} \\ \vdots & \vdots & \vdots & \vdots & \vdots \\ \vdots & \vdots & \vdots & \vdots & \vdots \\ d_{N,1} & d_{N,2} & \cdots & \cdots & d_{N,N} \end{bmatrix} \begin{bmatrix} \mu_1 \\ \mu_2 \\ \vdots \\ \vdots \\ \mu_N \end{bmatrix} \quad (3.28)$$

and

$$\begin{bmatrix} O_{1,1} & O_{1,2} & \cdots & \cdots & O_{1,N} \\ O_{2,1} & O_{2,2} & \cdots & \cdots & O_{2,N} \\ \vdots & \vdots & \vdots & \vdots & \vdots \\ \vdots & \vdots & \vdots & \vdots & \vdots \\ O_{N,1} & O_{N,2} & \cdots & \cdots & O_{N,N} \end{bmatrix} \begin{bmatrix} \sigma_1 \\ \sigma_2 \\ \vdots \\ \vdots \\ \sigma_N \end{bmatrix} \quad (3.29)$$

With the marching of the time steps, the size of the shed wake doublet influence coefficient matrix grows and it has an order of  $N \times K$ , where  $K = M * L$  is the number of columns of the matrix,  $M$  is the number of wake strips across the span and  $L$  is the number of total time steps. This matrix at the last time step (which covers the history of all the shed vortices) looks like:

$$\begin{bmatrix} dw_{1,1,1} & \cdots & dw_{1,M,1} & \cdots & \cdots & dw_{1,1,L} & \cdots & dw_{1,M,L} \\ \vdots & \vdots \\ \vdots & \vdots \\ dw_{N,1,1} & \cdots & dw_{N,M,1} & \cdots & \cdots & dw_{N,1,L} & \cdots & dw_{N,M,L} \end{bmatrix} \begin{bmatrix} \mu w_1 \\ \vdots \\ \vdots \\ \mu w_K \end{bmatrix}. \quad (3.30)$$

A subroutine was carefully written as the engine of the OSFBEM to obtain the coefficient matrices, along with another subroutine to transfer the global coordinates to panel local coordinates. These subroutines and two sample matrices are included as Appendix A.

The  $\mu_i$  in eq. (3.28), in this doublet-source perturbation potential method<sup>3</sup>, is equivalent to  $\Phi_i$ , the distribution of velocity potential over the solid surface. Once the distribution of  $\mu_i$  was obtained, the tangential velocities were then obtained by differentiating the potential with respect to the tangential vectors of each panel. For rigid foils, as panel relative positions remained unchanged, these coefficient matrices were the same for each time step. For an elastic foil, they had to be obtained at each time step.

As can be seen, if  $\sigma_i$  and  $\mu_i$  are not given, there is no unique solution to the linear equation system:

$$eq. (3.28) - eq. (3.29) + eq. (3.30) = 0.$$

However, eq. (3.29) becomes a known one-column matrix by applying eq. (3.22). The total kinematic velocity due to the motion of the foil was obtained by:

$$\vec{V}_{\infty} = \vec{V}_{trans} + \vec{V}_{rot} + \vec{V}_{flex}. \quad (3.31)$$

<sup>3</sup>By assuming the inner velocity potential being constant, i.e., zero, the local doublet strength yields a value the same as that of the local velocity potential. See Katz and Plotkin 1991, p.240.

The velocity  $\vec{V}_{trans}$  due to translation was the velocity at the origin of the body frame coordinates. It consists of the x-component, foil forward swim speed  $V_{flight}$  and the vertical component, foil heaving velocity  $\dot{h}$ . The y-component for an oscillating foil is zero. It is in a form of

$$\vec{V}_{trans} = (V_{flight}, 0, \dot{h}). \quad (3.32)$$

The velocity due to rigid body revolution about three fixed axes,  $\vec{V}_{rot}$ , was:

$$\vec{V}_{rot} = \vec{\Omega} \times \vec{r}, \quad (3.33)$$

where  $\vec{r}(x, y, z)$  is referred to the body frame and  $\vec{\Omega}$ , for a foil with pitch only, is  $(0, \dot{\alpha}_{pitch}, 0)$ .

A large amplitude motion was assumed. Therefore, the velocity of heave and pitch were derived from:

$$h = h_o \sin(\omega t - \Phi_{phase}) \quad (3.34)$$

and

$$\alpha = \alpha_o \sin(\omega t). \quad (3.35)$$

For a flexible foil, the velocity at each panel, due to the relative motion of the panel within each time step was obtained by determining the time derivative of the deflexion equation  $f(x, y, z, t)$ . It was noted that this velocity was based on the body frame so that it had to be projected to the global frame in order to be summed in eq. (3.31).

When the total kinematic velocity  $\vec{V}_{\infty}$  was projected onto the panel surface, the values of  $\sigma$  were then the normal components of the projected velocity  $\vec{V}_{\infty}$ . With these known source strength values, eq. (3.29) was reduced to a one-column matrix and moved to the right-hand-side becoming  $RHS_1$ .

As mentioned in a previous section, eq. (3.18) does not have a unique solution if the Kutta condition is not imposed. Eq. (3.30) was also reduced to a known one-column

matrix. This was done in two steps:

1. *Finding the doublet strength at the immediately shed wake panel at the current time step.* Once these values are found, they remain constant. As the wake roll-up is not implemented in this method, the locations of the wake panel remain where they were shed. A steady Kutta condition (Morino 1974) was used to determine these values. This Morino Kutta condition,

$$\Phi_{wake} = \Phi_{upper} - \Phi_{lower}, \quad (3.36)$$

is then evaluated along each wake strip across the span at each time step. Eq. (3.36) indicates that a number ( $M$ ) of unknowns should be added to the system linear equations. The coefficient matrix of eq. (3.28) was then rewritten as

$$\begin{bmatrix} d_{1,1} & \dots & d_{1,J} & dw_{1,1w} & \dots & \dots & d_{1,J+(M-1)+1} & \dots & d_{1,M*N} & d_{1,Mw} \\ \vdots & \vdots \\ d_{M,1} & \dots & d_{M,J} & dw_{M,1w} & \dots & \dots & d_{M,J+(M-1)+1} & \dots & d_{M,M*N} & d_{M,Mw} \\ 1 & \dots & -1 & 1 & \dots & \dots & 1 & \dots & -1 & 1 \\ \vdots & \vdots \\ \vdots & \vdots \\ d_{M,J,1} & \dots & d_{M,J,J} & dw_{M,J,1w} & \dots & \dots & d_{M,J,J+(M-1)+1} & \dots & d_{M,J,M*N} & d_{M,J,Mw} \\ 1 & \dots & -1 & 1 & \dots & \dots & 1 & \dots & -1 & 1 \end{bmatrix}, \quad (3.37)$$

where  $J$  is the number of total chordwise panels including both the upper and lower surfaces and  $M$  is the number of total spanwise strips. The subscripts ( $k, m_w$ ) are the flags of the influence coefficient at  $k$  contributed by the  $i$ -th immediately shed wake panel;  $k$  ranges from 1 to  $M * J$  and  $m_w$  from 1 to  $M$ .

Eq. (3.37) was then reduced to a  $(N + M) \times (N + M)$  coefficient matrix by substituting

$$d_{1,1w}\mu_{1,1w} = d_{1,1w}\mu_{1,M} - d_{1,1w}\mu_{1,1} \quad (3.38)$$

into the  $(M + 1)$ -th row for the first wake panel of eq. (3.37) and so forth as:

$$\begin{bmatrix}
 (d_{1,1} - dw_{1,1w}) & \cdots & (d_{1,J} + dw_{1,1w}) & \cdots & \cdots & (d_{1,J+(M-1)+1} - d_{1,Mw}) & \cdots & (d_{1,M+N} + d_{1,Mw}) \\
 \vdots & \vdots \\
 (d_{2,1} - dw_{2,1w}) & \cdots & (d_{2,J} + dw_{2,1w}) & \cdots & \cdots & (d_{2,J+(M-1)+1} - d_{2,Mw}) & \cdots & (d_{2,M+N} + d_{2,Mw}) \\
 0 & \cdots & 0 & \cdots & \cdots & 0 & \cdots & 0 \\
 \vdots & \vdots \\
 \vdots & \vdots \\
 (d_{M,J,1} - dw_{M,J,1w}) & \cdots & (d_{M,J,J} + dw_{M,J,1w}) & \cdots & \cdots & (d_{M,J,J+(M-1)+1} - d_{M,J,Mw}) & \cdots & (d_{M,J,M+N} + d_{M,J,Mw}) \\
 0 & \cdots & 0 & \cdots & \cdots & 0 & \cdots & 0
 \end{bmatrix} \quad (3.39)$$

At each time step, the values of doublet strength on the newly shed wake panel were found by using eq. (3.36) for each wake strip (each section), after the linear equation system was solved.

2. *Using the values of the previous shed wake doublets to find the one-column matrix.* This is done as follows:

- At time  $t = t_0$ ,  $\mu_1 \cdots \mu_M$  were found by using the steady Kutta condition and the matrix solver. There was no wake matrix formed.
- At time  $t = t_1$ , the wake matrix then became

$$\begin{bmatrix}
 dw_{1,1,1} & dw_{1,2,1} & \cdots & dw_{1,M,1} \\
 dw_{2,1,1} & dw_{2,2,1} & \cdots & dw_{2,M,1} \\
 \vdots & \vdots & \vdots & \vdots \\
 \vdots & \vdots & \vdots & \vdots \\
 dw_{N,1,1} & dw_{N,2,1} & \cdots & dw_{N,M,1}
 \end{bmatrix} \begin{bmatrix}
 \mu w_1 \\
 \mu w_2 \\
 \vdots \\
 \vdots \\
 \mu w_M
 \end{bmatrix}, \quad (3.40)$$

where  $N$  is the total number of panels and  $M$  is the number of wake strips. The wake coefficient matrix had a size of  $(J \times M) \times M = J \times M^2$ , where  $J$  is the total number of panels at each section. At this time step, there were only  $M$  wake panels.

- At time  $t = t_L$ , the last time step, the wake matrix became eq. (3.30).

This one-column matrix which incorporated the wake effect moved to the right-hand-side as  $RHS_2$ .

To improve the accuracy of the prediction, Katz and Plotkin (1991) moved the control point of each immediately shed wake panel closer to the trailing edge of the foil. Instead of doing so, this method employed a number of different approaches to improve the accuracy of the results. Two of these approaches are explained below.

When the trailing edge of the foil had a non-zero thickness, a substantial error in prediction occurred. This is because the Kutta condition is invalid at the trailing edge. To avoid this, the difference in the velocity potential  $\Phi_\infty$  at the trailing edge on the lower surface panel and on the upper surface panel had to be taken into consideration. Youngren et. al. (1983) has proposed an adjustment on their low order panel method, QUADPAN. Maskew (1987) used a similar approach in his VSAERO. This was done according to the formula:

$$\mu_w = \mu_{upper} - \mu_{lower} + \Phi_{\infty,upper} - \Phi_{\infty,lower}. \quad (3.41)$$

These velocity potentials were evaluated in terms of the dot product of the global velocity and the global coordinates of the panel's control point.

Consequently, eq. (3.41) added another one-column matrix to eq. (3.39) as  $RHS_3$ . This one-column matrix was:

$$RHS_3 = \begin{bmatrix} \sum_{m=1}^M d_{n_w,m} \mu_{n,m_v} \\ \vdots \\ \sum_{m=1}^M d_{N_w,m} \mu_{N,m_v} \end{bmatrix}, \quad (3.42)$$

where  $N$  is the total number of panels,  $M$  is number of wake strips and  $\mu_{n,m_v}$  is the difference between the velocity potential of the upper and the lower panels at the T.E. To find the doublet strength at the immediate shed wake panel, eq. (3.41) was used, instead of eq. (3.36).

It was found that averaging the immediately shed doublet strength improved the prediction on the velocity and pressure distribution on the foil, especially for a foil in

sinusoidal motion. In most cases, the above approach reduced the pressure difference at the trailing edge making the steady Kutta condition more feasible. This was formulated as:

$$\mu_{average} = \frac{\mu_w(t) + \mu_w(t-1)}{2} = \frac{[\mu_{upper}(t) - \mu_{lower}(t)] + \mu_w(t-1)}{2}. \quad (3.43)$$

Eq. (3.39) was further written as:

$$\begin{bmatrix} (d_{1,1} - d_{w1,1w}/2) & \cdots & (d_{1,j} + d_{w1,1w}/2) & \cdots & (d_{1,j+(M-1)+1} - d_{1,Mw}/2) & \cdots & (d_{1,M+N} + d_{1,Mw}/2) \\ \vdots & \vdots & \vdots & \vdots & \vdots & \vdots & \vdots \\ (d_{2,1} - d_{w2,1w}/2) & \cdots & (d_{2,j} + d_{w2,1w}/2) & \cdots & (d_{2,j+(M-1)+1} - d_{2,Mw}/2) & \cdots & (d_{2,M+N} + d_{2,Mw}/2) \\ \vdots & \vdots & \vdots & \vdots & \vdots & \vdots & \vdots \\ (d_{M,j,1} - d_{wM,j,1w}/2) & \cdots & (d_{M,j,j} + d_{wM,j,1w}/2) & \cdots & (d_{M,j,j+(M-1)+1} - d_{M,j,Mw}/2) & \cdots & (d_{M,j,M+N} + d_{M,j,Mw}/2) \\ \vdots & \vdots & \vdots & \vdots & \vdots & \vdots & \vdots \end{bmatrix} \quad (3.44)$$

Consequently, eq. (3.42) was revised as:

$$RHS_3 = \begin{bmatrix} \sum_{m=1}^M d_{n,m} \frac{\mu_{n,m_y}(t) + \mu_{n,m_y}(t-1)}{2} \\ \vdots \\ \sum_{m=1}^M d_{N,m} \frac{\mu_{N,m_y}(t) + \mu_{N,m_y}(t-1)}{2} \end{bmatrix}. \quad (3.45)$$

It was noted that the wake doublet strength found at the previous time step was kept in memory and was used to find the average at the current time step.

Finally, the left-hand-side of the linear equation system was eq. (3.44) and the right-hand-side was  $RHS_1 + RHS_2 + RHS_3$ . This linear system was ready for a matrix solver. The wake doublet strength currently shed was then determined by eq. (3.43).

### 3-C-2 The matrix solver

An accurate, reliable and efficient matrix solver can significantly improve the speed of computational work, especially for time-domain applications in which the matrix solver is to be repeatedly used at least as many times as the number of total time steps. (In some iteration methods, either for fluid or fluid-structural equilibrium, the matrix may need to be generated and solved a number of times at each time step). The percentage of total elapsed time taken to solve the linear equation system in this OSFBEM program depends on several factors: the matrix size and its property; the selection of the solver; the accuracy requirement; the CPU and the bus speed; programming techniques; the number of total time steps and panel density. This percentage ranged from 30% to 90% for rigid foils. For flexible foils, this percentage was reduced because both doublet and source coefficient matrices need to be obtained at each time step.

In many computational jobs, coefficient matrices that were yielded from the integral-L.P.D.E are symmetrical and sparse. For these symmetrical, sparse matrices, there are a number of mature subroutines such as ITPACK, LAPACK, LINPACK, NAG, IMSL, etc. Most of these well written packages are easily downloaded from the Internet. However, in most cases eq. (3.44) was a dense coefficient matrix. This matrix is not symmetrical due to the imposition of the Kutta condition, wake effects and sometimes non-symmetrical 3-D geometry of the foil. Therefore, a highly efficient, reliable matrix solver that is suitable for asymmetric and dense matrices is then desirable.

A number of Gauss elimination subroutines for both real and complex linear equations are available. For large scale linear equation systems, the Gauss elimination method is usually less numerically efficient, and this becomes obvious when the matrix size is larger than 400 (Katz and Plotkin 1991). Another disadvantage is that this method requires a greater amount of DRAM (dynamic random access memory) for operation, at least as much as the size of the matrix multiplied by a precision factor (e.g., for single precision this factor is 4). When a shortage of DRAM is encountered, this method becomes unbearably slow even if a very little amount of virtual memory

is to be swapped. A test on a 486SX 33MHz machine with 4MB DRAM found that, for an  $800 \times 800$  matrix, a solution took about four hours for a Gauss-Seidal iteration method and about two days for a Gauss elimination method.

Many classical linear iteration methods, such as the Jacobi, Gauss-Seidal, and SOR (successive over relaxation) methods are stationary iteration methods. They have slow convergence rates and these rates also depend much on the property of the matrix and over relaxation parameter (Jennings 1977). The SOR method was used once to solve a matrix generated from this panel method with irregular geometry input and it did not converge.

In this computer program OSFBEM (oscillating foil boundary element method), the Bi-CGSTAB (BiConjugate gradient stabilized) method was used (Freund et al. 1991). A pseudocode of this method was presented by Barrett et al. (1994). The subroutine used in the OSFBEM was based on a subroutine downloaded from the NetLib, which requires more DRAM and more matrix manipulation than the one used in OSFBEM. It was revised for two versions: a) Using a row-by-row reduction scheme to solve a big matrix without using virtual memory swap. The revised subroutine reads one row at a time when the DRAM is limited in which case the matrix is stored in a binary file at each time step. Required DRAM is  $I * (7N)$  bytes, where  $N$  is the order of the matrix and  $I$  is the floating point precision. This avoided using virtual memory swap which would take a long time to solve a big linear equation system. b) A modified version to reduce the number of times of the matrix had to be manipulated. This is particularly helpful when the DRAM is not very fast<sup>4</sup> or the virtual memory swap was required in the case of a) above. This version requires that the computer put a full coefficient matrix into DRAM. The amount of required DRAM is then  $I * (N^2 + 7N)$  bytes. Version b) is much faster than a) but requires much more memory. Version a) was found very helpful during the two-year development stage of the OSFBEM. Version b) has been used since a machine, with a Pentium 120 MHz processor, 32 Mb 70-ns DRAM and 1 Gb hard drive at accessing time of 8 ms, was accessible.

---

<sup>4</sup>DRAM's speed usually ranges from 60 to 80 ns. A faster EDO RAM is becoming popular now.

Version b) above was used to compare with the SOR method. For the OSFBEM with a given input, the ratio of total elapsed time for the Bi-CGSTAB to the that for the SOR is 220:2617. In this case, the Bi-CGSTAB has over ten times the computing efficiency of the SOR.

To achieve a fast convergence rate, Bi-CGSTAB requires that the matrix be normalized. In the OSFBEM, this was done by dividing by  $d_{i,i}$  at each row for both the LHS and the RHS.

### 3-C-3 Calculation of hydrodynamic forces

The solution to the linear equation system is the distribution of doublet perturbation potential. The velocity profile was then calculated by differentiating the doublet velocity potential with respect to the two tangential vectors on each panel and its adjacent panels. Hydrodynamic loads, boundary layer growth, propulsive efficiency (the ratio of the output power to the input power) and thrust were then obtained with this given velocity profile.

To obtain this velocity profile, a simple differentiation scheme such as a central or backward finite difference method will do the job. However, the velocity cannot be obtained at the control point of an end panel if backward or forward differences are used; either central or backward difference schemes may lose one point at each section (or inaccurately predict the velocity on the two end panels at the trailing edge of each section). Maskew (1987) used a surface quadratic formulation to get around this problem. In OSFBEM, an orthogonal-line quadratic formulation is used. While this method requires less computing power, it substantially improved the velocity distribution at both the leading edge and the trailing edge compared with the backward or forward difference scheme.

This scheme was first to locate the three values of the adjacent doublets, these values were then used to determine the coefficients  $a$ ,  $b$  and  $c$  of a parabolic function by solving  $3 \times 3$  linear equations. The tangential velocities were obtained by differentiating these two quadratic equations with respect to their two directions, exactly. At boundaries, values of the two closest adjacent panels were used; in the middle, values

of the doublet distance were taken from the immediately adjacent panels. This scheme is best to use for a structured<sup>5</sup> panel grid arrangement. For a non-structured panel grid layout, such as triangular surface panels, some special treatment is necessary.

With these perturbation tangential velocities,  $\vec{V}_p(V_{pi}, V_{pj}, V_{pk})$ , the total velocity based on the body frame at each panel  $l$  was obtained (p. 501 Katz and Plotkin 1991) by:

$$\vec{V}_l = \vec{V}_\infty(V_X, V_Y, V_Z) \cdot \vec{n}_l(i, j, k) + \vec{V}_l(V_i, V_j, V_k), \quad (3.46)$$

where  $i$ ,  $j$ , and  $k$  are in the panel local coordinate system<sup>6</sup>, the total kinematic velocity  $\vec{V}_\infty$  is a velocity due to motion of the foil and is projected onto the panel coordinate system. In this method, as discussed in a previous section, the strength of the source was given by eq. (3.22) and the perturbation normal velocity was given by  $\sigma_l = (V_k)_l$  so that they cancel out to satisfy the boundary condition: velocity normal to a panel on the body frame is zero. There was no axis transformation matrix operation needed as all manipulations were performed by vector operations.

The total velocity at each panel was then the modulus of eq. (3.46). With this velocity, the pressure coefficient  $C_p$  on each panel was obtained (Katz and Plotkin 1991) from:

$$C_p = 1 - \frac{|\vec{V}_l|^2}{|\vec{V}_\infty|^2} - \frac{2}{|\vec{V}_\infty|^2} \frac{\partial \Phi}{\partial t}. \quad (3.47)$$

The last term of eq. (3.47) can be obtained in a number of different ways. A simple approach is using backward finite differences:

$$\frac{\partial \Phi}{\partial t} = \frac{\mu_t - \mu_{t-1}}{t - t_1}, \quad (3.48)$$

<sup>5</sup>A structured panel layout is prepared according to a number of columns and rows, though the size and the shape of the panel may vary. In the present method, the trailing edge side of the upper and lower surface panels coincides each other. Unstructured panel arrangement will cause certain numerical difficulties in applying the trailing edge Kutta condition or finding the trailing edge pressure differences.

<sup>6</sup>The panel unit vectors,  $\vec{i}$ ,  $\vec{j}$  and  $\vec{k}$ , were obtained in terms of the global frame, i.e.,  $\vec{i}(X, Y, Z)/\sqrt{X^2 + Y^2 + Z^2}$ ,  $\vec{j}(X, Y, Z)/\sqrt{X^2 + Y^2 + Z^2}$  and  $\vec{k}(X, Y, Z)/\sqrt{X^2 + Y^2 + Z^2}$ .

where, in this doublet-source method,  $\Phi$  is equivalent to  $\mu$ . In the development of the OSFBEM, it was found that using finite-differences to find the doublet time derivative had a slow convergence rate (i.e., it required more time steps to get an acceptable degree of accuracy). More noticeably, for an oscillating foil in sinusoidal motion, the time history of the strength of  $\mu$  at each panel is also curvilinear. Therefore, the slope is better described by a polynomial. This was done by polyfitting three  $\mu$  values (one at the current time step, two at previous time steps) to a quadratic function. The time derivative was then found by differentiating the quadratic function exactly. Mathematically, the difference between these approaches vanishes when the time step size approaches zero, but, when the time step size is larger, this method converges faster. Using a higher order polynomial might be better for convergence, but it is necessary to solve a set of higher order linear equations for each panel at each time step. This in turn, increases the CPU demand.

The load normal to the panel (based on an inertia frame) at each panel  $l$  was then obtained from

$$\vec{F}_l = -(C_p)_l (A_{panel})_l \vec{k}_l(X, Y, Z) E, \quad (3.49)$$

where  $E$  is the reference dynamic pressure,  $\frac{1}{2}\rho|\vec{V}_\infty|^2$  and  $(A_{panel})_l$  is the panel area.

The sectional lift coefficient was calculated by:

$$c_l = -\frac{1}{A_{section} E} \sum_{j=1}^J F_l(0, 0, Z), \quad (3.50)$$

where  $A_{section}$  is the foil spanwise sectional area which is independent of foil thickness and  $J$  is the total number of chordwise panels.

Sectional thrust (also drag in an ideal fluid for a steady foil) was then calculated in similar manner:

$$c_t = -\frac{1}{A_{section} E} \sum_{j=1}^J F_l(X, 0, 0), \quad (3.51)$$

and the sectional moment coefficient was determined from:

$$c_m = -\frac{1}{A_{section} E c_{local}} \sum_{j=1}^J [(X_i - X_{pitch}) F_l(0, 0, Z) - (Z_i - Z_{pitch}) F_l(X, 0, 0)], \quad (3.52)$$

where  $c_{local}$  is the local chord length and  $X_{pitch}$  is the pitching axis location based on the global frame. For a small angle of pitch amplitude oscillation, the second term in eq. (3.52) may be neglected. Results from the calculation indicated that the effect of this term on total propulsive efficiency is very small (For an angle of attack of about  $10^\circ$ , the difference was usually less than 1%). For steady flow, this pitching axis position was automatically set at 25% root chord by the computer program.

Total lift  $L$ , thrust  $T$  and pitching moment  $M$  at each time step were then determined from

$$L = \sum_{j=1}^J (c_l)_j (A_{section})_j \quad (3.53)$$

$$T = \sum_{j=1}^J (c_t)_j (A_{section})_j \quad (3.54)$$

$$M = \frac{\sum_{j=1}^J (c_m)_j (A_{section})_j (c_{local})_j}{\sum_{j=1}^J (A_{section})_j (c_{local})_j} \quad (3.55)$$

### 3-C-4 Consideration of viscous effects and skin friction coefficient $C_f$

Boundary layer separation has substantial effects on hydrodynamic forces and propulsive efficiency. These effects, however, have not been quantitatively identified as a function of a variety of parameters such as aspect ratio, Reynolds number, roughness, sectional shape, planform geometry, forward swimming speed, reduced frequency, feathering parameter, deflexions, many of the factors, etc. They are too complicated to consider exactly. Though many studies have been done on experimental aspects, their results are by no means able to predict the flow phenomena for the oscillating foils in this study. Detailed study of all viscous effects is beyond the scope of this

research project. However, boundary layer separation effects on the flow pattern of the foil were qualitatively controlled according to previous results as described in the next few paragraphs.

In this method, a numerical prediction of boundary layer growth was made, mainly for the following purposes:

1. To compare the boundary layer growth between a rigid and a flexible foil. By doing so, it may allow the flexible foil to have a smaller pitch amplitude<sup>7</sup> and a higher heave amplitude to have a fair comparison (the same degree of separation or boundary layer growth). Usually, due to the chordwise bending moment of the flexible foil section, the instantaneous angle of attack of such a foil is much less than that of a rigid foil; thus, it is less prone to have a boundary layer separation. This method did not intend to determine the exact viscous effects on the boundary layer separation and dynamic stall.
2. To obtain a relatively accurate skin friction coefficient before boundary layer separation occurs.

Re purpose #1 above, it was decided to examine whether the flexibility of the foil would delay the boundary layer separation and, if so, how much delay. This examination was also useful to select the oscillating parameters to avoid a severe boundary layer separation in cooperation with the previous experimental studies. Re purpose #2 above, it was not intended to obtain a precise skin friction coefficient if separation occurs. However, it was intended to obtain a coefficient of skin friction more accurate than a rough assumption for a foil for all kinds of motion.

Based on the above reasons, a subroutine for the boundary layer effects was added to the OSFBEM. The formulation of the subroutine was based on Moran's (1984) 2-D steady flow approach. The assumptions were as follows:

- Each strip section of the foil resembles a 2-D wing section.

---

<sup>7</sup>In most cases, the larger the pitch amplitude, the smaller the instantaneous angle of attack.

- The tangential velocity downstream was then the velocity in the calculation of the velocity gradient.
- The cross flow velocity (another tangential velocity across the span) was neglected. This may affect the accuracy for small aspect ratio foils and for flow at the tip.
- Reynolds number was determined by taking the root chord as the characteristic length and the foil advance velocity as the reference velocity.
- The flow at each time step was assumed to be steady for the purposes of the calculation and this simulated a steady flow at each time step. The effect of the motion history on the boundary layer growth was neglected.
- The stagnation points were approximately taken at the extreme points at the leading edge and the trailing edge.
- The skin coefficient,  $c_f$ , was obtained first for each panel. This value stays where both laminar and turbulent separation occur because  $c_f$  is maximum there to have a conservative estimation and a method to evaluate the  $c_f$  at separation was not available yet; and, for an immediate separation, this value was calculated by using Blasius formula (p. 140 Schlichting 1979) for laminar separation and by using eq. (21.11) of Schlichting (1979) for turbulent separation. A leading edge separation may be allowed because it does not affect the loading sufficiently to eliminate the possibility for an unsteady foil (p. 478 and 525 of Katz and Plotkin 1991).

As the theoretical background of the above method in 2-D respects was discussed in detail by Moran (1984), the boundary layer growth starts at a stagnation point at the leading edge. In the laminar flow region,  $c_f$  was calculated by using Thwaites method; at the transition point, Michel's method was applied. The  $c_f$  at each panel, in turbulent flow, was obtained by Head's method.

At each time step, the total skin friction coefficient  $C_f$  was calculated by

$$C_f = \frac{1}{A_{foil}} \sum_{n=1}^N (c_f)_n (A_{panel})_n, \quad (3.56)$$

where  $N$  is total number of panels. This value of  $C_f$  was then used to modify the total thrust for input power calculation at each time step.

### 3-C-5 Efficiency and mean thrust calculation

The coefficient of friction was approximately taken as a reduction on the thrust, though they are not in opposite directions. This may allow a conservative prediction on the efficiency. Therefore, in each time step, the net thrust was calculated by:

$$T_i = \sum_{m=1}^M [(c_t)_m - (c_f)_m] (A_{section})_m, \quad (3.57)$$

where  $M$  is the total number of sections and  $i$  is a time step index.

The trapezoidal rule was used to calculate the mean thrust in an oscillatory cycle that consisted of a number of equal time steps.

The efficiency,  $\eta$ , is the ratio of output power to input power. The instantaneous input power at the  $i$ -th time step was calculated from

$$(P_{input})_i = M_i \dot{\alpha}_i - L_i \dot{h}_i, \quad (3.58)$$

where  $M$  is the pitch moment about the pitching axis,  $\dot{\alpha}$  is the velocity of pitch,  $L$  is the total lift and  $\dot{h}$  is the velocity of the heave motion at the  $i$ -th time step. The mean input power was also obtained using the trapezoidal rule.

The instantaneous output power is the product of the advance velocity of the foil and the thrust  $T_i$ .

The propulsive efficiency was finally obtained via the trapezoidal rule:

$$\eta = \frac{\sum_{i=1}^I (P_{output})_i + \frac{1}{2} [(P_{output})_1 + (P_{output})_I]}{\sum_{i=1}^I (P_{input})_i + \frac{1}{2} [(P_{input})_1 + (P_{input})_I]}. \quad (3.59)$$

It was noted that the mean input power and mean output power had to be calculated separately over the period. At certain time steps, the moment had the same

rotational direction as the angular velocity of pitch; thus, the instantaneous input power was negative (The stored energy did the work); at a zero instantaneous angle of attack, the thrust is negative due to pressure difference and the skin friction (extra thrust was needed to push the foil forward) so that the output was negative. These values should be held and be evaluated along with others in the whole period to yield practical input and output power.

### 3-C-6 Computing considerations and the procedure

Theoretical study and mathematical formulation are both essential to a computational fluid dynamics job. However, without a basic understanding of computer software, hardware and necessary techniques, numerical modelling cannot be realized, or, at least, results cannot be obtained in a reasonable time. The development of the early version of PMARC (Katz and Plotkin 1991) is such an example. If the binary file storing the matrices were not applied and the matrices were not solved by row-by-row reduction, it would not be possible to run it on a PC about ten years ago. Of course, this is not really necessary today for most of computing tasks. Computer knowledge helps to take advantage of new hardware and software technology and to avoid a waste of existing resources. This is particularly important in the case where the resources are limited.

A computer program package was produced to fulfil the computational tasks required by this research project. It consisted of four main parts:

1. Data input worksheet, JobInput. An ASCII file with templates and explanations to instruct the user for data input. This worksheet was designed for user-friendliness and for improving efficiency in batch jobs which required a huge amount of work. Data were inputted below the explanation lines. These data are in the following categories:
  - Sections of foil geometry offsets. Data inputted in this way were to make it easy to change the aspect ratio and thickness ratio of the foil. To change thickness and aspect ratios, only  $N$  number of values needed to be changed,

where  $N$  was the number of input section offsets. The planform shape was also easy to change by alerting  $2N$  values (the leading edge and the trailing edge  $x$ -offset).

- Oscillating parameters. These included the motion state (steady, unsteady or flexible), oscillatory speed, pitching amplitude, pitching axis location, heave amplitude, chordwise and spanwise deflexion equations and amplitudes, etc.
- Panel grid number and spacing across the span and chord. Nine combinations of panel spacing schedules were implemented, i.e., equal, cosine and log spacing in these two directions.

This input worksheet was also designed for repeated computations in which the input data and the dimension array sizes were different from one computation to another, without reformatting, linking the source program. In other words, an executable file OSFBEM.EXE will do them all.

2. Panel grid generation program, JobContr.FOR, a Fortran program to generate the panel corner points and to process the input data from the input data worksheet. As this program needs a large number of dynamic arrays and a fast CPU(s), it was designed to be separated from the main program for the hydrodynamic calculation. This arrangement enables the user to see the generated panel geometry before the job is sent for long hours of hydrodynamical computations, when desired. Its input file is the worksheet JobInput. It outputs the following files:

- A JobCorPt.BDF to be read by the main program. It includes all necessary information for hydrodynamic calculations.
- A 3-D surface panel file JobPanel.DXF in an ASCII or binary DXF format. This can be inputted to a CAD package such as AutoCAD to examine the generated surface panels. When needed, it can be directly downloaded to a computer that is linked to a CNC cutting machine to make a foil or an arbitrary 3-D surface.

- A polyline wire-frame DXF file JobGrid.DXF. This serves the same purpose as the surface panel file, but as an alternative.

These DXF files enable a user to have a close examination of the 3-D foil modelled in terms of surface panels. Errors in geometry may be corrected before sending the data to the main program for hydrodynamic calculations.

The dimension array sizes are declared dynamically (through the WATCOM F77/386 V. 9.01 compiler). This enables the compiled executable file to take different input data without reformatting and linking the source code, saving time and increasing portability.

3. The main program, OSFBEM (oscillating foil boundary element method). This program reads in the input data file JobCorPt.BDF and performs computations following the approaches and procedures discussed in previous sections. The array sizes were also declared dynamically, so that memory can be released by de-allocating some arrays and the program can take different input data without recompiling the source code.

The main output of the OSFBEM is OSFBEM.LOG. Output items are adjustable by changing the settings in the input worksheet file JobInput.

4. Pre- and post processing programs. These short programs were written to generate the NACA 4-digit foil sections, translating binary output from the OSFBEM to DXF format, retrieving specific values from the OSFBEM.LOG (to rearrange results for plotting without re-computing), and manipulating the binary file generated by AXUM (a plot package) for interfaces. These short programs were written in Borland C/C++, QuickBASIC and Fortran. They were designed to work under DOS for portability and speed. Computer languages were also selected in terms of their capability and time efficiency.

Computing procedures in the OSFBEM are listed below. They are

1. Dynamic array declarations (blank arguments).

2. Reading data from input file JobContr.BDF
3. Calculating all required array sizes and allocating them.
4. Finding neighbour panels for each panel. By the end of the program, panel flags will be used in differentiation of the doublet velocity potential to obtain two tangential velocities.
5. Changing the body frame origin to the pitching axis location if flow is not steady. This procedure finds the panel corner points and control points in the inertia frame.
6. Determining the starting wake corner points and recording them for output to a binary file OSFBEM.PAT (Using a binary file will save about 75% storage space and increase 5 times the data flow speed while retaining a double precision accuracy.) Recording the panel corner points and outputting them to a binary file OSFBEM.STP. These files will be translated to DXF format for graphical examination by other programs.
7. Transferring global corner points to panel local corner points. These Cartesian axes on each panel are expressed in terms of three vectors based on the inertia frame.
8. Finding the doublet coefficient and source coefficient matrices.
9. Initializing values and starting the time step loop.
10. Starting the time loop. Finding the instantaneous origin of the foil body frame and pitch angle.
11. For a flexible foil, finding the deflexions and relative velocities due to these deflexions.
12. Finding global values of panel corner points (on inertia frame); transferring panel corner points from the inertia frame to panel local frame.

13. For a flexible foil, calculating the doublet coefficient matrix and source coefficient matrix.
14. Finding the panel local velocities due to translation, rotation and deflexions based on the foil body frame. Transferring body frame velocity to global velocity.
15. Finding the panel local velocity referred to the panel's local Cartesian frame  $\vec{u}_i$ ,  $\vec{u}_j$  and  $\vec{u}_k$  (the unit vectors).
16. Calculating the fixed source strength (to yield the  $RHS_1$ ) by multiplying the source coefficient matrix by the normal component of the body local velocity. The source coefficient matrix for a flexible foil has to be obtained at each time step.
17. Determining the newly shed wake panel corner points and outputting them to OSFBEM.PAT. These corner points are also stored in memory for wake doublet coefficient matrix calculations.
18. Outputting panel corner points in the global frame to OSFBEM.STP.
19. Transferring global values of the newly shed wake panel corner points to the panel local frame. These values will be used to modify the foil body doublet coefficient matrix to fulfil the Kutta condition.
20. At  $t > t_1$ , transferring global values of previous wake panel corner points to panel local corner points and finding the doublet coefficient matrix due to these wake panels. Using this matrix, along with the doublet strength values corresponding to these coefficients, to find the  $RHS_2$ .
21. Applying the steady Kutta condition (Morino Kutta condition); further modifying the double coefficient matrix due to body panels by taking the T.E. potential jump into account; modifying the doublet coefficient matrix by averaging the newly shed and last shed wake panel doublet strength to yield a new doublet

coefficient matrix and a new  $RHS_3$ , at each time step. This is a one-step operation, though it was discussed in number of steps in the previous section in this Chapter.

22. Normalizing the doublet coefficient matrix; finding the right-hand-side of the linear system  $RHS = RHS_1 + RHS_2 + RHS_3$  and normalizing it too.
23. Solving for the unknown doublet strength distribution on the foil.
24. Determining the doublet strength of the newly shed panels.
25. Finding tangential velocities by using the panel neighbour flags, panel geometry values and doublet distribution.
26. Finding the panel total velocity and reference velocity.
27. Finding the derivative of the doublet potential at each panel.
28. Determining the pressure coefficient  $C_p$  and hence the loads.
29. Calculation of the boundary layer and skin coefficient  $C_f$ .
30. Recording time related variables, outputting the panel corner points at the last time step. Time loop ends here.
31. Calculating thrust and efficiency.
32. Outputting summaries; ending the program.

Verification of the program, convergence studies and certain special treatments for oscillating foil problems are described in the next chapters.

## Chapter 4

# Results and discussion: convergence and computing efficiency

Before obtaining any results for oscillating foils, a series of convergence studies and verifications were done. When the computer program OSFBEM was proven reliable, it was then used to perform a number of computations for oscillating foils.

A convergence study was first done for a steady, rigid foil, with regard to the time step size and the total number of panels. That is, the effect of time step size and panel number on lift and thrust was examined. Further, the effect of different panel spacings on lift and thrust were observed and several guidelines were obtained for both steady and unsteady flows.

The extensive convergence study was completed for several reasons. First, the combination of the panel density in the chordwise and the spanwise directions, the panel spacing arrangement in directions, the time step size and the number of time steps has a significant effect on the reliability and the accuracy of the predictions. Second, obtaining an acceptable accuracy of the results with less computing effort saves time and resources. Third, for a large scale numerical work, as the computing power of an IBM compatible Pentium processor PC with CISC architecture or a

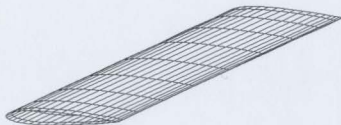


Figure 4.1: The panel geometry of a 3-D foil with an aspect ratio of 6 that was used in the convergence study with regard to the panel density arrangement.

UNIX workstation with a RISC processor (such as SuperSparc 5 or 10 or even a DEC alpha) is still inadequate, conservation of the resources is especially important.

## 4-A Panel density effects for a steady foil calculation

A rectangular NACA 0012 foil with an aspect ratio of 6 was used for the convergence study of the panel density and spacing. The sectional shape and one of the panel spacing arrangements (cosine-cosine for chordwise and spanwise direction) is shown in figure 4.1.

The chordwise panel intervals in figure 4.1 were taken as 20 and the spanwise panel columns as 10. The number of panels in either direction can be altered easily by changing one number in the input worksheet. The panel spacing arrangement can also be changed by changing a word in the input worksheet. Because the panel generation program was separated from the main program OSFBEM and several tool programs were written for interface with different software packages, panel generation and visualization were straight forward. A test was done on a Pentium 120 PC with 32 Mb on a PCI mainboard. For small panel numbers (about 10 by 20), when a batch program was used, it took about two minutes in total to revise the panel number and spacing, run the panel generation program, translate to a DXF file and display the graphics from within AutoCAD R12. About one quarter of the time was taken on

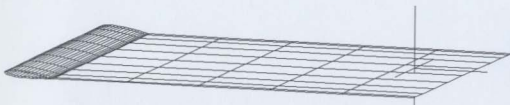


Figure 4.2: The foil with its shed wake. Each wake panel row stands for one time step in history.

starting the AutoCAD or it could have been even faster.

Figures 4.2 and 4.3 show the wake panels of such a foil and its instantaneous position in history, respectively. As was mentioned in Chapter 3, truncation of the immediate wake panel was not applied (Katz and Plotkin 1991). Instead, several different schemes were used. When these approaches were set active, the truncation of the immediate shed panel size had little effect on the load predictions.

Before performing any calculations for a different number of panels, a convergence study was done to select the fewest time steps necessary for a reliable result with an acceptable CPU efficiency.

Figures 4.2 and 4.3 also show that even if the foil was in steady motion, it was treated as if it were in an unsteady motion; i.e., the foil was moving constantly and marching with time steps, in a steady fluid.

The smallest number of time steps required to obtain an acceptable accuracy was about 5. As the starting vortex wake effect on the calculated hydrodynamic forces was significant, this number was dependent on the size of the time step to keep the

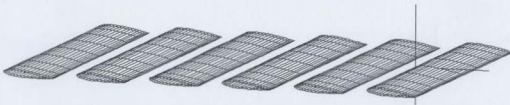


Figure 4.3: The instantaneous foil position in motion at each time step.

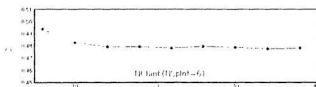


Figure 4.4: The lift coefficient  $C_L$  changes with the changes of the chordwise intervals NChInt at a fixed number of the spanwise intervals NSpInt=6.

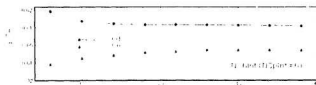


Figure 4.5: The calculated drag and the pitching moment coefficients  $C_d$  and  $C_m$  change with the changes of the number of chordwise intervals at a fixed number of the spanwise intervals at NSpInt=6.

foil far from the starting vortex wake. The distance from the starting vortex to the foil, should be usually greater than 50 times the root chord length.

For a rough calculation, in which only the lift coefficient and moment are important, a total of 5 time steps with 10 seconds step size, is sufficient. For a clear presentation, the time marching distance shown in figure 4.2 is much smaller than it was in practice. Also, the intervals between each instantaneous position shown in



Figure 4.6: The lift coefficient  $C_L$  changes with the changes of the spanwise intervals NSpInt at a fixed number of the chordwise intervals NChInt=6.

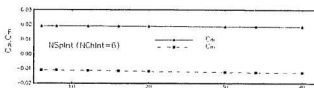


Figure 4.7: The calculated drag and the pitching moment coefficients  $C_{di}$  and  $C_m$  change with the changes of the spanwise intervals NSpInt at a fixed number of the chordwise intervals NChInt=6.



Figure 4.8: The lift coefficient  $C_l$  changes with the changes of the chordwise intervals NChInt at a fixed number of the spanwise intervals NSpInt=10.

figure 4.3 are much larger than they actually were when an arrangement of 5 time steps with a 10-second step size was taken.

The angle of attack of the foil for all calculations was 0.1 rad or 5.7296°. The panel spacing arrangement for the results presented in figures 4.4 and 4.5 was cosine in both chordwise and spanwise directions. In these two figures, NSpInt is the total number of the spanwise panel intervals, and NChInt is the total number of the chordwise intervals. The total number of the sectional chordwise panels is NChInt  $\times$  2, including both the upper and the lower surfaces. It can be seen that when NSpInt was taken as a small number (6) the lift coefficient reached to about 0.47 (a converged value in this case is about 0.45). As the value of NSpInt was small, convergence cannot be obtained.  $C_{di}$ , the drag in an ideal fluid, and  $C_m$ , the pitch moment coefficient (about 0.25 $C_r$ , where  $C_r$  is the root chord) also showed a fake convergence. This indicates that if the number of the spanwise panel is taken as a small number, increasing the

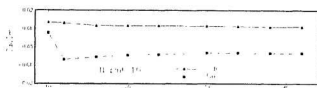


Figure 4.9: The calculated drag and the pitching moment coefficients  $C_d$  and  $C_m$  change with the changes of the number of chordwise intervals at a fixed number of the spanwise intervals at  $NSpInt=10$ .

panel intervals in the chordwise direction will not improve the convergence rate<sup>1</sup> on the lift coefficient.

As shown in figures 4.6 and 4.7, when the panel density was changed to 6 panel intervals across the chord with a total number of panels of  $NChInt \times 2 = 12$ , increasing the spanwise panel density increased the convergence rate for the lift coefficient  $C_l$ . However, with such a small number of chordwise panels (12 in total), the nonviscous drag coefficient  $C_{di}$  and the pitch moment coefficient  $C_m$  stayed almost at the same value; i.e., they had a poor convergence behaviour.

It was seen that the number of spanwise panels had a significant effect on the convergence of the lift. This might be caused by increasing the number of the spanwise

<sup>1</sup>The 'convergence rate', or the 'convergence speed' mentioned in this thesis means that how fast a result reaches a converged value with regard to the number of the panel intervals, the number of time steps or the number of the iterations, if any. A good convergence rate, or a fast convergence speed will show an ability of the results reaching a value and having a very small change when the number of panel intervals, the number of time step size, etc., increase significantly.



Figure 4.10: The lift coefficient  $C_l$  changes with the changes of the spanwise intervals  $NSpInt$  at a fixed number of the chordwise intervals  $NChInt=10$ .

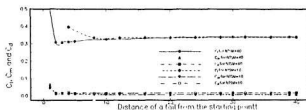


Figure 4.11: Time convergence behaviour with regard to the number of time step and the time step size. The results were obtained from a rectangular foil with an aspect ratio of 4. To eliminate the effect of the panel spacing on the accuracy, 40 chordwise and 20 spanwise panels were arranged.

wake strips. However, as the wake matrix takes an amount of memory in bytes equal to  $(NSpInt)^2 \times NChInt \times 2 \times NTSM \times I$ , where  $I$  is a precision parameter (for single precision,  $I=4$ ), increasing the number of wake strips will require substantially more computing power and DRAM. As will be discussed later in this chapter, for oscillating foil calculations, the CPU and the DRAM were barely adequate, even though a Pentium P120 processor with a 32 Mb DRAM on a PCI local bus and EIDE I/O controlled mainboard was employed. Also, this result suggested that using a high number of the spanwise panels will not effectively improve the convergence rate of the thrust (the drag is the negative thrust in oscillatory motion).

Figures 4.8 and 4.9 show the convergence rates for the lift, thrust and pitching moment coefficients, at a constant spanwise panel number of 10. The panel spacing

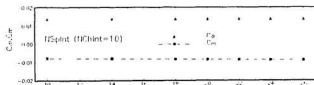


Figure 4.12: The calculated drag and the pitching moment coefficients  $C_{di}$  and  $C_m$  change with the changes of the spanwise intervals  $NSpInt$  at a fixed number of the chordwise intervals  $NChInt=10$ .

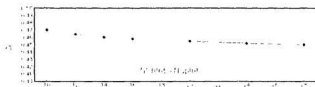


Figure 4.13: The lift coefficient  $C_l$  changes with the changes of the number of the chordwise intervals (NChInt) being equal to the spanwise intervals (NSpInt).

in both directions were cosine, where each panel boundary was determined by

$$x_i = \frac{(c_{\text{root}})_i}{2} \cos \theta_i, \quad (4.1)$$

and

$$y_j = \frac{s_{\text{half}}}{2} \cos \beta_j, \quad (4.2)$$

where  $\theta_i = i \times 180/(\text{NChInt})$  and  $\beta_j = j \times 180/(\text{NSpInt})$ .

When the number of the spanwise panels remained constant at 10, increasing the chordwise interval NChInt had little effect on the rate of convergence of the lift coefficient. However, the convergence rate on the pitching moment  $C_m$  was significantly improved. As can be seen later in this chapter, a fast convergence rate on the pitch moment will speed up the convergence rate on propulsive efficiency.

Figures 4.10 and 4.12 show that when the number of chordwise panels was fixed,

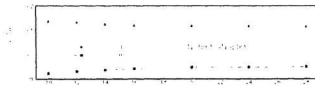


Figure 4.14: The calculated drag and the pitching moment coefficients  $C_d$  and  $C_m$  change with the changes of the number of the chordwise intervals (NChInt) being equal to the spanwise intervals (NSpInt).

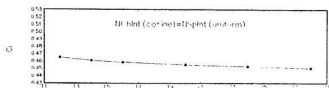


Figure 4.15: The lift coefficient  $C_l$  changes with the changes of both the number of cosine chordwise intervals and the number of the uniform spanwise intervals.

increasing the spanwise panel NSpInt increased the rate of convergence on the lift coefficient and slowed the rate of convergence on the thrust/drag and pitch moment coefficients. It also can be seen that the convergence speed, for the lift coefficient at a larger value of chordwise panel number (NChInt=10), became slow; i.e., the lift approached the limiting value. When NSpInt was taken to be above 24, the lift coefficient converged quickly to about 0.45. As was mentioned earlier, when the number of the chordwise panels is less than  $10 \times 2 = 20$ , the predicted thrust, drag and the pitching moment do not have an acceptable accuracy.

When it was seen that either using a small number of chordwise or spanwise panel numbers did not obtain an overall fast convergence rate, equal panel spacings in both directions were tested. The results for the same number of chordwise and spanwise intervals (the number of chordwise panels was then twice as many as that of the spanwise panels), is shown in figures 4.13 and 4.14. These three quantities (lift,

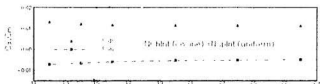


Figure 4.16: The calculated drag and the pitching moment coefficients  $C_d$  and  $C_m$  change with the changes of both the number of cosine chordwise intervals and the number of the uniform spanwise intervals.

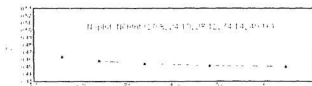


Figure 4.17: The lift coefficient  $C_l$  changes with the changes of a panel arrangement of the number of the spanwise panel intervals being 2.4 times of the number of the chordwise intervals ( $2.4 \cdot N_{ChInt} = N_{SpInt}$ ).

pitching moment and pressure drag/thrust coefficients) had a good convergence rate when the number of panel intervals was about 10 to 11. Above 16, they gradually approached a limit.

Up to this point, for the results to converge when using a relatively slow CPU and DRAM set up, the number of time steps in the motion was  $NTSM=5$ , the time step interval was about 10 sec. and the number of intervals in both directions was taken about the same (over 14). Using fewer time steps and increasing the time interval size increased computing efficiency. However, when the time interval was too large (aspect ratio of the shed wake panel being greater than 100), the shed wake panel became a line, and this affected the accuracy of the results. This numerical problem may be caused by inaccurate determination of the panel vectors and relative geometrical values. In such cases, double precision might be needed and this in turn, would have

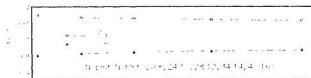


Figure 4.18: The calculated drag and the pitching moment coefficients  $C_{di}$  and  $C_m$  change with the changes of a panel arrangement of the number of the spanwise panel intervals being 2.4 times of the number of the chordwise intervals ( $2.4 \cdot N_{ChInt} = N_{SpInt}$ ).

increased the CPU demand and the amount of DRAM required.

A test was also done for different panel spacing arrangements across the span and the chord. When the chordwise panel spacing was taken as a uniform interval, the prediction was obviously poor at the leading edge and the trailing edge. Especially, at the leading edge, the slope of the pressure coefficient is in fact very large. Using a dense panel arrangement at these two edges, such as cosine, yielded a better prediction at a smaller total number of the chordwise panels. In contrast, using the uniform spanwise panel spacing resulted in a quicker convergence rate (see figures 4.15 and (4.16) for all three quantities at  $NChInt=NSpInt$ ). This may be due to the fact that the lift distribution across the span had a relatively flat slope and therefore, the cosine spacing was not optimal.

The log spacing in both directions was also tested. The log spacing along the chord was determined by

$$x_i = c_i(1 + \log(10i/N)) \quad (4.3)$$

where  $c_i$  is half of the local chord length and  $N$  is half of  $NChInt$ ,

and

$$y_i = s_i(1 + \log(10i/N)), \quad (4.4)$$

where  $s_i$  is the length of the half span. Figure 4.19 shows a log spacing for both the spanwise and the chordwise directions with  $14 \times 14$  panel intervals.



Figure 4.19: A log spacing arrangement for a rectangular foil with an aspect ratio of 3. Foil section is *NACA 0012* with both 14 chordwise and spanwise intervals ( $NChInt=NSpInt=14$ ).

The predictions by using log spacing in either or both directions yielded about the same results as that obtained by using the cosine spacing. Therefore, these results are not presented in this thesis.

As was mentioned above, increasing the number of the spanwise intervals improved the speed of convergence. A larger ratio of NSpInt to NChInt was also used to examine the convergence behaviour. One of several combinations was plotted in figures 4.17 and 4.18. For example, when the ratio was taken as 2.1, 20 : 8 means that there are 20 spanwise panels and  $8 \times 2 = 16$  chordwise panels. The total number of panels was then  $20 \times 16 = 320$ . It can be seen that using a panel arrangement of NSpInt=28 and NChInt=12, (i.e., 672 panels in total) resulted in a good convergence performance.

As all computations were done on PCs, improving the computing efficiency to save time and resources became very important.

For steady motion, a small total number of time steps and a bigger NSpInt number were desirable for both speed of the convergence and computing efficiency. The guidelines yielded from the convergence study are:

- The total number of time steps and the time interval had to be considered together. The foil had to be far from the starting vortex to eliminate the effect of this vortex.
- Too many time steps would reduce the computing efficiency; too few time steps and too large a time interval would have yielded a very large panel aspect ratio. When this ratio was too large, numerical difficulty occurred.
- Using more time steps improved the pressure profile across the chord (this will be discussed later in this chapter). Using a minimum of 50 time steps and a 1 to 2 seconds time interval gave a good overall computing performance; i.e., accuracy and computing efficiency.
- Using a larger spanwise panel number while keeping the NChInt larger than 10 yielded a good panel arrangement. Typically, the combination is no less than 16 and 8 (the number of the spanwise and the chordwise panel intervals being equal to 16 and 8, respectively, i.e., NSpInt=16 and NChInt=8).

For a steady foil, there was no computing power problem even if a 33 MHz 486 PC was used. Shortage of RAM was not problematic either. However, for unsteady motion, as the total number of time steps had to be very large (to keep a higher degree of validity of the steady Kutta condition), increasing the number of wake strips resulted in a dramatic increase in the computing power demand. The best arrangement was no longer the same as in the case of a steady foil where the situation had to be re-evaluated.

## 4-B Convergence study for an oscillating foil

Figures 4.20 and 4.21 show the instantaneous positions of an oscillating foil with an aspect ratio of 6. As was mentioned before, compared with the actual time step size of the moving steps, the time step size shown is very large; i.e., the actual positions of the foil had a very small step size and these positions almost overlapped each other.

As shown in figure 4.21, the instantaneous pitch angle and heave position at the starting point were set at zero and  $-h_{heave}$  respectively, where  $h_{heave}$  is the absolute heave amplitude. By doing so, the effect of the strength of the starting vortex was reduced to a minimum so that fewer oscillating cycles were required to obtain steady, periodical load values. It was seen that the foil at zero angle of attack in a sudden acceleration motion resulted in a minimum strength of the starting vortex. While keeping the pitch leading the heave, the oscillating governing equations were rewritten as

$$\alpha = \alpha_o \cos(\omega t) \quad (4.5)$$

for pitch and

$$h = h_o \cos(\omega t - \Phi_{phase}) \quad (4.6)$$

for heave. Reducing the total period by a half cycle reduced the number of time steps



Figure 4.20: Instantaneous position of an oscillating foil in motion. Viewing point at  $(0.00, -1.00, 0.00)$



Figure 4.21: Instantaneous position and panel geometry of an oscillating foil in motion. Viewing point at  $(0.05, -1.00, 0.10)$

and this improved computing efficiency by 20% because, when the total number of time steps increased, the elapsed time increased exponentially (see figure 4.25).

Figure 4.22 shows an oscillating foil with its shed wake sheet. The total number of time steps shown in figure 4.22 is 50. The period of the motion is  $2\pi$ . The period for a sinusoidal motion is governed by

$$T = \frac{2\pi}{\omega}, \quad (4.7)$$

where  $\omega$  is the angular velocity. This indicates that the larger the value of  $\omega$ , the shorter the period. In order to keep the Kutta condition valid, at least 100 step sizes may be required in such a short period.

It was noted that, while the phase angle was fixed, the phase shift in time is given



Figure 4.22: An oscillating foil with its shed wake in fluid.

by

$$T_{shift} = \frac{\Phi_{phase}}{\omega}, \quad (4.8)$$

where  $\Phi$  is the phase angle between pitch and heave. The period  $T$  mentioned above was considered important for the validity of the Kutta condition: the time step size was determined based on the period  $T$ .

The convergence study for an oscillating foil covers two aspects: the time step and the panel number.

There were several things concerning the time:

- Because the steady Kutta condition was used for unsteady foils, a small time step size was desired to make the steady Kutta condition valid. Computationally, the steady Kutta condition might be considered fully valid when the time step size approaches zero. This is obviously impossible. Therefore, for a better computing efficiency, the largest time step size allowing an acceptable accuracy needed to be determined.
- An oscillating foil has a cyclic motion. This presented another problem: to find the minimum number of cycles which would not cause the results to be affected by the starting vortex.
- Using a non-dimensional time (Katz and Plotkin 1991),  $t^* = \frac{y}{T}$ , may be necessary in studying a steady foil with a sudden acceleration at the initial stage of its motion. However, this non-dimensional time step size cannot reflect the angular velocity of an oscillating foil. This is simply because the  $t^*$  is not a function of  $\omega$ . The wake effect was believed to be associated with the oscillating frequency. Therefore, the higher the frequency, the smaller the time step size should be taken. Therefore,  $t^*$  was considered to be not a good parameter for a comparison.

In the OSFBEM, the total number of time steps was set for four cycles of the oscillation. For example, for  $\omega = 1.0$  rad/s, the period is  $2\pi$  sec and hence the total

time history is  $8\pi$  sec. When the time step size was set at zero in the input, the time step size would be automatically calculated based on the period in terms of the total given time steps.

A number of test runs showed that the same results were obtained in three cycles.

Some previous studies used a Newton-Raphson iteration scheme to improve the pressure distribution on the foil section in unsteady flow by obtaining an equal pressure on the upper and the lower trailing edge panels (Kinnas and Hsin 1992). This scheme improved the steady Kutta condition, especially the pressure difference at the trailing edge, but required more computing power, even if a matrix manipulation approach was used (Kinnas and Hsin 1992). However, the difference in lift, thrust and pitching moment coefficients, resulting from the approximation of the iterative Kutta condition was reported as unnoticeable. Meantime, for a flexible foil computation, if an iterative procedure is to be used, the high computing power required becomes a problem. This implies that at each time step, the coefficient matrices need to be regenerated due to the flexibility plus the iteration for the Kutta condition. Fyo and Kinnas (1994) pointed out that even if this scheme was used, for certain irregular panel geometry, the pressure distribution could not be improved as desired. In the calculation done here, no attempt was made to equalize pressure on the upper and lower surfaces at the trailing edge. The steady Kutta condition was used without modification. The reasons for this are as follows: a) the steady Kutta condition yielded accurate results when the time step and the size were chosen properly. These results included hydrodynamic loads; and b) the required high computing power became a concern when a flexible foil was under consideration.

An oscillating foil was used in a time convergence study. Its geometry and motion parameters are as follows:

- The number of chordwise intervals was  $NChInt=16$ ; which was equivalent to 16 chordwise panels.
- The number of the spanwise intervals was  $NSpInt=16$ . Total number of panels was 256.

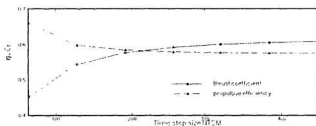


Figure 4.23: Time convergence study of the efficiency  $\eta$  and the thrust coefficient  $C_t$  vs. the total number of time steps NTSM.

- Uniform and cosine spacing were used for spanwise and chordwise panels respectively.
- The foil had a NACA 0012 section with an aspect ratio of 6.
- The heave amplitude factor was set at unity ( $h_o = h_{heave}/C_r = 1.0$ ).
- The apparent pitch amplitude was 0.16 rad ( $9.167^\circ$ ).
- The pitching axis position factor was set at unity ( $x_{pitch}^* = x_{pitch}/C_r = 1.0$ ).
- The phase angle,  $\Phi_{phase}$ , was  $90^\circ$  where pitch leads heave.
- The oscillating angular velocity was  $\omega = 1.0 \text{ rad/sec}$ .
- The foil forward swim speed was  $V_{flight}^* = V_{flight}/C_r = 1.0/\text{sec}$ .
- The reduced frequency was, then,  $k = \omega C_r/V_{flight} = 1.0$ .

There were a total of four cycles for all different total numbers of time steps. The number of time steps ranged from 64 to 448, with an increment of 64. When the angular velocity was  $\omega = 1.0 \text{ rad/sec}$ , the period was  $2\pi$  sec. Four cycles had a total time of  $8\pi$  seconds. The time step size was then from  $\frac{1}{8}\pi \approx 0.3927$  second to  $\frac{1}{50}\pi \approx 0.05610$  second. It can be seen from figure 4.23 that the propulsive efficiency  $\eta$  started to converge at about 200 time steps (with a change of 0.1%). However,

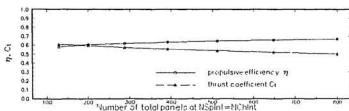


Figure 4.24: The efficiency  $\eta$  and the thrust coefficient  $C_t$  vs. the total number of panels with an arrangement of  $NSplnt=NChnt$  (the number of the chordwise panel intervals being equal to the number of the spanwise panel intervals) at a total of 256 time steps.

the thrust required more time steps at around 300 time steps to converge (about 5% increase from 320 to 384). The figure also shows that increasing the number of time steps resulted in the efficiency remained almost unchanged, but the thrust coefficient approached a limit of about 0.61. This indicates that, when using a smaller number of time steps, the propulsive efficiency can be well predicted but the thrust might be under-predicted and more time steps may be needed to obtain the same convergence rate for the thrust as for the efficiency.

Results from a convergence study on the number of panels are presented in figure 4.24. The total number of time steps was taken as 256. It can be seen that propulsive efficiency had an acceptable convergence behaviour starting from a total of 300 panels. However, for the thrust coefficient, a denser panel size was required. This suggested that a combination of a large number of time steps and a larger number of panels are required to obtain a satisfactory convergence on the thrust coefficient prediction. This would be computationally expensive. However, the thrust coefficient approached the upper limit as the number of time steps increased, and it became less as the number of panels increased. An appropriate combination of modest time steps and panel numbers is expected to yield an accurate result for engineering application.

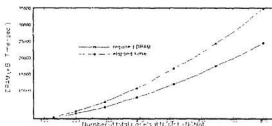


Figure 4.25: Required DRAM and elapsed time vs. the total number of panels with an arrangement of  $N_{SpInt}=N_{ChInt}$  (the number of the chordwise panel intervals being equal to the number of the spanwise panel intervals) at a total of 256 time steps.

#### 4-B-1 Computing efficiency and conservation of resources

Figure 4.25 shows the total number of panels versus required DRAM and total elapsed time. These results were obtained from a Pentium 120 MHz computer with 32 Mb DRAM. For a foil with  $20 \times 40 = 800$  panels, doing one computation for 256 time steps, about 24 Mb of DRAM and about 35,000 seconds computing time (about 10 hours) were required. From a trial on a 486 33 MHz machine with 4 Mb DRAM, it was found that it took about 350 hours or a half month to do the same computations. The CPU speed of the computer is also important. A Pentium 120 PC with PCI/ISA and built-in I/O had an overall throughput of seven times that of a 486 33 MHz box when the DRAM was enough for both.

If the amount of DRAM is not enough, binary files have to be used to store the matrices and row-by-row reduction has to be applied to solve the linear system. In this case, five times as much time is required for the OSFBEM.

#### 4-B-2 Summary

Considering both overall accuracy and computing efficiency, for oscillating foils, parameters should be chosen as follows:

- Use cosine panel spacing for chordwise panels with total of over 20 panels.
- Use uniform panel spacing in the spanwise direction with more than 16 spanwise intervals (NSpInt=16).
- Use 256 time steps for computation for four cycles of oscillation to yield an acceptable overall accuracy.

## Chapter 5

# Results and discussion: verifications and comparisons

To test the results from OSFBEM, numerical results were first compared with existing theoretical results, where these existed.

### 5-A Pressure distribution and lift coefficient of a 2-D foil

The test was first done on a 2-D NACA 0012 foil at angle of attack of  $8.3^\circ$ . The theoretical results were available for both the lift coefficient ( $C_l = 1.0$ ) and the pressure distribution (Moran 1984).

Figure 5.1 shows the pressure distributions obtained from a 2-D analytical method and from OSFBEM. The OSFBEM is a 3-D foil program. To simulate the 2-D section, the aspect ratio was taken as 1000. The number of time steps was taken as 100. The number of chordwise panels was 20 as was the number of spanwise panels. The spanwise panel spacing was uniform and the chordwise spacing was cosine.

It can be seen that the predicted pressure coefficients agree very well with the theoretical ones. The predicted lift coefficient is 0.9734. The OSFBEM, in most

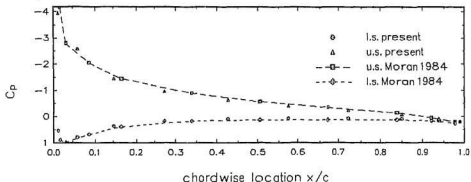


Figure 5.1: Pressure distribution  $C_p$  on a 2-D NACA 0012 wing at an angle of attack of  $8.3^\circ$ , which has a unit lift coefficient  $C_l$  of 1.0.

cases, gave a conservative prediction of the propulsive performance and the difference between the predicted values and the actual values was expected, in the worst case, to be under 5%. For this foil section, the predicted potential drag coefficient was 0.00822; the skin friction coefficient of the section was 0.00983 and the pitch moment coefficient about the 25% root chord was 0.0045. The pressure difference at the T.E. was about 0.003, a value close to zero, indicating the acceptability of the Kutta condition used.

## 5-B Pressure distribution at the tip of a 3-D foil

While it was relatively easy to obtain an agreement for 2-D steady foils, predictions were obtained from the present method for a 3-D steady foil with results of an experimental study (van Dam 1986). The foil had a NACA 0012 section with an aspect ratio of 6 at an angle of attack of  $6.75^\circ$ . Input parameters were: uniform spanwise spacing, cosine chordwise spacing, 14 spanwise panels, 40 chordwise panels, a total number of time steps of 5 and a time step size of 10 seconds. More chordwise panels were set at the trailing and the leading edges in order to have more data, because the experimental data were given in terms of  $\sqrt{x/c}$ .

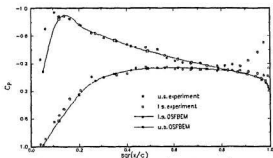


Figure 5.2: Pressure distribution  $C_p$  on a rectangular wing with an aspect ratio of 6 along the section close to tip at 98.75% semispan.

Figure 5.2 shows the comparison of the pressure coefficient along the extreme tip of the foil, at 98.75% semispan. Similar to the results by VSAERO, this method produced results which had a high degree of agreement with the experimental ones, except that there was a little difference in  $C_p$  at the leading edge on the suction side and there was a big difference between the predicted value and the experimental value of the pressure coefficient at the trailing edge on the suction side. The reason for this is unknown, perhaps crossflow, interference with tip vortex or separation accounted for the difference. However, the pressure coefficient from the experiment at the trailing edge shows that the pressure difference in reality was not zero; this conflicts with any kind of Kutta condition. This pressure difference is possibly caused

by the severe cross flow at the wing tip.

The spanwise distribution of pressure coefficient was also compared with the experimental results from the same wing presented by van Dam (1986). These results were in excellent agreement with each other (almost coinciding except a tiny discrepancy at the root chord section). Therefore, the plots are not presented here.

### 5-C Pressure distribution of a swept and tapered foil with 2% maximum thickness

Results from OSFBEM were also compared with those for foils that had certain irregular geometries. The results for a 2% thickness, thin, swept section, NACA 0002 wing at an angle of attack of  $5^\circ$  are an example of this. This foil had a sweep angle of  $30^\circ$ , an aspect ratio of 6 and a taper ratio of  $\frac{1}{3}$ .

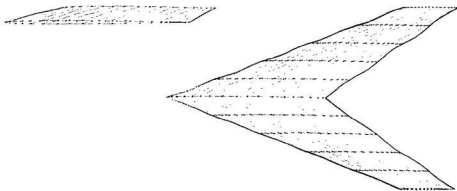


Figure 5.3: A 3-D surface panel geometry of a swept wing.

A 3-D view of the foil is shown in figure 5.3. The left graph in figure 5.3 shows this thin section which is located at a position of the root chord, right-most column and the right one shows an overview of the foil at a view point from  $(0.1, -1.0, 0.1)$ . In the figure, the number of total chordwise panels is 40 with a cosine spacing and the number of spanwise panels is 10 with uniform spacing.

Results along the middle semispan section (55% semispan) are presented in figure 5.4. General agreement can be seen between the methods, OSFBEM and VSEARO (Maskew 1982) except at the leading edge on the suction side. As the foil section's maximum thickness is only 2% of the chord, the leading edge is very sharp. A small radius to be placed on the leading edge is expected to smoothen the leading edge

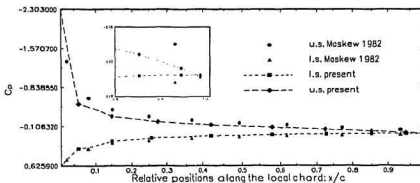


Figure 5.4: Pressure distribution  $C_p$  on a swept wing with an aspect ratio of 6 along the 54.9% semispan.

pressure distribution on the suction side. However, it can be seen from figure 5.4 that the present method produced a nearly zero pressure difference at the trailing edge. The enlarged trailing edge pressure distribution placed in the square box in figure 5.4 shows that predictions from previous studies including the ones by Maskew, the low order panel method and by Robert, the high order panel method (see Maskew 1982) had a substantial pressure difference at the trailing edge compared with the present method. Normally, a large trailing edge pressure difference reflects the poor application of the Kutta condition at the trailing edge, and this usually affects the pressure distribution at both the L.E. and the T.E., to a large extent.

## 5-D Efficiency and thrust from an oscillating foil

For an oscillating foil, as the accuracy of thrust and efficiency values are difficult to evaluate from an experimental study (for example, accurate measurement of thrust is a problem), experimental results are difficult to use to verify predictions. Therefore, results from experimental studies were not used for comparison. The propulsive efficiency and thrust from the OSFBEM without skin friction were compared with a previous lifting surface theory.

An oscillating foil with an aspect ratio of 8 in Chopra and Kambe (1977) was used in this comparison. The oscillating parameters are: forward swim velocity  $V_{flight}^* = 1.0$  m/sec; heave amplitude factor  $h_a = h_{heave}/C_r = 1.0$ ; pitching axis position factor is  $x_{pitch}^* = x_{pitch}/C_r = 0.75$ ; angular velocity  $\omega = 0.1 \dots 2.0$ ; pitch amplitude  $\alpha_a = 0.0$  and  $0.16$ ; reduced frequency  $k = \omega C_r / V_{flight}^* = 0.1 \dots 2.0$ ; and feathering parameter  $\theta = \alpha_a V_{flight}^* / [h_a \omega] = 0.0, 0.4$ .

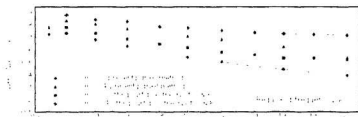


Figure 5.5: Comparison of efficiency  $\eta$  determined by calculated by lifting surface theory (Chopra and Kambe 1977) and that determined by the present panel method for an oscillating foil of aspect ratio 8.

Figure 5.5 shows the propulsive efficiency versus the reduced frequency  $k$ . It can be seen that both methods are in agreement on the trends, but the discrepancy between results by the two method becomes obvious when the reduced frequency  $k$  increases. These differences may result from the different methods. In the lifting surface theory of Davies (1965) which was used by Chopra and Kambe (1977), a small amplitude of both heave and pitch was assumed. At a large reduced frequency

which corresponds with a large angular velocity, the pitch amplitude is large when the feathering parameter is fixed; then the linearized lifting surface theory becomes less acceptable. At  $k = 2.0$ , the pitch amplitude  $\alpha_0$  is 0.8 rad. These two terms,  $\sin(\alpha)$  and  $\cos(\alpha)$ , that determine the heave and vertical velocity at the control point, become  $\sin(0.8) = 0.717$  and  $\cos(0.8) = 0.697$  for the present method and,  $\sin(0.8)$  and  $\cos(0.8)$  being assumed to be 0.8 and 1.0 respectively, for small amplitude theory. Therefore, the errors of the trigonometric functions (to be used to control the motions of the foil) for an  $\alpha_0$  of 0.8 rad are about 10% and 30% percent respectively. Another reason is that Chopra and Kambe (1977) did not consider the unsteady, large amplitude wake effect. As was tested in the computations, there was a substantial drop in both the thrust and efficiency when the wake effect was considered (Liu 1991). Meaningful results cannot be obtained from a panel method without taking the unsteady wake effect into consideration.

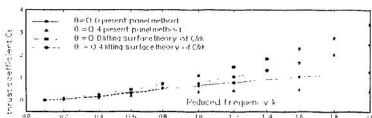


Figure 5.6: Comparison of the thrust coefficient  $C_t$  by lifting surface theory (Chopra and Kambe 1977) and present panel method for an oscillating foil of aspect ratio 8.

In figure 5.6, the thrust coefficients are compared. Though the two methods agree on the trends, they do not agree on the magnitudes. In a potential theory based method, the larger the angle of attack of the foil, the larger the thrust. At the same small amplitude feathering parameter of 0.8, the small amplitude theory has a maximum instantaneous angle of attack of  $20.92^\circ$  (see table 6.1) and the maximum instantaneous angle of attack for the large amplitude theory is about  $12^\circ$ . This substantially large difference in the angle of attack was the major cause of such a

large difference in thrust. At a higher feathering parameter and a larger angular velocity, the change of the strength of the shed vortex wake is rapid and hence the wake effect is substantially strong. A dramatic drop in both efficiency and thrust is expected at a very large feathering parameter (close to 1.0). The previous lifting surface theory work did not take this strong effect into consideration. Another cause of the substantially high thrust predicted, using the lifting surface theory, is the nature of the theory: i.e., zero thickness of the wing section is assumed. A thin (zero-thickness) wing section has a large leading edge suction and this suction also contributes to the thrust.

Using the present method, the values of propulsive efficiency and thrust, when the reduced frequency approached zero, decreased dramatically to zero. For the lifting surface theory, however, the efficiency went up to 100%. This may be explained as follows: in panel method, the foil has a "pressure drag" (a pressure difference calculated by using the panel method in the x-direction) all the time, and this drag always cancels a part of the thrust. In lifting surface theory a flat plate, moving in a fluid at an angle of attack of zero, has a zero drag; hence there is no power input required for the thin plate to move at any velocity. The panel method seems more practical here.

Figures 5.5 and 5.6 did not include the comparison at a feathering parameter of 0.8. It can be seen that when the root chord  $C_r$  and the forward swim speed  $V_{flight}$  were taken as a unit value, changing the reduced frequency  $k$  was equivalent to changing the oscillating frequency  $\omega$  because  $k = \omega C_r / V_{flight}$  (it is noted that many researchers define the reduced frequency as  $k = \omega C_r / \{2V_{flight}\}$ ). Therefore, at a high feathering parameter of 0.8 and the oscillating frequency,  $\omega = 2.0$ , the pitch amplitude calculated from the small amplitude theory reached 1.6 rad = 91.6°. It is impossible in reality for a pitch angle greater than 90° to yield a positive thrust.

In a large amplitude theory developed in this thesis, the instantaneous angle of attack is the angle between the instantaneous pitch angle and the instantaneous kinematic velocity angle of the foil pitch axis. In a practical range of the oscillating frequency  $\omega$  and the heave amplitude  $h$ , the larger the pitch angle, the smaller

the instantaneous angle of attack of the foil. A positive angle of attack is required to produce a positive thrust. This means that the angle of the kinematic velocity  $\tan^{-1} \frac{u_0 h}{V_{\text{pitch}}}$  has to be greater than the instantaneous pitch angle  $\alpha$ , i.e., the large amplitude feathering parameter  $\Theta$  has to be less than 1.0. For details, see Chapter 6-A and figure 6.1.

According to the present method, the predicted efficiency became ridiculous when the reduced frequency  $k$  reached 0.6 at  $\theta = 0.8$  because at this oscillating frequency the oscillating foil's instantaneous angle of attack was a negative value (the pitch angle is greater than the velocity vector) and was no longer able to produce thrust so that an external thrust was needed to keep the foil moving at a constant swim speed of 1.0 m/sec.

## Chapter 6

# Results and discussion: parametric analysis for rigid planforms

A study of the effects of variations of parameters on propulsive efficiency and thrust for a rigid oscillating foil was conducted. To have a full picture of the propulsive performance for a 3-D, non-zero thickness oscillating foil with different parameters, a number of calculations were done and they are presented below. The reasons for doing so are as follows:

Previous methods used for these calculations were based on either two dimensional theory or the small amplitude theory or both; a more realistic method, reflecting the aspect ratio, planform shape, sectional shape, large amplitude motion and viscous drag of an oscillating foil, was desirable. Because previous methods did not cover all the above factors, a re-evaluation and analysis of the full spectrum of parameters on the efficiency  $\eta$  and the thrust coefficient  $C_t$  is useful. A large amplitude theory was developed first below and was then used to explain the propulsive performance. The establishment of this large amplitude theory was found very useful to clarify a misleading concept. This conceptual confusion is that the pitch angle has been taken as a factor to affect the thrust and efficiency without considering the instantaneous

kinematic velocity for the pitch axis of the foil. Especially, some previous works mistook the instantaneous pitch angle as the instantaneous angle of attack.

The parameters, covered in the analysis, are heave amplitude factor  $h_o = h_{heave}/C_r$ , apparent pitch amplitude  $\alpha_o$  (the same as real amplitude for rigid foils), pitching axis position measuring from the leading edge at the root chord  $x_{pitch}^* = x_{pitch}/C_r$ , phase angle (pitch leads heave)  $\Phi_{phase}$ , sectional thickness ratio  $t^* = t_{max}/C_r$ , aspect ratio  $A$ , skin friction, and swept planforms of a man-made and naturally occurring planform.

A base combination of motion and geometry parameters was set. When studying each effect, only one parameter was set as a variable. This combination is as follows:

1. Rectangular planform with an aspect ratio  $A = 8.0$ .
2. NACA 0012 section with 12% thickness,  $t^* = 12\%$ .
3. Oscillating propeller forward velocity  $V_{flight}^* = V_{flight}/C_r = 1.0/sec$ .
4. Heave amplitude factor  $h_o = h_{heave}/C_r = 1.0$ .
5. Oscillating angular velocity  $\omega = 1.0 rad/sec$ .
6. Reduced frequency  $k = \omega C_r / V_{flight}^* = 1.0$ .
7. Absolute pitch amplitude  $\alpha_o = 0.4 rad \simeq 22.92^\circ$ .
8. Small amplitude feathering parameter  $\theta = \{\alpha_o/h_o\} \{V_{flight}^*/\omega\} = 0.4$ .
9. Large amplitude feathering parameter  $\Theta = \alpha_o / \tan^{-1}[\omega h_o / V_{flight}^*] = 0.5093$ .
10. Pitch leading heave at a phase angle of  $\pi/2 = 90^\circ$ .
11. Pitch axis factor  $x_{pitch}^* = x_{pitch}/C_r = 1.0$ .

In addition to the above parameters, all calculations were done using NTSM=256 time steps, NSpInt=20 spanwise panels with uniform spacing and NChInt $\times$ 2 = 20 chordwise panels with cosine spacing.

The individual effect of the variation of each parameter on the propulsion performance will be discussed in this chapter.

## 6-A A note on large amplitude theory

Since more than half a century ago, the small amplitude assumption or linearized theory has been used to solve aerodynamic problems for wings in gust and flutter. The reasons for using small amplitude theory are mainly: a) the foil under consideration often has a very small amplitude of pitch and heave, so that the accuracy of the results were acceptable; and b) solution for a large amplitude theory was difficult because the establishment of a non-linear system of equations or an analytical solution was not possible. For example, lifting surface theory is a linearized analytical solution.

In small amplitude lifting surface theory, the magnitude of heave and the downwash velocity are evaluated by assuming  $\tan(\alpha) \simeq \alpha$  and

$$\tan^{-1}\{\omega h_o/V_{flight}\} \simeq \omega h_o/V_{flight}.$$

Because of this, the feathering parameter becomes  $\theta = \alpha_o V_{flight}/(\omega h_o)$ . Unfortunately, this small amplitude assumption, as can be seen later in this chapter, has an unacceptable accuracy in many cases.

For oscillating foils, in addition to an inaccurate evaluation of the heave, which

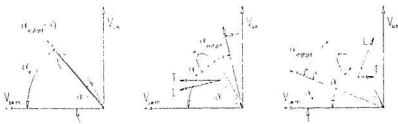


Figure 6.1: A graphical explanation of the instantaneous angle of attack using a large amplitude theory.

heavily affects the accuracy of the results at higher pitch amplitude, the small amplitude feathering parameter  $\theta$  also gives an excessive value of the pitch angle at a high feathering parameter.

As can be seen in figure 6.1, the feathering parameter is the ratio of the pitch amplitude to the angle  $\alpha_v$  (the instantaneous direction angle of the foil pitch axis' kinematic velocity), where  $\alpha_v$  is evaluated as a ratio of the maximum vertical velocity  $V_{\omega h} = \omega h_o$ , to the forward swimming velocity  $V_{flight}$ . When the phase angle is taken as  $90^\circ$ , this kinematic velocity will occur at the same position as the instantaneous pitch angle reaching the maximum value  $\alpha_o$ .

It is noted that the lift  $L$  produced by the foil has been defined as being perpendicular to the instantaneous kinematic velocity of the pitching axis. The thrust, however, is parallel to the horizontal.

The left graph in figure 6.1 shows the determination of the large amplitude feathering parameter

$$\Theta = \alpha_o / \alpha_v = \alpha_o / [\tan^{-1}(\omega h_o / V_{flight})]. \quad (6.1)$$

Consequently, the instantaneous pitch angle  $\alpha$  is equal to the instantaneous kinematic velocity of the pitch axis of the foil,  $\alpha_v$ , i.e., the large amplitude feathering parameter  $\Theta = 1.0$ . Therefore, the instantaneous angle of attack is

$$\alpha_{instant} = \alpha_v - \alpha = 0.0. \quad (6.2)$$

Therefore, the lift coefficient  $C_l$  and the generated thrust are both equal to zero for a symmetrical foil with no twist across the span.

The middle graph in figure 6.1 presents a feathering parameter of less than 1.0. In this case, the instantaneous pitch angle  $\alpha$  is less than the angle of the kinematic velocity,  $\alpha_v$ . Therefore, the generated thrust has a non-zero value and its direction is the same as the foil forward velocity.

The right graph shows an undesirable situation for a propulsor, in which the feathering parameter is  $\Theta > 1.0$ ; this is equivalent to producing a negative thrust, i.e., the instantaneous angle of attack

$$\alpha_{instant} = \alpha_v - \alpha < 0.0.$$

Reduced frequency $k$	0.2000	0.6000	1.000	1.400	1.800	2.000
$(\alpha_o)_s$ in rad	0.1600	0.4800	0.8000	1.120	1.440	1.600
$(\alpha_o)_s$ in deg	9.167	27.50	45.84	64.17	82.50	91.67
$(\alpha_{instant,max})_s$ in rad	-0.0400	-0.1200	-0.2000	-0.2800	-0.3600	-0.4000
$(\alpha_{instant,max})_s$ in deg	-2.292	-6.876	-11.46	-16.00	-20.68	-20.92
$(\alpha_o)_l$ in rad	0.1579	0.4323	0.6283	0.7604	0.8510	0.8857
$(\alpha_o)_l$ in deg	9.048	24.77	36.00	43.75	48.76	50.75
$(\alpha_{instant,max})_l$ in rad	-0.0420	-0.1081	-0.1571	-0.1906	-0.2127	-0.2213
$(\alpha_{instant,max})_l$ in deg	-2.262	-6.194	-9.000	-10.89	-12.19	-12.68

Table 6.1: Comparison of the maximum instantaneous angle of attack between small and large amplitude theory, at a fixed small amplitude feathering parameter of  $\theta = 0.8$ . Subscripts  $s$  and  $l$  stand for small and large amplitude assumptions respectively. The value of the maximum instantaneous angle of attack  $\alpha_{instant,max}$  may change with the change of the phase angle  $\Phi_{phase}$  between the pitch and the heave. Values given in this table are for the phase angle at  $\Phi_{phase} = 90^\circ$ .

To obtain a general picture of an error in feathering parameter in small amplitude theory, an oscillating wing with a reference length of 1, heave amplitude factor of 1,  $V_{flight}$  of 1/sec, and a fixed small amplitude feathering parameter of  $\theta = 0.8$ , was used to tabulate the values of the instantaneous angle of attack,  $\alpha_{instant}$ , with the changes in reduced frequency. From table 6.1, for small amplitude theory, the instantaneous angle of attack is already  $16.00^\circ$  at  $k = 1.4$ . At such a big angle of attack, separation will occur and the results are no longer meaningful. However, using the large amplitude theory, the instantaneous angle of attack is much smaller and the lifting flow around the foil might be still possible at a much larger reduced frequency say up to  $k = 2.0$ .

An instantaneous large amplitude feathering parameter  $\Theta_{instant}$  was defined in the form of

$$\Theta_{instant} = \frac{\alpha}{l \tan^{-1} \frac{\omega h \cos(\omega t - \Phi_{phase})}{V_{flight}}} \quad (6.3)$$

The value of this  $\Theta_{instant}$  should be less than 1 to obtain a positive thrust. However,

this instantaneous value may be larger than, but must be close to 1, even if the large amplitude feathering parameter  $\Theta$  is less than 1, because the phase angle had an effect on the instantaneous value (by shifting the phase of the numerator and the denominator in eq. (6.3)).

## 6-B Effect of heave amplitude on the efficiency and thrust

The effect of heave amplitude on the thrust and efficiency was observed and the results are presented in figure 6.2. The figure shows that the heave amplitude has a substantial effect on the thrust; the predicted thrust coefficient  $C_t$  ranges from 0.04 at  $h_o = 0.5$  to over 1.6 at  $h_o = 2.5$ . However, the efficiency drops gradually from 74% to 62%. It can be seen that the use of the large amplitude theory in this method gives an almost linear relation for both the efficiency  $\eta$  and the thrust coefficient  $C_t$ , and that, with an increasing the heave amplitude, the efficiency drops while the thrust coefficient increases. As an increase in the heave amplitude is equivalent to an increase in the angle of attack, i.e., a decrease in the feathering parameter  $\Theta$ , the thrust increased linearly.

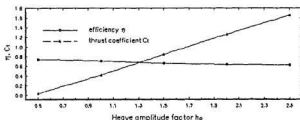


Figure 6.2: Effect of heave amplitude on the propulsive efficiency  $\eta$  and thrust coefficient  $C_t$  for a rigid rectangular oscillating foil with an aspect ratio of 8.

The trend of the efficiency in figure 6.2 is contrary to the conclusion by Yamaguchi 1992 (p.2). In the present method, higher heave amplitude results in lower efficiency, though the curve looks rather flat. This is also in agreement with the result by Liu and Bose (p.67-68, 1993), in which three naturally occurring planforms were examined using a small amplitude lifting surface theory. Increased thrust means an increased load of the propeller, and hence there is a drop in efficiency.

$h_o = h_{heave}/C_r$	0.5000	1.0000	1.5000	2.0000	2.5000
$\theta = \alpha_o V_{flight}^* / [\omega h_o]$	0.8000	0.4000	0.2667	0.2000	0.1600
$\Theta = \alpha_o / \tan^{-1}[\omega h_o / V_{flight}^*]$	0.8627	0.5093	0.4070	0.3613	0.3361
$\alpha_{instant,max}$	3.6450	22.080	33.390	40.520	45.280
$k = \omega C_r / V_{flight}^*$	1.0000	1.0000	1.0000	1.0000	1.0000
$J = \pi V_{flight}^* / [\omega h_o]$	6.2832	3.1416	2.0944	1.5708	1.2566

Table 6.2: Results of changing the heave amplitude.  $\alpha_{instant,max}$  is the maximum instantaneous angle of attack which occurs at the equilibrium position of the oscillation at a phase angle equal to  $90^\circ$ .

Increasing foil area will raise total thrust. In addition, increasing the heave amplitude will have an equivalent effect. In both cases, however, the dimensions of the foil and the heave amplitude usually have to be constrained by the geometry conditions where an oscillating propulsor is installed. The reason for a higher heave amplitude resulting in a higher thrust is that when the instantaneous velocity angle  $\alpha_o$  increases, the instantaneous angle of attack  $\alpha_{instant}$  also increases. A larger instantaneous angle of attack will usually produce a higher lift and thrust before separation occurs, but it will not produce a higher efficiency at all times; the pitching moment plays an important role in determining efficiency (see equation 3.59).

Changing the heave amplitude will also alter other parameters. For clarity, values are tabulated in table 6.2. It is noted that the small amplitude feathering parameter  $\theta$  decreased linearly with the decrease in the heave amplitude. However, the large amplitude feathering parameter  $\Theta$  decreased non-linearly due to the relationship being a reverse tangent function.

It can be seen that to obtain a larger thrust, the maximum instantaneous angle of attack needs to be increased. A too large angle of attack will produce a boundary layer separation or stall. When the oscillating frequency  $\omega$  and the swim velocity  $V_{flight}$  is fixed, increasing the pitch angle  $\alpha_o$  and increasing the heave amplitude  $h_o$  may keep the instantaneous angle of attack unchanged.

The advance ratio,  $J$ , defined by Bose and Lien (1989) is also included in the table.

This advance ratio, as a base of comparison, is better than reduced frequency for a tapered foil if the reference length is not taken as the average of all local chords. For a flexible foil with a spanwise flexibility, as the heave amplitude is not uniform across the span, the basis of comparison, instead of using the advance ratio  $J$  and feathering parameter  $\Theta$ , needs to be determined.

## 6-C Effect of apparent pitch amplitude on the efficiency and thrust

The apparent pitch amplitude was so named because, for an oscillating foil with a chordwise flexibility, the real maximum instantaneous pitch angle is no longer the same as that for a rigid oscillating foil. Therefore, the effective pitch amplitude had to be determined and used in calculations for flexible foils in Chapter 7. However, for rigid foils, this amplitude remains the same.

$\alpha_o$	0.1000	0.2000	0.4000	0.6000	0.8000
$\theta = \alpha_o V_{flight}^* / [\omega h_o]$	0.1000	0.2000	0.4000	0.6000	0.8000
$\Theta = \alpha_o / \tan^{-1}[\omega h_o / V_{flight}^*]$	0.1273	0.2547	0.5093	0.7639	1.0186
$\alpha_{instant,max}$	39.270	27.810	22.080	10.620	-0.840
$k = \omega C_r / V_{flight}^*$	1.0000	1.0000	1.0000	1.0000	1.0000
$J = \pi V_{flight}^* / [\omega h_o]$	3.1416	3.1416	3.1416	3.1416	3.1416

Table 6.3: Results of changing the apparent pitch amplitude.  $\alpha_{instant,max}$  is the maximum instantaneous angle of attack which occurs at the equilibrium position of the oscillation at a phase angle equal to  $90^\circ$ .

Table 6.3 tabulates the changes of small and large amplitude feathering parameters  $\theta$  and  $\Theta$ , reduced frequency  $k$  and the advance ratio  $J$ . It can be seen that at  $\theta = 0.8$ ,  $\Theta$  is already greater than one, in which case, a negative thrust is expected when a the large amplitude motion of the foil is considered.

The maximum allowable pitch amplitude was taken as  $0.8$  rad, i.e.,  $-45.84^\circ$ . Figure 6.3 shows that the oscillating foil no longer produced a positive thrust because the feathering parameter  $\Theta$  was too large ( $\Theta = 1.0186$  at  $\alpha_o = 0.8$  rad); consequently, the instantaneous angle of attack was less than zero.

In fact, at about  $\alpha_o = 0.8$  rad  $\simeq 45.84^\circ$ , the value of the thrust coefficient was about zero (see figure 6.3) because the angle of attack is close to zero or the large amplitude feathering parameter  $\Theta$  is about 1.0. This figure also tells us that there is an almost linear relation between the pitch amplitude and the thrust, perhaps due

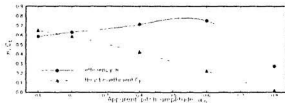


Figure 6.3: Effect of the apparent pitch amplitude  $\alpha_n$  on the propulsive efficiency  $\eta$  and the thrust coefficient  $C_T$  for a rigid oscillating foil with an aspect ratio of 8.

to the linear relation between the lift and the instantaneous angle of attack; i.e., the larger the  $\alpha_n$ , the smaller the  $\alpha_{instant}$ , and, hence, the smaller the lift and thrust. This trend, however, reverses the effect of heave on the thrust as shown in figure 6.2.

Results in figure 6.3 were obtained at an initial angle of attack of zero. Different initial angles of attack were also tested and there was no difference seen except that the oscillatory values of instantaneous lift and thrust shifted a phase angle. This will be discussed later.

The propulsive efficiency, however, follows a non-linear manner with different pitch amplitudes. This non-linear behaviour is different from case to case and reveals that, in oscillating propeller design, the maximum efficiency has to be evaluated for a particular oscillating foil with particular motion and geometry parameters. It can be seen that at a pitch angle  $\alpha_n = 0.6$  rad, i.e., at the maximum instantaneous angle of attack  $\alpha_{instant,max}$  about  $10^\circ$ , the maximum efficiency  $\eta$  was obtained. A too small angle of attack did not produce enough thrust and a too big angle of attack required too much pitching moment and hence they both resulted in a low efficiency.

As mentioned in verification of the results from an oscillating foil, efficiency drops to zero when the reduced frequency approaches zero. Reduction of pitch amplitude  $\alpha_n$ , when the reduced frequency  $k = \omega C_r / V_{flight}$  is fixed, is equivalent to decreasing the reduced frequency when the feathering parameter

$$\Theta = \alpha / \tan^{-1}[\omega h_n / V_{flight}]$$

is fixed. In other words, for a constant  $k$  (hence, a constant  $\omega$ ) decreasing the pitch

amplitude  $\alpha_o$  will decrease the large amplitude feathering parameter  $\Theta$ ; to keep  $\Theta$  constant, when decreasing the pitch amplitude  $\alpha_o$ , the oscillating frequency  $\omega$  has to be decreased (equivalent to having the same angle of attack). At a very small  $\omega$  and  $\alpha_o$ , the instantaneous angle of attack is very small too; a large portion of thrust will be cancelled by the pressure difference opposite to the motion of the foil (a calculated drag in the panel method) because the total amount of thrust produced is very small. Therefore, the efficiency drops dramatically at  $\alpha_o$  approaching to zero.

Again, at a larger pitch amplitude and hence a lower instantaneous angle of attack  $\alpha_{instant}$ , little thrust was produced, thus, the efficiency did not increase with the pitch amplitude. This effect is also equivalent to increasing the reduced frequency (in most cases increasing the angular speed) when the pitch amplitude is fixed.

## 6-D Effect of pitching axis position factor on the efficiency and thrust

Extensive study on the pitching axis position factor on the efficiency and thrust has been done previously. Examples include the calculations for a 2-D oscillating foil using small amplitude theory in Lighthill (1970) and the observation for a 3-D oscillating foil with a small amplitude assumption in Liu (1991). Here, results are presented for an oscillating foil of finite thickness based on a large amplitude theory by the present panel method (see figure 6.4).

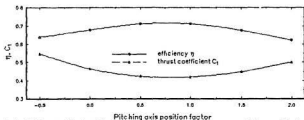


Figure 6.4: Effect of pitching axis factor on the propulsive efficiency  $\eta$  and the thrust coefficient  $C_t$  for a rigid oscillating foil with an aspect ratio of 8.

In the calculation, as only the pitching axis position changed, all the oscillating parameters were not altered. Therefore, throughout the range, the feathering parameter was  $\Theta = 0.5093$ , reduced frequency was  $k = 1.0$  and advanced ratio was  $J = \pi$ .

Compared with the study by Lighthill (1970), there is no difference in trends for the efficiency and thrust versus the pitching axis position. It can be seen from figure 6.4, that the best efficiency was at about  $x_{pitch}^* = 0.75 \sim 1.0$ , where the minimum thrust is expected. An effective way to increase the thrust is to increase either the heave amplitude (to increase the thrust coefficient) or the wing area (to increase the total thrust). The optimum pitching axis location can be set at  $x_{pitch}^* = 1.0$ , if the required thrust can be produced under the limitation of the heave amplitude and the wing area.

## 6-E Effect of phase angle on the efficiency and thrust

Results of phase angle effect are shown in figure 6.5. Unlike the effect due to the heave change, here, both efficiency and thrust had a non-linear relationship with the phase angle. This agrees with conclusions in previous studies, in a 2-D theory by Lighthill (1970), and in a 3-D lifting surface theory with a small amplitude assumption (Lan 1979 and Liu 1991).

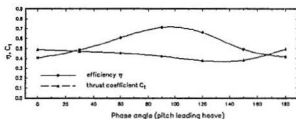


Figure 6.5: Effect of phase angle on the propulsive efficiency  $\eta$  and the thrust coefficient  $C_t$  for a rigid oscillating foil with an aspect ratio of 8. Phase angle was taken as pitch leading heave.

It can be clearly seen from the figure, for this particular foil geometry with particular motion parameters, that the efficiency  $\eta$  reached a maximum at the phase angle  $\Phi_{\text{phase}} = 90^\circ \sim 100^\circ$ ; this maximum representing an increase of about 80% over that in the range from  $0^\circ$  to  $90^\circ$ . The thrust coefficient  $C_t$ , however, had about a 30% variation in this range of the phase angle.

For experimental study and oscillating foil design, taking the phase angle around  $90^\circ$  seems to be a good choice if, again, the amount of thrust meets the requirement. In a case where a large thrust value is required, and where changing other parameters does not work or there are constraints on the change of other parameters such as the area of the wing, the phase angle has to be taken close to  $180^\circ$  or zero (they coincide with each other) to yield the maximum possible thrust.

The phase angle has an effect equivalent to the initial angle of attack. Therefore, for all computations, the initial angle of attack was taken as zero, with a phase angle of  $90^\circ$ .

## 6-F Effect of sectional thickness on the efficiency and thrust

In the computation, sectional offsets were taken according to a NACA 0012 four-digit series designation (Abbott and von Doenhoff 1949). Results obtained for the same rectangular foil, with sectional thickness ratios ranging from 6% to 24%, are presented in figure 6.6.

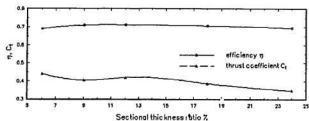


Figure 6.6: Effect of sectional thickness on the propulsive efficiency  $\eta$  and the thrust coefficient  $C_t$  for a rigid oscillating foil with an aspect ratio of 8.

The propulsive efficiency  $\eta$  had a maximum value at a thickness ratio of 12%. Throughout the thickness ratio range, changes in the value of  $\eta$  were rather small. However, the thrust coefficient  $C_t$ , reached large values for 6% thickness foil and 12% foil.

For foils with section thinner than 9% of the chord length, decreasing the thickness increased the thrust. This probably is the effect of the leading edge suction on the pressure distribution because of the sharp leading edge or the small L.E. radius. As can be seen in Chapter 5 (page 96, predicted thrust from the lifting surface theory was much higher than that from the present method. Here, the thickness effect had played an important role. In lifting surface theory, the thickness of a foil is zero; hence a large amount of leading edge suction was added to the total thrust.

A thickness ratio less than 6% seems not to be economically feasible for engineering applications, at least at present, in oscillating foil design, because of the strength of

available materials. In fact, for such a thin wing the efficiency might have a steep drop when the foil is made flexible (see next chapter) due to the large chordwise and spanwise deflexion. Therefore, reducing the thickness is not a good method to increase thrust.

For foils with a sectional thickness higher than 15% of chord, the larger the thickness the smaller the thrust. This implies that a thicker foil section has lower hydrodynamic efficiency. The optimum thickness for an oscillating foil, if structural problems are not a concern, would be around 12% of the chord.

## 6-G Efficiency and thrust from a lunate planform

Study of the propulsion from the lunate tail of marine animals has been conducted for about a half century. Numerous publications are available but most of them are either based on 2-D theories (some may include a 3-D correction) or lifting surface theory in which foil thickness has been neglected; or small amplitude motion, from which results obtained at large amplitude of heave and pitch are questionable.

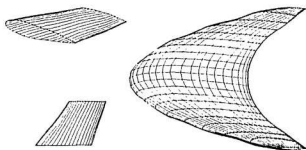


Figure 6.7: 3-D geometry of a man-made lunate planform with an aspect ratio of 8. This 3-D surface panel is illustrated by the perspective view.

Based on the above arguments, predictions were made for a man-made lunate planform to observe the differences between methods. This man-made lunate wing was taken from Chopra and Kambe's (1977) work: the B2 planform.

In their work, the offsets of the foil were calculated by

$$c = C_r \left\{ 1 - \left( \frac{y}{s} \right)^2 \right\} + C_{tip} \left( \frac{y}{s} \right)^2 \quad (6.4)$$

for the local chord length and

$$x_l = K \left( \frac{y}{s} \right)^2 \quad (6.5)$$

for the leading edge offsets. When  $K$  is taken as  $\frac{5}{4}$ ,  $s$  as 3,  $C_r = 1.0$  and  $C_{tip} = 0.25$  (the tip chord length), the foil has an aspect ratio of  $A_l = 6s(2C_r + C_{tip}) = 8$  and

an area of  $S = \frac{2}{3}s(2C_r + C_{tip}) = 4.5$ . Input data were taken for nine stations and recorded on the input worksheet; then they were curve fitted by a spline function in the JobContr.FOR program. The sectional offsets were taken as a NACA 0012 designation (with 41 stations) and they were interpolated by the same program. The right graph in figure 6.7 shows a perspective view of the foil with cosine and uniform spacing in chordwise and spanwise directions respectively. The upper left graph shows a 3-D view of the right-most (starboard) tip section. The lower left graph shows the top view of this tip section.

Calculations were done based on the following geometry and motion parameters:

- heave amplitude  $h_{heave} = 1.0$  m; hence, the factor  $h_o = h_{heave}/C_r = 1.0$ ;
- forward swim velocity  $V_{flight} = 1.0$  m/sec; then, the velocity factor  $V_{flight}^* = 1.0$ /sec;
- pitching axis  $x_{pitch}^* = x_{pitch}/C_r = 1.0$ ;
- small amplitude feathering parameter  $\theta = 0.0, 0.4$ ;
- large amplitude feathering parameter  $\Theta = 0.0, 0.5093$ ;
- angular velocity  $\omega = 0.2 \sim 1.8$  to obtain  $k = 0.2 \sim 1.8$ ;
- and pitching amplitude  $\alpha_o = 0.08 \sim 0.72$  rad.

It is noted that the value of  $\Theta$  corresponding to  $\theta = 0.4$  is not uniform for each curve by the present method because of the non-linear large amplitude relationship. Therefore, at  $\omega = 0.2, 0.6, 1.0, 1.4$  and  $1.8$ , they are 0.4093, 0.4441, 0.5093, 0.5892, 0.6769, respectively.

For this man-made lunate foil, two comparisons were done and are presented as follows. They are: a) the present method versus previous ones. The present method takes the large amplitudes and the sectional thickness into account. The computations were done in the time domain. The previous methods are based on small amplitude lifting surface theory (zero sectional thickness); and b) propulsive efficiency and thrust

from a rectangular oscillating wing versus those from the man-made lunate planform predicted by the present method.

### 6-G-1 Present method versus lifting surface theory for a man-made lunate tail

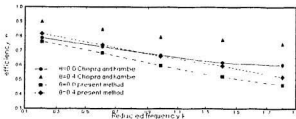


Figure 6.8: Efficiency  $\eta$  of a man-made lunate planform with an aspect ratio of 8.

Figure 6.8 shows the propulsive efficiency predicted by a small amplitude lifting surface theory (Chopra and Kambe 1977) and by present method. In calculation, this lunate tail propulsor was set to have a NACA 0012 section. Similar to the comparison for the rectangular oscillating foil in Chapter 5, the present method gives a lower efficiency prediction, especially at a large frequency, because of the practical large amplitude consideration.

In addition to the large difference in the feathering parameter, which makes the comparison difficult at higher amplitudes of oscillation, for a small amplitude feathering parameter  $\theta = 0.4$ , when the reduced frequency is  $k = 1.8$ , the pitch amplitude  $\alpha_0$  is  $0.72 \text{ rad}$ . The error for pitch amplitude estimation itself from small amplitude assumption is about  $\epsilon = 50\%$ . There is also about the same amount of error in heave amplitude. Therefore, the discrepancy at larger heave and pitch amplitudes is significant. For a small feathering parameter, for example,  $\theta = 0.0$ , only the error of heave amplitude exists; hence, the difference in efficiency is smaller.

In figure 6.9, the difference in thrust is substantial; lifting surface theory predicted a much larger thrust. The slope of the thrust curve obtained by the lifting surface theory at higher pitch amplitude (the same as a higher reduced frequency  $k$  at a fixed

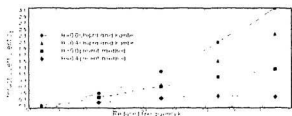


Figure 6.9: Thrust of a man-made lunate planform with an aspect ratio of 8.

feathering parameter  $\theta$ ), is steep. In lifting surface theory, the steepness is due to the linear effect of the lift coefficient  $C_L$  slope and the increasing thrust portion (the x-component of the normal force), when  $\alpha$  increases. Such a large difference in the thrust coefficient is not surprising, because the angle of attack of the small amplitude theory is almost twice as large as the large amplitude theory one.

### 6-G-2 Effect of the man-made lunate planform on efficiency and thrust

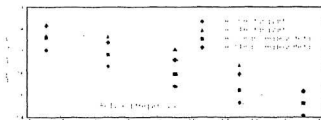


Figure 6.10: Efficiency  $\eta$  of a man-made lunate planform and a rectangular oscillating foil.

To observe the effect of a lunate tail on  $\eta$  and  $C_T$ , results from a rectangular oscillating propulsor were obtained. This wing had a span of 6 m and a chord of 0.75 m. The forward swimming velocity  $V_{flight}$  is set as 0.75 m/sec in order to have all the

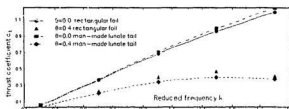


Figure 6.11: Thrust coefficient  $C_t$  of a man-made lunate planform and a rectangular oscillating foil.

same motion parameters.

Figures 6.10 and 6.11 show that the man-made lunate planform had a significant efficiency and thrust increase over those from the rectangular planform, at a very small feathering parameter ( $\Theta = \theta = 0.0$ ), throughout all the reduced frequency range. As was mentioned before, at  $\Theta = 0.0$ , the instantaneous angle of attack of the foil reaches a maximum. In this case, the foil was under a heavy load condition; the lunate tail had a better performance. At a medium feathering parameter, the instantaneous angle of attack is smaller (so that the thrust is smaller), the higher pressure drag became dominant over the thrust, and the required pitch moment portion of the input power increased (hence the efficiency decreased). This made the efficiency and thrust less than those from a rectangular foil.

The observation above indicates that a) the propulsive performance of different swept planforms predicted by evaluating them only in steady flow (for example in van Dam 1986) is not adequate; b) as the lifting surface theory does not consider the pressure drag and most previous 3-D methods were based on a small amplitude assumption, evaluations related to the effect of the swept planforms on the swim efficiency using these methods may have a questionable accuracy.

## 6-H Efficiency and thrust from a fin whale's flukes

Results were also obtained for a naturally occurring planform: a fin whale's flukes. The measurements of the flukes were taken from the work by Bose and Lien (1989). The thickness of the flukes' section is 19.6% of the chord. Figure 6.12 shows such a planform. In the figure, the lower right graph shows the top view and the upper left one is a perspective view. The flukes have a span of 3 meters and an aspect ratio of 6.1. Their root chord is 0.87 m. Comparison between the present method and lifting surface theory, and also the effect of the lunate tail on  $\eta$  and  $C_t$ , will be discussed below separately.

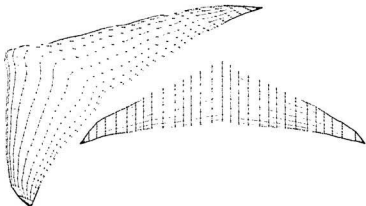


Figure 6.12: Three dimensional geometry of a fin whale's flukes. The left graph has a perspective view so that the tip of the left fluke looks rather wide.

### 6-H-1 Present method versus lifting surface theory for the flukes of a fin whale

To compare the results from the lifting surface theory with those by present method, the following motion parameters were used:

- $V_{flight}^* = V_{flight}/C_r = (0.87 \text{ m/sec})/(0.87 \text{ m}) = 1.0;$

- $h_o = h_{kave}/C_r = 0.87 \text{ m}/0.87 \text{ m} = 1.0$ ;
- $\alpha_o = 20^\circ \simeq 0.3491 \text{ rad}$ ;
- $\Phi_{phasc} = 90^\circ = \pi/2 \text{ rad}$ ;
- and  $x_{pitch}^* = x_{pitch}/C_r = 1.0$ .

Based on the above motion parameters, the values of  $J$ , along with the other variables, are listed in table 6.4.

$J = \frac{rV_{flight}}{\omega h_o}$	0.5000	3.5000	6.0000	7.0000	8.0000	9.0000
$\theta = \frac{J\alpha_o}{\pi}$	0.0556	0.3889	0.6667	0.7778	0.8889	1.0000
$\Theta = \alpha_o / \tan^{-1} \left[ \frac{\omega h_o}{V_{flight}} \right]$	0.2471	0.4773	0.7238	0.8276	0.9330	1.0395
$k = \frac{\omega C_r}{V_{flight}}$	6.2832	0.8976	0.5236	0.4488	0.3927	0.3491
$\omega$	6.2832	0.8976	0.5236	0.4488	0.3927	0.3491

Table 6.4: Advance ratio  $J$  versus other motion parameters for a fin whale's flukes.

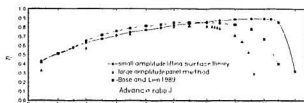


Figure 6.13: Propulsive efficiency of rigid fin whale's flukes: present method versus lifting surface theory with small amplitude assumption and a 2-D strip theory with finite span and skin drag corrections.

It can be seen from figure 6.13 that the prediction by the present method on efficiency has a good agreement among others at a medium advance ratio  $J$ . When  $J$  was very small, the foil oscillated at a large frequency  $\omega$  ( $\omega$  is  $2\pi$  at  $J = 0.5$ ) so that it had a big instantaneous angle of attack. The maximum thrust will always occur at the largest instantaneous angle of attack. A too large instantaneous angle of attack

then yielded a smaller efficiency than other methods. At a higher advance ratio thus a small instantaneous angle of attack, as total thrust is small, calculated pressure drag by panel method together with the skin friction drag cancelled a large portion of the thrust and, hence, the efficiency dropped earlier than the efficiency curves obtained by the 3-D lifting surface theory (Liu and Bose 1993) and the 2-D strip theory with a 3-D correction (Bose and Lien 1989). As the skin friction drag estimation was taken in the 2D strip theory with a 3-D correction, the efficiency curve by Bose and Lien (1989) dropped earlier than that predicted by using the 3-D lifting surface theory. Predicted by the present method, the efficiency dropped quickly after  $J = 6$  and this is mainly due to the drop in the maximum instantaneous angle of attack.

This also indicates that, when the amplitude of pitch and heave is carefully controlled, small amplitude lifting surface theory gives an acceptable prediction. This prediction, however, is limited to a small range of oscillating parameters.

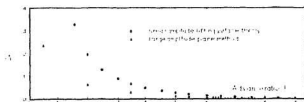


Figure 6.14: Thrust coefficient  $C_t$  of rigid fin whale's flukes: present method versus lifting surface theory with small amplitude assumption.

As it was observed before, there is a large discrepancy between the thrust predictions determined by the two methods, especially at higher value pitch and heave amplitudes, feathering parameter, oscillating frequency and reduced frequency. A large difference in the thrust determined by the two methods can also be seen in figure 6.14 for the fin whale's flukes due to a remarkable difference in the angle of attack at a low advance ratio  $J$  (equivalent to a small value of the large amplitude feathering parameter  $\theta$  at which value, the difference in the angle of attack is substantially large).

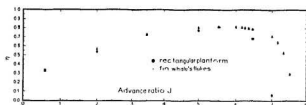


Figure 6.15: Efficiency  $\eta$  of the flukes of a fin whale and a rectangular oscillating foil.

### 6-H-2 Effect of a natural lunate tail on efficiency and thrust

Computation was also done for a rectangular oscillating propulsor with an aspect ratio of 6.1 to compare with the flukes of the fin whale. The span of the foil was 3.0 m and chord length was 0.4918 m. To have the same basis of comparison,  $V_{flight}$  was taken as 0.4918 m/sec so that all other motion parameters are the same as those for the flukes. The sectional thickness distribution was also set the same as that of the flukes.

Predicted propulsive efficiency and thrust for a rectangular oscillating planform are presented in figures 6.15 and 6.16. When the wings are rigid, there is not much difference in either efficiency or thrust between these two different planforms. A large drop in efficiency for the rectangular planform, however, occurs after the advance

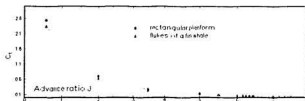


Figure 6.16: Thrust coefficient of the flukes of fin whale and a rectangular oscillating foil.

ratio reaches about 6. At a large advance ratio, the instantaneous angle of the axis kinematic velocity  $\alpha_v$  is small and, hence, the instantaneous angle of attack is small (this is true in most normal cases, in which the feathering parameter has to be less than 1.0). This indicates that, when the oscillating foil is under a light load, the fin whale flukes obtain a higher efficiency and the flukes' working range in terms of the advance ratio  $J$  is also wider. It can also be seen that, at a heavier load where  $J$  is small, the fin whale flukes also had a slightly bit better performance.

It can be seen that the rectangular foil under a heavy load condition will produce more thrust than the fin whale flukes; and the smaller the advance ratio, the greater the thrust produced by the rectangular foil.

The above comparisons for both the man-made lunate planform and the naturally occurred fin whale flukes suggest that for a rigid oscillating propulsor, lunate tails have a slightly bigger working range. A rectangular foil, however, can produce almost the same amount of thrust and efficiency.

## 6-I Effect of skin friction on efficiency and thrust

To have a common basis for a comparison of results from the small amplitude theory, results presented below used the small amplitude feathering parameter for two groups, though they were obtained by the large amplitude assumption. Therefore, the large amplitude feathering parameter is not uniform for each curve corresponding to  $\theta = 0.4$  in each plot.

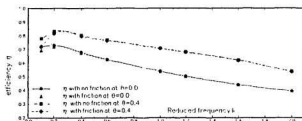


Figure 6.17: Effect of skin friction  $C_f$  on efficiency  $\eta$  of a rectangular oscillating foil with an aspect ratio of 8.

Figure 6.17 shows the effect of skin friction on the efficiency for a rectangular foil with an aspect ratio of 8. At a low reduced frequency, where the generated thrust was small, the skin friction and the calculated pressure drag (they had about the same order) cancelled a major portion of the thrust. Therefore, the efficiency there

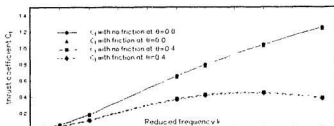


Figure 6.18: Effect of skin friction  $C_f$  on the thrust coefficient  $C_t$  of a rectangular oscillating foil with an aspect ratio of 8.

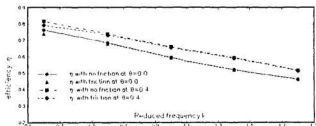


Figure 6.19: Effect of skin friction on efficiency of a lunate oscillating foil with an aspect ratio of 8.

was small. At a higher reduced frequency, the skin friction relative to the generated thrust is negligible. Therefore, there is no reduction of efficiency. This is also similar to the curves for the man-made lunate *B2* planform; the only difference is that the skin friction affected the efficiency in the lower range of reduced frequency (see figure 6.19).

As can be seen in figures 6.18 and 6.20, skin friction had little effect on the thrust coefficient for the rectangular foil and the lunate tail *B2* wing; the average value of  $C_f$  was about 0.085 ~ 0.095. The skin friction effect had no change with a different feathering parameter  $\theta$  or  $\Theta$ . As mentioned before, the implementation of the skin friction formulation was mainly to establish a basis for a qualitative comparison of flow pattern between a rigid and a flexible foil. This will be discussed in the next chapter.

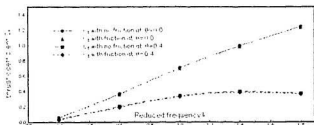


Figure 6.20: Effect of skin friction on thrust of a lunate oscillating foil with an aspect ratio of 8.

## Chapter 7

# Results and discussion: flexible oscillating foils

This large amplitude, time domain, flexible 3-D geometry panel method, has been used to simulate an oscillating rigid, non-zero thickness foil with an arbitrary planform. In this chapter, simulations move a further step toward reality: computing the performance of an oscillating propulsor with both chordwise and spanwise deflexion.

For a foil with given geometry, motion parameters, and modulus of elasticity, the propulsive performance could be evaluated by iteration, which couples the hydrodynamical forces, their equilibrium and structural rigidity at each time step. This kind of method yields the efficiency and thrust and, at the same time, gives the passive deflexion shapes and magnitudes. This passive approach may be advantageous in designing a particular man-made oscillating propulsor with given planform shape, thickness distribution and variation of rigidity (material, spanwise and chordwise sectional moment of inertia). However, the passive calculation may lose a generality: fish tails and flukes of whales and dolphins and, especially the flapping wings of birds, may have certain muscle control on their propulsors, so that either the chordwise and/or the spanwise deflexion might be controlled actively. In addition, for certain advanced man-made oscillating airfoils or man-made swimming fish, optimization of

the positive deflexion control needs also to be realized, to give a good and controllable propulsive performance. Therefore, deflexions in both the chordwise and the spanwise directions were pre-determined in terms of shape functions and amplitudes in this study.

This chapter will first discuss the selection of a number of chordwise and spanwise deflexion equations; secondly, it will examine the effect of a variety of flexibility parameters on the propulsive performance; it will then compare the results from the present method with that from a 2-D panel method in which a half chord elastic rectangular foil was tested (Yamaguchi 1992); finally, the propulsive performance of the fin whale flukes will be examined.

## 7-A Selection of chordwise and spanwise deflexion equations

Selection of equations involved both the chordwise and spanwise directions and they are discussed separately below.

### 7-A-1 Deflexion equations for chordwise flexibility

For a general oscillating flexible foil, as the distribution of the moment of inertia of the section parallel to the span and the variation of the chordwise pressure distribution are not predetermined, the shape function is difficult to obtain. In this study, in addition to a cubic function assumption (Bose 1992),  $y = 8\delta(x - 0.5)^3$ , in a 2-D analysis, five other equations were added to make a total of six. For a 3-D foil, the chordwise deflexion shape for each section was assumed to be the same across the span, though the thickness distribution of each section may be different. Equation (7.1) is the shape function in a general form. The order  $\epsilon$  of the shape functions in equation (7.1) ranges from 1.5 to 4. These six equations in a general form, after normalization, are

$$z = \delta_c(2x - 1)^\epsilon \sin(\omega t + \Phi_c), \quad (7.1)$$

where  $\delta_c$  is the chordwise deflection amplitude ( $\delta_c = \delta_{co}C_{local}$ ), a product of the chordwise deflection factor  $\delta_{co}$  (the input data for the maximum chordwise deflection referring to the chord length) and the local chord length;  $\epsilon$  is taken as  $\epsilon = 1.5, 2, 2.5, 3, 3.5, 4$  and  $\Phi_c$  is the phase angle of the deflection relative to the pitch. When  $\epsilon$  is taken as 3, the chordwise deflection equation is then reduced to that of Bose 1992. The value of  $\Phi_c$  in a normal case (for a passive deflection) is negative.

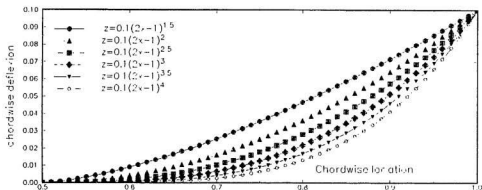


Figure 7.1: Shapes of chordwise deflexions determined by six equations.

The shapes of these six functions are plotted in figure 7.1. In the figure, the maximum deflection was set as 10% of the local chord length.

Several assumptions are listed as follows:

- Deflection starts at half local chord.
- Maximum deflection is at the trailing edge and its magnitude is determined by the local chord length and the deflection factor  $\delta_{co}$ .

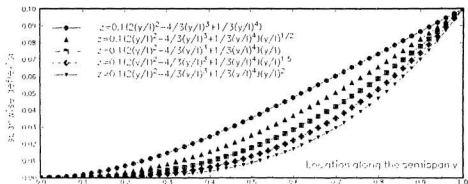


Figure 7.2: Shapes of spanwise deflexions determined by five equations.

- One shape function governs all sections so that all sectional shapes of deflexions are the same, though the thickness and/or the shape of the foil section may vary. In other words, there is no twist or torsional deflexion along the span.

Based on the above assumptions, several corresponding numerical procedures were performed: a) Each panel on the flexible part of the foil has a relative velocity. This relative velocity was calculated by differentiating eq. (7.1) with respect to time  $t$ . b) This relative velocity has to be added to the total velocity after a transformation from the body frame to the global frame; and c) As the shape of the foil varies with each time step, the influence doublet and source coefficient matrices have to be re-evaluated at each time step.

### 7-A-2 Deflexion equations for spanwise flexibility

Five spanwise deflexion equations were formed by using a cantilever beam deflexion function, and they are shown in figure 7.2.

The standard deflexion formula for a uniform cantilever beam with a uniformly distributed load is

$$z = \frac{-W}{24EI} [6ly^2 - 4y^3 + y^4/l]. \quad (7.2)$$

As the dimension of  $l$ ,  $E$  and  $W$  are:

$$l \rightarrow l^4, \quad E \rightarrow N/l^2 \text{ and } W \rightarrow N,$$

the unit of the fraction outside the brackets of equation (7.2) is  $l^{-2}$ . Therefore, equation (7.2) can be rewritten for a time dependent oscillation, in a form of

$$z = \delta_s [2(\frac{y}{l})^2 \mp \frac{4}{3}(\frac{y}{l})^3 + \frac{1}{3}(\frac{y}{l})^4] \frac{y}{l} \epsilon \sin(\omega t + \Phi_s). \quad (7.3)$$

In equation (7.3),  $\delta_s$  is the maximum deflexion,  $\delta_s = \delta_{so}l$ , a product of spanwise deflexion factor  $\delta_{so}$  and half span length  $l$ .  $\Phi_s$  is the spanwise deflexion phase angle relative to pitch.  $\epsilon$  is taken as 0, 0.5, 1, 1.5 and 2.

The second term in the brackets of equation (7.3) has to be negative for the left half span and positive for the right half span to have a symmetrical deflexion. The maximum deflexion occurs at the span tip at  $y = l$ , and zero deflexion occurs at the root chord at  $y = 0$ .

Though there are altogether five spanwise deflexion equations available in the OSFBEM.FOR, only three of them will be discussed here; as it will be seen later, the shape function of the spanwise deflexion has a negligible effect on the propulsive performance compared with the amplitude of the spanwise deflexion.

### 7-A-3 Determination of instantaneous effective angle of attack

As thrust and efficiency are dependant on the instantaneous angle of attack  $\alpha_{instant,max}$ , this instantaneous angle of attack is useful in explaining the relations between forces and deflexion.  $\alpha_{instant,max}$  is also important for boundary layer separation control.

Instantaneous angle of attack is the difference between the instantaneous pitch angle  $\alpha$  and the instantaneous angle of the foil's kinematic velocity  $\alpha_v$ , i.e.,  $\alpha_{instant} =$

$\alpha_v - \alpha$ . In an oscillation with pure chordwise flexibility, the instantaneous pitch angle changes but the  $\alpha_v = \tan^{-1} \frac{w^h}{V_{flighth}}$  remains constant.

In 2-D foil theory the effective angle of attack, when a wing section is deformed, can be determined by finding the angle of zero lift. A numerical implementation was done in the present method to find the angle of zero lift by using Glauert's expression following Pankhurst (1944). In this method, the angle of zero lift of each section was obtained first; then the angle of zero lift of the whole foil was found by using

$$\alpha_{zero} = \frac{\sum_{i=1}^I (c_{local})_i (\alpha_o)_i}{\sum_{i=1}^I (c_{local})_i} \quad (7.4)$$

For a symmetrical, rigid foil, the angle of zero lift  $\alpha_{zero}$  is zero. However, the chordwise deflexion made the symmetrical section become a cambered one. Therefore, the angle of zero lift  $\alpha_{zero}$  was no longer zero. The instantaneous pitch angle  $\alpha$  increased at a value of  $\alpha_{zero}$ <sup>1</sup>. The lift and the thrust were then determined inherently by the panel method.

For a non-twisted foil, each section has the same angle of zero lift; so does the whole foil. The feathering parameter, as the pitch amplitude  $\alpha_o$  increases due to the flexibility, increases because of eq. (6.1)

$$\Theta = \frac{\alpha_o}{\tan^{-1} \frac{w^h}{V_{flighth}}}$$

Increasing  $\Theta$  will produce a higher efficiency and a smaller thrust; therefore, when the chordwise amplitude increased, the efficiency increased and the thrust dropped. However, when the chordwise deflexion became sufficiently large so that  $\Theta$  was greater than 1.0, the instantaneous angle of attack changed its sign; then, a negative thrust is generated. Therefore, a large chordwise amplitude deflexion of a foil may mix both positive and negative thrust; hence, a lower efficiency and thrust may be obtained; or, when the instantaneous angle of attack is close to zero, a small amount of drag will cancel the large portion of generated thrust; this results in a lower value of the efficiency  $\eta$  and the thrust coefficient  $C_t$ .

<sup>1</sup>In this case, the instantaneous pitch angle is  $\alpha = \alpha_{rigid} - \alpha_{zero}$

### 7-A-4 Graphical representation of fin whale flukes in motion

In order to have an idea of the instantaneous deflexion shape and the shed wake patterns behind the fin whale's flukes, graphics for a combination of 19 chordwise and spanwise deflexion functions governing the flexible flukes are presented in Appendix B.

Calculations were also made to observe the propulsive performance for these 19 cases. In the computations, the following parameters were used:  $\delta_{co} = 0.1$ ;  $\delta_{so} = 0.1$ ;  $\Phi_c = -30^\circ$ ;  $\Phi_s = 90^\circ$  (small flap);  $h_o = h/C_r = 1.305/0.87 = 1.5$ ;  $\alpha_o = 20^\circ$ ;  $\Phi_{phase} = 90^\circ$ ;  $X_{pitch}^* = 1.0$ ;  $\omega = 0.2\pi$ ;  $k = 0.2\pi$ ;  $\Theta = 0.4619$  and  $\theta = 0.3704$ .

Table 7.1 tabulates some results from a series of calculations.

The results shown in table 7.1 show that:

- The higher the order of  $\epsilon$  in the chordwise deflexion, the higher the instantaneous pitch angle. This was obvious because the slope of the deflexion shape function close to the trailing edge increased when the value of  $\epsilon$  increased, and, hence, the value of the angle of zero lift of the camber section increased.
- A larger  $\epsilon$  in the chordwise deflexion equation increased the instantaneous pitch angle, and, hence, decreased the value of maximum angle of attack. In other words, the value of instantaneous pitch angle was closer to the velocity slope  $\frac{w}{V_{flight}}$  when  $\epsilon$  was increased. This is the reason why the overall feathering parameter was higher with the increase in  $\epsilon$ .
- Maximum efficiency was obtained by using chordwise deflexion equation #3 and spanwise deflexion equation #2.
- Too large a value of  $\epsilon$  in the case of the spanwise deflexion produced both small efficiency and thrust. The best thrust was obtained from the rigid foil, followed by the least flexible foil governed by C1S1. When  $\epsilon$  was small, the efficiency increased with an increase in the chordwise flexibility; however, when  $\epsilon$  was too large (greater than 4), efficiency decreased with an increase of the value in  $\epsilon$ .

Eqn.	$C_t$	$C_t w/C_f$	$\eta$	$\eta w/C_f$	$\alpha_{eff}$	$\alpha_v$	$\alpha_{max}$	$\Theta_{eff}$
C0S0	0.2600	0.2539	0.8098	0.7969	20.00	43.30	23.30	0.4619
C1S1	0.1473	0.1410	0.8394	0.8147	30.63	43.30	12.67	0.7074
C1S2	0.1431	0.1370	0.8402	0.8155	30.63	43.30	12.67	0.7074
C1S3	0.1402	0.1341	0.8404	0.8153	30.63	43.30	12.67	0.7074
C2S1	0.1310	0.1246	0.8430	0.8152	32.04	43.30	11.26	0.7400
C2S2	0.1269	0.1207	0.8439	0.8159	32.04	43.30	11.26	0.7400
C2S3	0.1239	0.1178	0.8442	0.8158	32.04	43.30	11.26	0.7400
C3S1	0.1174	0.1111	0.8441	0.8132	33.26	43.30	10.04	0.7681
C3S2	0.1133	0.1072	0.8451	0.8139	33.26	43.30	10.04	0.7681
C3S3	0.1104	0.1043	0.8455	0.8138	33.26	43.30	10.04	0.7681
C4S1	0.1056	0.0993	0.8426	0.8086	34.35	43.30	8.950	0.7933
C4S2	0.1016	0.0955	0.8437	0.8090	34.35	43.30	8.950	0.7933
C4S3	0.0987	0.0926	0.8441	0.8086	34.35	43.30	8.950	0.7933
C5S1	0.0950	0.0888	0.8386	0.8009	35.32	43.30	7.980	0.8157
C5S2	0.0911	0.0849	0.8396	0.8009	35.32	43.30	7.980	0.8157
C5S3	0.0882	0.0822	0.8399	0.8050	35.32	43.30	7.980	0.8157
C6S1	0.0883	0.0820	0.8310	0.7906	36.21	43.30	7.090	0.8363
C6S2	0.0884	0.0783	0.8318	0.7905	36.21	43.30	7.090	0.8363
C6S3	0.0816	0.0755	0.8320	0.7895	36.21	43.30	7.090	0.8363

Table 7.1: Comparison of nineteen combinations of deflexion equations for a fin whale's flukes. In the table, C0S0 means that there is no deflexion and C1S2 indicates that the chordwise shape function was equation number one and the spanwise shape function was equation number two.  $\eta$  and  $C_t$  are efficiency and thrust and "w/C<sub>f</sub>" means that the values were obtained after the reduction of the skin friction.  $\alpha_{eff}$  is the effective pitch angle due to the flexibility. This angle, however, is an overall value for the whole planform if the chordwise deflexion is not uniform and is both an overall and local value if the governing equation is the same for all the sections.  $\alpha_v$  is the kinematic velocity of the foil's pitching axis, and it is obtained by neglecting the non-uniform heave amplitude due to the spanwise deflexion. Strictly, each section has its own  $\alpha_v$  at each time for a foil with spanwise flexibility. The value of  $\alpha_{max}$  is the maximum instantaneous angle of attack and it was obtained by assuming the phase angle  $\Phi_{phase} = \pi/2$ .  $\Theta_{eff}$ , the effective large amplitude feathering parameter, was calculated based on  $\alpha_v$  and  $\alpha_{eff}$ . All the angular values above for each local section at each time step were obtained and recorded in the output file OSFBEM.LOG.

- The larger the maximum instantaneous angle of attack, the larger the thrust coefficient.
- The best efficiency ( $\eta = 0.845$ ) was obtained at the maximum instantaneous angle of attack of about  $10^\circ$ .

It was found that a combination of the heave amplitude factor  $h_o$ , and the phase angle of the spanwise deflexion phase angle  $\Phi_s$  had a strong effect on the selection of the spanwise deflexion amplitude to yield a positive thrust. Normally, a combination of a higher heave amplitude and a spanwise deflexion phase angle of about  $\Phi_s = 180^\circ$  (the active control of deflexion) along with a large spanwise deflexion amplitude  $\delta_s$  gave the best efficiency and thrust (see page 139). The selection of shape functions that governed the deflexion in both directions showed a much smaller effect than the amplitude of deflexion on the efficiency and thrust.

## 7-B Effect of the chordwise deflexion phase angle on efficiency and thrust

A graphical analysis of a flexible foil for the chordwise deflexion was done and it suggested that a phase angle between the start of the deflexion and the pitch is necessary for flexible foils. This is evidenced by the fact that a flexible foil needs time to adjust the bending equilibrium itself and, consequently, the maximum deflexion does not occur at the same instant as the bending moment reaches its maximum.

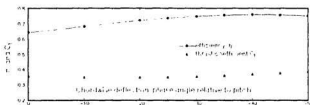


Figure 7.3: Effect of the chordwise deflexion phase angle  $\Phi_c$  on the efficiency  $\eta$  and the thrust coefficient  $C_t$  for a rectangular half elastic chord oscillating foil.

Figures B.23 through B.28 in Appendix B show the instantaneous chordwise deflexion and the wake pattern with different deflexion phase angles ranging from  $0^\circ$  to  $-50^\circ$ . The geometry and motion parameters of the oscillating foil shown are also listed in Appendix B.

As can be seen in figures B.23 through B.28, the trailing edge of the sixth foil position is higher than the maximum height (T.E. was taken as the location of the pitching axis). This trailing edge position gradually became lower than the extreme points. The wake patterns, however, do not appear much different from each other in the geometry shown.

A number of calculations were done to determine the effect of the chordwise phase angle on thrust and efficiency. Figure 7.3 shows that the maximum efficiency was obtained at  $\Phi_c = -40^\circ$ , with a thrust the same as it was at  $\Phi_c = 0^\circ$ . When  $\Phi_c$  is

greater than  $40^\circ$ , efficiency drops rapidly at about the same rate as the increase in thrust. As can be seen in figure B.25, the shape of the chordwise deflexion at the peak and the trough seems practical.

## 7-C Effect of the spanwise deflexion phase angle on efficiency and thrust

To test the effect of the phase angle of spanwise deflexion on the efficiency and thrust, performance of a fin whale's flukes was calculated, by using the following parameters:

- planform and section geometry were the same as those in Chapter 4-II;
- chordwise deflexion equation no. 0, no deflexion;
- spanwise deflexion equation no. 1 with amplitude of 0.1;
- oscillating frequency  $\omega = 0.2\pi$ ;
- phase angle  $\Phi_{phase} = 90^\circ$ ;
- pitch amplitude  $\alpha_o = 20^\circ$ ;
- pitching axis position at the T.E.  $x_{pitch}^* = 1.0$ ;
- flukes swimming speed  $V_{flight}^* = 1.0/sec$ ;
- heave amplitude of the root chord  $h_o = 1.0$ ;
- large amplitude feathering parameter based on the root chord  $\Theta = 0.6223$ ;
- the spanwise deflexion phase angle ranging from  $-180^\circ \sim 180^\circ$ .

It was noted that when a foil has a spanwise flexibility, the instantaneous heave velocity of each section varies across the span. This is due to the pitching axis being no longer a straight line; the height of the pitching axis is not uniform along the span. Therefore, the second term of input power of equation (3.58),  $L\dot{h}$ , has to be re-evaluated for each section instead of for the whole foil.

As the chordwise flexibility does not affect the pitching axis' kinematic velocity, the total relative velocity due to the flexibility cannot be taken into account for the efficiency. In the present method, the vertical velocity due to the spanwise deflexion

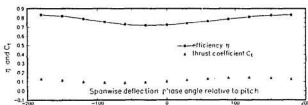


Figure 7.4: Effect of the spanwise deflection phase  $\Phi_s$  on the efficiency  $\eta$  and the thrust coefficient  $C_t$  for a fin whale's flukes.

at all the control points of all panels of each section at each time step were averaged for a mean vertical velocity of the section. As this mean velocity was evaluated based on the body frame coordinates, it had to be transformed to the inertia frame before it was subtracted from the root chord pitching axis' heave velocity.

If the velocity due to spanwise flexibility at each control point is  $v_{i,j}$ , where  $i$  is the  $i$ th number of chordwise panel and  $j$  is the  $j$ th number sections, the mean velocity of each section is then:

$$V_j = \sum_{i=1}^I v_{i,j}. \quad (7.5)$$

The term  $L\dot{h}$  in the input power for the whole foil at each time step is then

$$P_{input,A} = L\dot{h} = \sum_{j=1}^J (c_l * s)_j [-V_j + \dot{h}_{root}]. \quad (7.6)$$

A number of calculations were also done for different phase angles ranging from  $\Phi_s = -180^\circ$  to  $180^\circ$ . Figure 7.4 shows the effect of the spanwise deflection phase angle on  $\eta$  and  $C_t$ . Results show that when the spanwise deflection did not have a muscle control, i.e., the phase angle  $\Phi_s$  was about  $0^\circ \sim 30^\circ$ , the predicted efficiency was the minimum and the thrust was also at the bottom line. In this case, compared with the rigid foil, spanwise deflection produced both low thrust and small efficiency.

When the foil's spanwise deflexion is under an active control, especially at an angle of  $180^\circ$ , the efficiency and the thrust had a substantial increase.

The best efficiency of  $\eta = 0.8319$  was obtained at  $\Phi_s = \pm 180^\circ$  with a thrust coefficient of  $C_t = 0.1332$ ; and the best thrust coefficient of  $0.1482$  with a good  $\eta$  of  $0.8322$  occurred at  $\Phi_s = 120^\circ$ .

## 7-D Effect of the chordwise deflexion amplitude on efficiency and thrust

To observe the effect of the chordwise deflexion amplitude on  $\eta$  and  $C_t$ , calculations were done for a half chord elastic rectangular foil. Geometry and motion parameters were taken as the same as those in Yamaguchi (1992) and they were itemized in Appendix B. The chordwise deflexion equation, the pitching axis location and the deflexion phase angle, however, were not available, hence, they were taken as  $Cl$ ,  $x_{pitch}^*$  and  $-30^\circ$ , respectively.

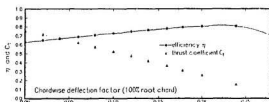


Figure 7.5: Effect of the chordwise deflexion factor  $\delta_{co}$  on the efficiency  $\eta$  and the thrust coefficient  $C_t$  for a rectangular half elastic chord oscillating foil.

Figure 7.5 shows the changes of  $\eta$  and  $C_t$  with the different chordwise deflexion amplitude. When the amplitude factor  $\delta_{co}$  was less than 0.2, efficiency increased linearly but the thrust dropped rapidly. This trend agrees with Bose's 2-D work (1992). When the chordwise deflexion factor  $\delta_{co}$  was greater than 0.2, the thrust approached zero quickly with a large drop in efficiency.

As there are so many parameters affecting the propulsive performance, figure 7.5 indicates that an overall propulsive performance cannot be obtained by adjusting only the chordwise deflexion amplitude itself. In many cases, a large amount of thrust has to be sacrificed to obtain a higher efficiency.

Figures 7.6 to 7.8 show the chordwise pressure distribution at each section, for a deflexion amplitudes of 0.0 (no deflexion), 20% chord and 28% chord, respectively. The instantaneous position was taken at the 240th time step (a total number of time

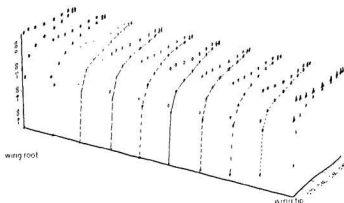


Figure 7.6: Pressure distribution  $C_p$  at zero chordwise deflexion for a rectangular half elastic chord oscillating foil.

steps equals 256) at an angular displacement of  $7.5\pi$  and a time displacement of 17.4948 seconds.

At this instantaneous time step, the maximum hydrodynamical forces in a cycle for these three different amplitudes of deflexion were obtained. The value of these forces should be multiplied by the dynamic pressure  $\frac{1}{2}\rho V_{flight}^2$  and the area of the planform. The units of these forces are therefore in Newtons.

These non-dimensional forces are as follows:

1. Total lift is -513.972, -125.986 and -71.3279.
2. Total thrust is -341.709, -100.300 and -52.2584 (Foil goes to the negative x-direction; this is positive instantaneous thrust relative to the motion of the foil. The mean thrust, however, should be positive due to the formulation of the method.).
3. Friction drag is 2.90524, 2.99726 and 2.98881.
4. Total pitch moment 1347.57, 1297.88 and 1030.63.
5.  $C_L$  is 1.498460, 0.367306 and 0.207953.

6.  $C_T$  is -0.996235, -0.292419 and -0.152357.
7. Skin friction coefficient is 0.008464, 0.008775 and 0.008437
8.  $C_T$  with skin friction is -0.987765, -0.293681 and -0.143643.

The negative  $C_T$  shows a positive thrust because the oscillating foil was assumed to move in the negative  $x$ -direction.

When there was no deflexion, the pressure distribution had a profile similar to that for a steady foil. At a larger chordwise deflexion of 0.2, the pressure coefficient  $C_p$  on the pressure side dropped dramatically on the flexible part of the foil. As the deflexion continued to increase, this drop increased. Therefore, the lift and thrust were small for these larger deflexions.

The efficiency, however, kept increasing with the increase of the deflexion, because the deflexion increased the instantaneous pitch angle, so that the difference between the instantaneous pitch angle and the instantaneous pitching axis' kinematic velocity became smaller; i.e., the instantaneous angle of attack became smaller. Therefore, the lift and thrust dropped.

It can be seen that, even though the foil had such high lift, thrust and pitch moment at this time step, the pressure differences at the trailing edges, for both the rigid and the flexible foil, were very small. This again indicates that as long as the time step size, the total number of time steps and proper numerical procedure are carefully chosen, the validity of the steady Kutta condition will remain in a flow round a flexible unsteady foil. However the pressure difference at the trailing edge may not, in practice, be zero in certain cases, and this has to be tested by somewhat advanced and sophisticated experimental studies.

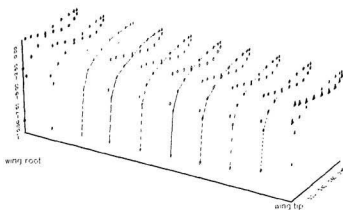


Figure 7.7: Pressure distribution  $C_p$  at a 20% chordwise deflexion for a rectangular half elastic chord oscillating foil.

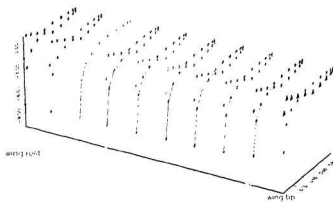


Figure 7.8: Pressure distribution  $C_p$  at a 28% chordwise deflexion for a rectangular half elastic chord oscillating foil.

## 7-E The effect of spanwise deflexion amplitude on efficiency and thrust

Calculations were done for a fin whale's flukes to examine the effect of amplitude of the spanwise deflexion on  $\eta$  and  $C_t$  and the results are presented in figure 7.9. The following parameters of motion were used:

- Planform geometry was the same as that in Chapter 5.
- Chordwise deflexion amplitude factor  $\delta_{co} = 0$ .
- Spanwise deflexion equation was S1, the basic normalized cantilever beam deflexion function.
- Oscillating frequency was  $0.2\pi$ .
- Pitching amplitude  $\alpha_o = 20^\circ$ .
- Heave amplitude factor  $h_o = h_{heave}/C_r = 0.87 \text{ m}/0.87 \text{ m} = 1.0$ .
- Fluke swimming speed  $V_{flight}^* = V_{flight}/C_r = 0.87/0.87 = 1.0/\text{sec}$ .
- The corresponding small and large amplitude feathering parameters  $\theta = 0.5556$  and  $\Theta = 0.6222$ .
- Spanwise deflexion phase angle lagging pitch  $0^\circ$ .
- Pitch axis position factor  $x_{pitch}^* = x_{pitch}/C_r = 0.87/0.87 = 1.0$ .

Figure 7.9 indicates that when the flukes did not have a positive flexibility, increasing the spanwise deflexion will decrease the efficiency and thrust. As  $L\dot{h}$  in equation (7.6) is part of the denominator in equation (3.59), the sign of  $V_j$  and  $\dot{h}_{root}$  affect the value of  $P_{input,A}$ . For a spanwise deflexion phase angle of zero degrees, the signs of  $V_j$  and  $\dot{h}_{root}$  were opposite at all times so that the efficiency was large (see figure 7.10); at a large degree of phase angle,  $V_j$  and  $\dot{h}_{root}$  may have had the same sign

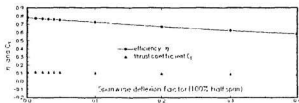


Figure 7.9: Effect of the spanwise deflection factor  $\delta_{s0}$  on the efficiency  $\eta$  and the thrust coefficient  $C_t$  for a fin whale's flukes.

at a certain instant so that they add up. Therefore, the larger the spanwise deflection, the smaller the efficiency (figure 7.10).

It is suggested that to obtain a higher efficiency for a passive deflexion, the spanwise deflexion amplitude should be controlled at around zero (rigid span). In the case of bird flights, and especially in the case of swimming of whale, however, active deflexion control mechanism may have a phase angle of  $180^\circ$  (tips go down on downstroke when foil is going up and vice versa).

A controllable chordwise and spanwise man-made oscillating foil, if it is practical in reality, is to be designed to have an active spanwise deflexion (spanwise flap of a rigid halfspan hinged at the root chord) and a passive chordwise deflexion with a phase lag of around  $35^\circ$  (reducing the load by decreasing the instantaneous angle of attack due to the chordwise flexibility).

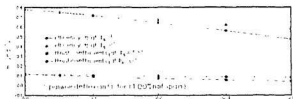


Figure 7.10: Effect of the spanwise deflection amplitude factor  $\delta_{s0}$  and the phase angle  $\phi_s$  on the efficiency  $\eta$  and the thrust coefficient  $C_t$  for a fin whale's flukes.

For an appropriate phase angle control ( $\Phi_s = 180^\circ$ ), a bigger spanwise deflexion amplitude factor  $\delta_s$  was desired to yield a higher efficiency and thrust, but the ratio of  $\delta_s/h_s$  has to be controlled to obtain a positive thrust. However, the best ratio for both the efficiency  $\eta$  and the thrust coefficient  $C_t$  may not be obtained for all cases, because this ratio depends on the shape of the planform, chordwise deflexion parameters and the motion parameters.

## 7-F Propulsive performance of a rectangular flexible foil

Computations were done for a rectangular foil with and without chordwise deflexion. The motion parameters (Yamaguchi 1992), were set as follows:

- Pitching amplitude  $\alpha_o = 15.8^\circ$  and  $\alpha_o = 19.7^\circ$ , for the rigid and flexible planforms, respectively;
- Phase angle of pitch leading heave  $\Phi_{pitch} = 105^\circ$  and  $\Phi_{pitch} = 104^\circ$ , for the rigid and flexible planforms, respectively;
- Heave amplitude factor  $h_o = h_{heave}/C_t = 4.2 \text{ m}/7 \text{ m} = 0.6$ .
- Oscillating frequency  $\omega$  was set as 0.6241, 0.7644, 0.9043, 1.047, and 1.123 for the rigid foil and 0.7562, 0.9434, 1.1265, 1.3125, 1.4097 for the semi chordwise elastic foil.
- The swimming forward velocity  $V_{flight}$  was obtained as 4.3822, 5.477, 6.573, 7.669 and 8.217  $\text{m/s}$ , respectively.

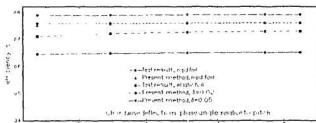


Figure 7.11: Efficiency  $\eta$  versus swimming speed  $V_{flight}$  of a rectangular rigid/elastic propulsor from Yamaguchi (1992), a 2-D theory with 3-D modification and the present method with 2% and 5% chordwise deflexions.

The pitching axis position was assumed at  $X_{pitch}^* = 1.0$ . The chordwise deflexion phase angle  $\Phi_c$  was taken as  $-30^\circ$ . The deflexion amplitude was assumed to be 5%

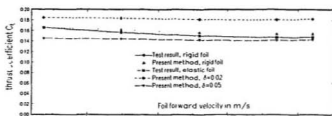


Figure 7.12: Thrust coefficient  $C_T$  versus swimming speed of a rectangular rigid/elastic propulsor from Yamaguchi (1992), a 2-D theory with 3-D modification and the present method with 2% and 5% chordwise deflexions.

of chord length. As these parameters were not given in Yamaguchi 1992, they were pre-assumed.

Figure 7.11 and 7.12 show the 2-D numerical results versus the results predicted by the present method in determining efficiency for the rigid and elastic foil. The prediction for the rigid foil from the present method showed a higher thrust and efficiency than those from Yamaguchi 1992. As the rigid foil in his study had a pitch amplitude  $\alpha_0 = 15.8^\circ$ , the maximum velocity angle  $\alpha_v$  of the foil was about  $31^\circ$  and the phase angle  $\Phi_{\text{phase}}$  was  $14^\circ$ , and the maximum instantaneous angle of attack was about  $\alpha_{\text{instant}} \sim 16^\circ$  (see figure 7.13 or 7.14). Such a large instantaneous angle of attack  $\alpha_{\text{instant}}$  would probably have led to a boundary layer separation and hence a reduction of the efficiency and the thrust for the 2-D calculations. As the

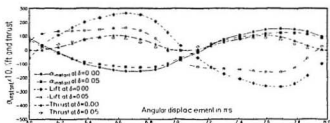


Figure 7.13: Comparison of the instantaneous angle of attack, lift and thrust between a rigid and a flexible (5% chord), a size of  $49 \text{ m} \times 7 \text{ m}$ , rectangular foil at  $V_{\text{flight}} = [8.217 \text{ m/s}]/C_r = 1.174/\text{s}$ .

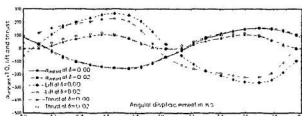


Figure 7.14: Comparison of the instantaneous angle of attack, lift and thrust between a rigid and a flexible (2% chord), a size of  $49 \text{ m} \times 7 \text{ m}$ , rectangular foil at  $V_{flight}^* = [8.217 \text{ m/s}]/C_r = 1.174/s$ .

present method cannot take the lift reduction due to the boundary layer separation into account, it gave higher values of efficiency and thrust. However, the present method was able to give the value of  $\alpha_{instant}$  at each time step to warn for a possible boundary layer separation.

Predictions for the elastic planform by the present method show that a very small chordwise deflection did not result in a noticeable gain in efficiency compared with the rigid foil. As the thrust from the 2-D panel method was obtained at the same velocity for these two planforms, the thrust coefficient for both the rigid and the elastic foils were the same (the solid line in figures 7.13 and 7.14). Therefore, there are four curves representing five quantities. It can be seen that a small amount of chordwise deflection produced negligible change in efficiency but yielded a significant change in the thrust. For a relatively large chordwise deflection ( $\delta_{co} = 0.05$ ), the thrust decreased slightly with about the same portion as the increase of the efficiency.

Figures 7.13 and 7.14 present the instantaneous angle of attack, lift and thrust for the planforms with 5% and 2% chordwise flexibility, predicted by the present method. In figure 7.13, the graph of the instantaneous lift was rather flat for the 5% deflection foil while that of the rigid foil looks like a sinusoidal wave. As the instantaneous pitch angle  $\alpha$  was increased due to the chordwise flexibility (so that it was closer to the instantaneous kinematic velocity  $\alpha_w$  of the pitching axis), the instantaneous angle of attack had a fair amount of reduction; depending on the chordwise deflection

amplitude (  $\delta_c = 0.05 \sim 0.2$  ), this reduction usually ranged from  $5^\circ$  to  $20^\circ$ .

Figure 7.14 shows a rather irregular behaviour for a foil with a very small chordwise deflexion. This small amount of deflexion increased the pitch angle so that the instantaneous angle of attack should normally be smaller than the rigid foil. Here, the instantaneous angle of attack was larger because the chordwise deflexion phase angle was taken as  $-30^\circ$  (a slight control of the deflexion). This pattern also existed with the 5% deflexion planform. However, as the instantaneous angle of attack dropped rapidly at about every half  $\pi$  rad of angular displacement for the 5% chordwise deflexion foil, the mean thrust was much smaller than that of a rigid foil.

## 7-G Propulsive performance of a fin whale's flukes

To examine the propulsive performance of a fin whale's flukes as a propeller, computations were done by using a number of motion parameters based on the study of Bose and Lien (1992). Some motion parameters are:

- heave amplitude factor  $h_0 = 1.723$  because of  $h$  being taken as 1.5 meters;
- pitch axis position starting at the T.E.,  $X_{pitch}^* = 1.0$ ;
- pitch leading heave at  $\Phi_{pitch} = 90^\circ$ ;
- oscillating frequency  $\omega = 3$  rad/sec;
- swimming forward velocity  $V_{flight} = 4, 6, 8, 10$  and  $12$  m/sec.

Besides the above motion parameters, some additional parameters were used for the flexibility:

- chordwise deflexion amplitude factor  $\delta_{co} = 0.05$ ;
- spanwise deflexion amplitude factor  $\delta_{sw} = 0.1$ ;
- chordwise deflexion phase angle  $\Phi_c = -30^\circ$ ;
- spanwise deflexion phase angle  $\Phi_s = -30^\circ$  and  $-180^\circ$ ;
- deflexion shape function set C3S3.

Calculations for a flexible planform were made for two cases: a) for  $\Phi_s = -30^\circ$ , both the spanwise and the chordwise flexibility were assumed as passive deflexion (no muscle control); b) a passive chordwise and an active spanwise control for the deflexion.

A non-dimensional advance ratio was used and defined as

$$J^* = \frac{V_{flight}}{\omega c'_r} \quad (7.7)$$

$V_{flight}$ (m/s)	4.0	6.0	8.0	10.0	12.0
$V_{flight}$ (knots)	7.8	11.7	15.6	19.5	23.3
$\alpha_v$ (deg)	48.37	36.86	29.58	24.23	20.56
$J^* = \frac{V_{flight}}{\omega C_r}$	1.71	2.56	3.42	4.27	5.13
$\alpha$ (deg)	28.12	16.61	9.33	4.98	2.31
$\alpha_{instant,max}$ (deg)	15.50	12.75	11.65	10.69	9.776
$\Theta$	0.5816	0.4507	0.3180	0.2057	0.1124

Table 7.2: Determination of an appropriate pitch amplitude for the flexible planforms with and without active control.

The pitch amplitudes for the elastic planform were determined by considering the efficiency, thrust and boundary layer separation; that is, to use a maximum possible instantaneous angle of attack. This maximum possible value was set at about  $12^\circ$ , with a consideration that this value may be allowed to be slightly larger because this maximum value occurred only in a small range of one oscillating cycle so that, even if boundary separation occurs in that range, it would probably not affect the overall performance.

Using a pitch amplitude of  $50^\circ$  as it was taken in Bose and Lien (1989), it is not possible for this large amplitude theory to yield a positive thrust. If such a large pitch amplitude has to be used, either the heave amplitude or the oscillating frequency should be increased or the swim velocity should be decreased to have an instantaneous large amplitude feathering parameter less than 1.0. As can be seen in table 7.2, the maximum angle of the instantaneous kinematic velocity of the pitch axis was  $48.37^\circ$ . Any pitch angle that is greater than this value yielded a negative thrust. This was obvious when the large amplitude was considered (Chapter 6).

Based on the above considerations and a number of trial computations, the pitch amplitude for each forward speed was selected and some related quantities are tabulated in table 7.2.

For a rigid foil, if a desired maximum angle of attack is  $12^\circ$ , the pitch amplitude should be set as  $48.37^\circ - 12^\circ = 36.37^\circ$  at a forward velocity of  $4$  m/s. However, for the fin whale's flukes section with a 5% chordwise deflexion, the change of the maximum

$V_{flight}$ (m/s)	4.0	6.0	8.0	10.0	12.0
$\alpha_{instant,max}$ (deg)	15.50	12.75	11.65	10.69	9.776
$\Theta$	0.5816	0.4507	0.3180	0.2057	0.1124
$\eta$	0.7806	0.8154	0.8278	0.8292	0.8180
$C_t$	0.1409	0.1108	0.0935	0.0749	0.0575
Thrust (kN)	1.69	2.99	4.49	5.62	6.21
$P_{input}$ (factor)	1.079	1.222	1.3579	1.3633	1.2829
Power (kW)	8.63	22.0	43.45	68.17	92.37

Table 7.3: Propulsive performance of the fin whale's flukes without an active spanwise deflexion control ( $\Phi_s = -30^\circ$ ) and with a skin friction consideration.

$V_{flight}$ (m/s)	4.0	6.0	8.0	10.0	12.0
$\alpha_{instant,max}$ (deg)	15.50	12.75	11.65	10.69	9.776
$\Theta$	0.5816	0.4507	0.3180	0.2057	0.1124
$\eta$	0.8079	0.8670	0.8965	0.8942	0.8559
$C_t$	0.1621	0.1327	0.1122	0.0861	0.0619
Thrust (kN)	1.95	3.58	5.39	6.46	6.69
$P_{input}$ (factor)	1.0794	1.3741	1.5039	1.4524	1.3184
Power (kW)	8.64	24.73	48.13	72.60	94.93

Table 7.4: Propulsive performance of the fin whale's flukes with an active control ( $\Phi_s = 180^\circ$ ) and with a skin friction consideration.

angle of attack was about  $13.25^\circ$ , i.e., an extra  $13.25^\circ$  had been added to the pitch due to the flexibility. Therefore, to control the maximum angle of attack at about  $12^\circ$ , the pitch amplitude had to be set at  $48.37^\circ - 12^\circ - 13.25^\circ = 23.12^\circ$ .

In addition, a phase angle of  $-30^\circ$  in chordwise deflexion shifted the point at which the maximum pitch angle  $\alpha$  and the maximum velocity angle  $\alpha_w$  coincide. This shift reduced the maximum angle of attack by about  $5^\circ$ . Therefore, the pitch amplitude was set at  $28.12^\circ$  in order to expect a maximum instantaneous angle of attack close to  $12^\circ$ .

The large amplitude feathering parameter  $\Theta_{flexible}$  was obtained by neglecting the spanwise deflexion, though the spanwise deflexion had affected the pitching axis'

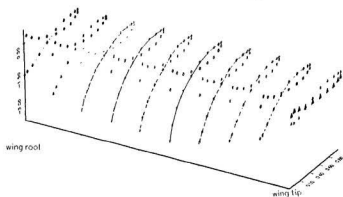


Figure 7.15: Pressure distribution  $C_p$  for a fin whale's flukes with a spanwise deflexion phase angle of  $\Phi_s = -30^\circ$  (passive deflexion) and  $t = 17.4948$  sec (the 240th time step).

velocity. For a large spanwise deflexion, a value of  $\Theta_{fcrible}$  that is greater than zero and less than one may not produce a positive thrust due to too small an average heave amplitude.

Tables 7.3 and 7.4 show the results from a fin whale's flukes with and without an active deflexion control (the deflexion phase angles were zero). In the tables, efficiency, thrust coefficient and  $P_{input}$  were obtained after a reduction of skin friction. The thrust was obtained by multiplying the wing area  $S$  and the reference dynamic pressure  $\frac{1}{2}\rho V_{flight}^2$ . The required input power was, then, a product of the  $P_{input}$  factor, the planform area  $S$  and the reference dynamic pressure  $\frac{1}{2}\rho V_{flight}^2$ .

The predicted efficiency in tables 7.3 and 7.4 show that the best efficiency occurred at the maximum instantaneous angle of attack about  $10^\circ$ . This is the same with the observations made for the rigid rectangular and the swept planforms.

It can be seen that when the flukes had a positive flexibility control, both efficiency and thrust had a substantial increase. In a normal range of the instantaneous angle of attack, the smaller the value of  $\Theta$ , the higher the efficiency and the lower the thrust. When the mean thrust was very small at a large forward speed (12 m/s), the skin friction cancelled a large portion of the thrust and, hence, the predicted efficiency

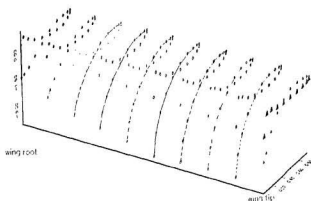


Figure 7.16: Pressure distribution  $C_p$  for a fin whale's flukes with a spanwise deflexion phase angle of  $\Phi_s = 180^\circ$  (active deflexion control) and  $t = 37.5$  sec.

became smaller, even though the value of  $\Theta$  was very small.

Figures 7.15 and 7.16 show the pressure distributions of the fin whale's flukes with and without active spanwise deflexion control. The x-ordinates at where the  $C_p$  value is located were normalized to provide a clear visualization.

It can be seen that when the planform did not have an active deflexion control (simulating a passive deflexion), the pressure coefficient  $C_p$  had a small difference between the pressure and the suction sides, especially at the flukes's tips. The chord length of the tip of the planform was set at 0.012 m, which is about 1.4% of the root chord. This small chord length was set to approximate a point tip of the planform. Even with such a small relative local chord, the predicted pressure distribution from the present method appeared normal.

When the spanwise deflexion had an active deflexion control at a phase angle of  $180^\circ$ , the difference in  $C_p$  increased at all sections and, hence, so did the efficiency and the thrust. As the predicted pressure difference at the trailing edge is very small (see figures 7.15 and 7.16), the Kutta condition used in this method along with the selection of the number of time steps and the time step size were considered acceptable.

## Chapter 8

### Conclusions

This is the first attempt to evaluate the propulsive performance from an oscillating propeller with both spanwise and chordwise flexibility. A new system of approaches was developed based on a classical time domain panel method, to calculate the performance of a non-zero sectional thickness, unsteady, flexible, three-dimensional, large amplitude oscillating propulsor including the consideration of viscous skin friction and the allowance of a non-zero trailing edge thickness. In order to obtain reliable results, a series of tests was done covering a rigorous convergence study and a careful verification analysis. When the method was proven accurate and dependable, it was then used to predict the propulsive performance.

A large amplitude theory was developed and the instantaneous angle of attack, the large amplitude feathering parameter and the instantaneous large amplitude feathering parameter were defined.

As previous results on 3-D rigid oscillating foils were obtained based on small amplitude theory without considering the sectional thickness and the effect of skin friction, a parametric study was done to re-examine the effect of geometry and motion parameters on the propulsive performance of a 3-D rigid oscillating foil.

For flexible 3-D foils, a number of deflexion equations in both the chordwise and the spanwise directions were pre-assumed to simulate the fin whale's flukes or the flexible wing. Propulsive performance was evaluated for oscillating propellers with

different amplitudes of the chordwise and the spanwise deflexion. The phase lags of both chordwise and the spanwise deflexion were introduced to examine their effect on the efficiency and thrust. Predictions were also obtained for a  $49\text{ m} \times 7\text{ m}$  rectangular, semi-chordwise flexible foil and results were compared with those from a 2-D panel method. Finally, a fin whale's flukes with both spanwise and chordwise flexibility was used to evaluate its propulsive performance.

## 8-A About the method

In steady flow, this low order, Dirichlet boundary condition 3-D panel method was proven reliable, when the foil under consideration did not have a very small aspect ratio. The predicted results were accurate and reliable for the hydrodynamic loads and pressure distribution. The steady Kutta condition worked well for the steady flow when the time step size was taken sufficiently small. In the steady flow, only two things need to be considered in order to obtain accurate results: a) the number of chordwise and spanwise panels should be large enough to converge; b) the total number of time steps should be large enough to keep a small time step size and to minimize the effect of the starting vortices in order to have a realistic pressure distribution.

Application of the potential jump due to the kinematic velocity at the trailing edge enabled this method to allow a non-zero thickness trailing edge wing geometry. The quadratic function curve fits for the surface doublet distribution in both the chordwise and spanwise directions were formulated and the tangential velocities were obtained by differentiating the second order polynomial exactly at both middle points and the surface boundaries. These approaches improved the pressure distribution when a structured panel arrangement is used.

A number of approaches were implemented into the unsteady flow calculation: a) The time variant doublet strength at each panel were polyfitted to a quadratic function and the differentiation with respect to time was then obtained from this quadratic function exactly. This scheme improved the steady Kutta condition when it was used in the unsteady flow; b) The doublet strength of the last and the present shed wake panel at the trailing edge were averaged for each time step. This also improved the convergence behaviour or reduced the total number of required time steps for the same degree of accuracy. c) As the shed vortices behind the oscillating foil were also a function of the oscillating frequency  $\omega$ , a non-dimensional time  $t$  as used in previous studies is not sufficient to be generally used to determine the time step size. Therefore, a number of tests were done and the time step size was suggested

to be determined based on the period  $T = 2\pi/\omega$ . At a small oscillating frequency, the time step size can be taken as a large value, and vice versa, i.e.,  $\delta t = T/N_t$ , where  $N_t$  is the total number of time steps. The value of  $N_t$  greater than or equal to 256 was believed acceptable in the consideration of both the accuracy and the CPU time on a P120 (Intel Pentium 120 MHz processor) PC. The scheme that uses the period  $T$  along with  $N_t = 256$  to determine the size of the time step is advantageous to maintain the validity of the steady Kutta condition in unsteady flow.

A convergence study for unsteady flow was also done. A bigger number of spanwise panels NSpInt improved the convergence more effectively than to increase the number of chordwise panels, but too big a value will significantly use up more memory and add more manipulations. A stable prediction on cyclical thrust and lift was obtained after three cycles of oscillation. Therefore, the total number of cycles of all oscillating propellers was taken as 4 (4 periods or  $8\pi$  rad of angular displacement). Values in the last cycle were used to obtain the efficiency and the mean thrust.

A large amplitude theory was developed. In the theory, the instantaneous angle of attack of the oscillating foil was defined as the instantaneous angle between the instantaneous pitch angle (the instantaneous position of the foil) and the instantaneous angle of the kinematic velocity vector of the foil's pitch axis. The large amplitude feathering parameter and its instantaneous value were also defined. They were used to present the prediction and to analyze the propulsive performance.

For a foil with chordwise flexibility, the instantaneous pitch angle changes due to the change of the shape of the foil section. A numerical procedure was also established to determine the effective instantaneous pitch angle and hence the instantaneous angle of attack.

The determination of the instantaneous angle of attack was found to be a rule of thumb in analyses of the changes in lift, thrust, large amplitude feathering parameters with a variation of heave amplitude, pitch amplitude, and the chordwise deflexion. This is because the instantaneous angle of attack has a definite value corresponding to a combination of the above parameters and the efficiency and thrust are found directly dependent on this definite value. A preliminary design of an oscillating foil

in terms of parameters can be easily done by properly selecting this instantaneous angle of attack without doing a hydrodynamic computation. It was also useful to warn of a possible boundary layer separation due to too large an instantaneous angle of attack, for both rigid and flexible foils.

A numerical procedure was also developed and applied to the calculations of the foils with the spanwise flexibility. Spanwise flexibility affected the heave velocity, i.e., the vertical velocity varied across the span for each section. Instead of evaluating the  $L\dot{h}$  term for a whole planform, sectional  $L\dot{h}$  was obtained and summed for the whole planform in the efficiency calculation.

A numerical scheme to calculate the skin friction coefficient for a 3-D, unsteady, flexible foil was also formulated based on a 2-D flow assumption at each section. The velocity gradient along each section was used to determine the flow pattern, in terms of laminar, laminar separation, turbulent transition, turbulent and turbulent separation, and the skin friction coefficient  $C_f$ .

The computer program OSFBEM can be used when the DRAM is small in which case binary files are created to store the matrices, instead of a very slow virtual memory swap. However, when there is enough DRAM run times are about five times faster. A reliable, fast matrix solver by applying the Bi-CGSTAB method was implemented. By using the steepest descent steps, the Bi-CGSTAB method gives a smooth and fast convergence while avoiding the often irregular convergence patterns of other nonsymmetric linear system solvers, such as the BiCG (BiConjugate Gradient) method and the CGS (Conjugate Gradient Squared) method. This method was then used to solve the linear system iteratively. The use of this method significantly increased the computing efficiency.

## 8-B Verification of the method

Results for a 2-D foil section were first verified. When the aspect ratio of a 3-D rectangular foil was set to 1000, predicted lift and pressure distributions were compared with those of a 2-D foil obtained from a theoretical approach. The method showed a good accuracy and reliability (even though a small number of panels was used) in terms of the pressure distribution and the value of the lift coefficient (3% in difference).

The pressure distribution at the extreme point, at the tip (98.75% halfspan) of a 3-D foil, was obtained and compared with experimental results. The present method had a good overall agreement, except at the trailing edge, where the experimental results did not agree with the Kutta condition (non-zero pressure difference).

Comparisons were also made for a 30° swept,  $\frac{1}{3}$  taper, 2% thickness thin wing with an aspect ratio of 6. This method showed a general agreement among others and a better trailing edge Kutta condition (less amount of the trailing edge pressure difference) was obtained which often implies a better accuracy.

Finally, as there were no theoretical results that are based on a large amplitude assumption available, predictions of efficiency and thrust from a rectangular foil were compared with the results from a linearized lifting surface theory. There was a slight difference between the methods at a small reduced frequency ( $k < 0.5$ ) but a substantial difference at higher reduced frequency ( $k \approx 2$ ). Results indicated that the linearized lifting surface theory applied to evaluate the propulsive performance had a limited validity in a small range. The present method, had an incomparable smaller thrust than previous ones, in the working range of the reduced frequency about  $k = 1.0$ . As the previous method used in comparison was a small amplitude assumption (the instantaneous angle of attack for the small amplitude theory was about as twice as large (12.68° vs. 20.92°), which was the major cause of the difference in thrust production) and did not consider the foil thickness, the thrust prediction by present method is believed more accurate and more reliable.

## 8-C Large amplitude analysis and parametric study of a rigid oscillating propeller

As the results from a method that takes the large amplitude, thickness effect, 3-D geometry and viscous skin friction into account were not available, a parametric study for a rigid foil was found necessary and was hence conducted.

A large amplitude analysis was performed and it was used to determine the large amplitude feathering parameter and the instantaneous angle of attack. This indicated that the small amplitude theory at a large reduced frequency and a large feathering parameter ( $\Theta = 0.4$  and  $k = 1.8$ ) predicted an instantaneous angle of attack about twice that of large amplitude theory and, hence, it had a very large thrust production. A comparison was done and it showed that the small amplitude assumption had a thrust over prediction about five times at the above values of  $\Theta$  and  $k$ . Meanwhile, the value of the instantaneous angle of attack at  $\Theta = 0.8$  and  $k = 1.8$  for the small amplitude theory was too large ( $20.68^\circ$ ). Such big an angle of attack would cause a severe boundary layer separation even in a steady flow.

In addition, the instantaneous angle of attack is usually close to zero at a large  $\Theta$  and a small  $k$  for the large amplitude theory. Therefore, the calculated drag by the present method cancelled a large portion of the small amount of the predicted thrust so that the present method yielded a smaller efficiency and a much lower thrust.

At a large reduced frequency, significant errors in efficiency and thrust were found for the small amplitude approximation. The error for the thrust production could be as much as 50%. As a result of the large amplitude study, the pitch amplitude is not suitable to be used to determine its effect on the propulsive efficiency. Instead, the maximum instantaneous angle of attack defined by the present method plays an important role among other propulsive parameters. Predictions show that for either a rectangular or a swept wing, for either a rigid or a flexible planform, the best efficiency occurred at the maximum instantaneous angle of attack  $\alpha_{instant,max}$  about  $10^\circ$ .

The finding of the optimal angle, the maximum instantaneous angle of attack provides a direct control of a combination of the motion parameters to obtain the

best efficiency. This means that a combination of motion parameters for rigid foils can be approximately optimized by adjusting the maximum instantaneous angle of attack without performing a tedious hydrodynamic calculation.

Indication of the instantaneous angle of attack (or the instantaneous feathering parameter) was also found useful to observe the sign of the generated thrust. An instantaneous feathering parameter greater than 1 will lead to a negative generated instantaneous thrust. Therefore, if this is the case, the problem can be solved so that either the pitch amplitude, or phase angle (pitch leading heave), or the ratio of the velocity derivative  $\dot{f}(t)$  to  $V_{flight}$  (i.e., the denominator of eq. (6.1)) needs to be adjusted to maintain an instantaneous feathering parameter less than 1. The phase angle (pitch leads heave) had an effect on the instantaneous large amplitude feathering parameter. As the phase angle has a direct effect on the instantaneous pitch angle, the instantaneous large amplitude feathering parameter may be greater than 1, if the phase angle is far away from  $90^\circ$  even if an overall value of the large amplitude feathering parameter is less than 1 (comparing eq. (6.1) with eq. (6.3)).

Examination of the effect of the heave amplitude on the thrust and efficiency showed that increasing the heave amplitude raised the thrust significantly, because of the increased value of the instantaneous angle of attack. This suggests that an oscillating foil should be set at the maximum possible heave amplitude for the best possible thrust.

For a foil with all parameters fixed and only the pitch amplitude  $\alpha_0$  as a variable, the thrust decreased when the pitch amplitude  $\alpha_0$  increased, because increasing the pitch amplitude reduces the instantaneous angle of attack. The best efficiency, however, occurred at a certain pitch amplitude with a smaller amount of thrust. In any case, the best efficiency was obtained at the maximum instantaneous angle of attack of about  $10^\circ$ .

When other parameters being fixed, an optimum pitch amplitude was found for the best efficiency. However, this optimum pitch amplitude is only valid in a particular combination of parameters. The best efficiency, in fact, was again controlled by the maximum instantaneous angle of attack. At the optimum pitch amplitude point,

increasing the pitch amplitude, both the efficiency and the thrust were increased, though in most cases, increasing efficiency will reduce the thrust output.

As in previous studies, a good pitching axis position for the best efficiency was in a range from 50% to 100% root chord from the leading edge.

The best efficiency can be obtained at an optimized phase angle. The thrust, however, had not much change in a wide range of the phase angle values. From  $\Phi_{phase} = 0^\circ$  to  $180^\circ$ , the relation, "the higher the efficiency, the lower the thrust" did not appear as it was stated in previous studies. In fact, after the point where the efficiency reached highest value (at the maximum instantaneous angle of attack of  $10^\circ$ ), the higher the efficiency the higher the thrust. This reversed relationship exists after the point at which the maximum efficiency occurred (see figure 6.5).

Sectional thickness ratio had little effect on the efficiency for a series of NACA 4-digit symmetrical wing sections. The best efficiency occurred around 9% ~ 12%. The thrust, however, had a good value of 0.4 (about the same as that for 6% thick section) at a thickness of  $t = 12\%$  chord. When  $t < 9\%$ , the smaller the thickness ratio, the higher the thrust. This may be caused by the sharp leading edge that brought a big leading edge suction. This larger increase in thrust due to the reduction of thickness may not be practical due to the pressure drop when the pressure at the leading edge below the vapour pressure. When  $t > 15\%$ , thrust dropped dramatically with an increase of  $t$ .

Comparison between the linearized lifting surface theory and the large amplitude panel method was also done for both a man-made lunate tail and a fin whale's flukes. The present method gave a smaller efficiency prediction and much lower thrust values. Because the present method considered the section thickness effect, the large amplitude assumption and the skin friction effect, results from the present method are believed more practical. The extremely large  $C_l$  value from the lifting surface theory indicates that this value was over estimated due to too big (impractical) an instantaneous angle of attack and that the assumption of a zero-thickness wing section had a disadvantage in calculating thrust because it over-predicted the leading edge suction.

Study of the effect of the swept planforms on the thrust and efficiency gives the following conclusions:

- A lunate planform had a much better efficiency over that of a rectangular planform, at a feathering parameter of  $\Theta = 0$ . At this value, the load of the propeller was maximum. The thrust from the lunate tail was slightly smaller.
- At a higher feathering parameter of 0.4, the rectangular planform gave a slightly higher efficiency but a lower thrust in a working range of reduced frequency  $k$  ( $0.5 \sim 1.5$ ). Again, under extreme load conditions (very light load at  $k \leq 0.4$  or very heavy load  $k \geq 1.8$ ), the man-made lunate tail behaved better in terms of both the efficiency and thrust.
- The fin whale's flukes gave higher efficiency than that of a rectangular foil throughout the range of advance ratio  $J$ , especially at a higher advance ratio ( $J \geq 6$ ) at which the load is getting lighter. The fin whale's flukes showed an excellent energy efficiency (about  $\eta = 80\%$  and  $C_i = 0.1$  at  $J = 5.5$ ) at cruising, at which a minimum input power is required to maintain the cruising speed.
- The rectangular planform produced a slightly higher thrust over the flukes. However, the naturally occurring planform had a better overall performance.

The best efficiency, again, occurred when the maximum instantaneous angle of attack was at  $10^\circ$ , for both rectangular and swept planforms.

The skin friction coefficient  $C_f$  was obtained from the boundary layer calculation and was deducted from the thrust coefficient  $C_T$ . However, it had little effect on either the efficiency or the thrust. A significant effect occurred at a very low reduced frequency  $k$ , at which value, the generated thrust was very small so that the  $C_f$  cancelled out a large portion of the thrust.

## 8-D About flexible oscillating planforms

To simulate both a possible muscle control and a passive flexibility of a fin whale's flukes, five chordwise and three spanwise deflexion equations were tested.

Chordwise deflexion was assumed to start at the half local chord position and the deflexion was uniformly controlled by one equation for all sections and the local chord length for each section. Spanwise deflexion equations were postulated based on a cantilever beam with a uniform distributed load. Calculations showed that the selection of the governing equation had little effect on the efficiency and thrust.

A chordwise deflexion phase lag relative to the pitch was introduced and the study showed that a phase lag of about  $35^\circ$  gave the best efficiency (about 0.75) and about the same thrust coefficient (about 0.35). The graphic presentation of the motion and the wake of a rectangular planform showed that a phase lag about  $30^\circ$  seemed more practical and closer to the shape of a natural deflexion. This is shown in Appendix B that the deflexion of an elastic section cannot have an undeformed shape at the trough and peak where the vertical velocity is maximum when pitch leads heave about  $90^\circ$ .

The instantaneous angle of attack or the instantaneous large amplitude feathering parameter changed due to a) the change of the chordwise flexibility of the foil because the sectional shape was changed or twisted, b) the change of the phase lag between the chordwise deflexion and the pitch  $\Phi_c$ , because the sectional twist varies with time and c) the change of the phase angle  $\Phi_{phase}$ . In a normal case, at  $\Phi_{phase} = 90^\circ$  (heave lags pitch),  $\Phi_c = 0^\circ \sim 30^\circ$ , the chordwise flexibility played the most important role in the changes of the instantaneous angle of attack  $\alpha_{instant}$ . The effective value of the instantaneous angle of attack decreased when the flexibility or the amplitude of the chordwise deflexion  $\delta_c$  increased. Therefore, a lighter load had a higher efficiency and a lower thrust. When the chordwise deflexion amplitude  $\delta_{co}$  continued to increase, the efficiency  $\eta$  dropped due to the generated negative thrust; the total thrust also decreased. The decrease of the thrust due to the increase of the chordwise deflexion amplitude factor  $\delta_{co}$  was approximately linearly proportional, but the best efficiency was obtained at about a chordwise deflexion amplitude of 20% local chord. However,

at such a large deflexion, the thrust coefficient was very small (0.3). A medium deflexion of 10% chord gave a good overall thrust and efficiency ( $\eta = 0.75$  and  $C_t = 0.53$  for a rigid span rectangular planform).

The pressure distribution for a rectangular semi-elastic chordwise foil showed that the steady Kutta condition has been carefully applied and the present method is reliable for both the unsteady rigid and flexible foil. Though the value of the predicted pressure difference at the trailing edge varied from one time step to another and for different panel spacings, the pressure difference  $C_p$  at the maximum lift point ( $C_l = 10$ ) is about 0.01. At a larger amplitude chordwise deflexion, the pressure distribution on the pressure side became negative due to the substantially increased flow velocity. This negative value reduced the lift of the flexible section and hence the thrust. However, as the pitching moment had reduced significantly due to chordwise flexibility, the efficiency had an increase until the feathering parameter approached 1.0, at which points negative thrust was generated at certain instantaneous positions.

A spanwise deflexion phase angle (referring to the pitch)  $\Phi_s$  was also introduced and was used to study the propulsive performance of a fin whale's flukes. This phase angle  $\Phi_s$  had a substantial effect on the thrust and efficiency. When the phase angle was about  $0^\circ$ , the flukes always gave a lower value of both efficiency  $\eta$  and thrust  $C_t$ , compared with those obtained at spanwise deflexion amplitude  $\delta_{so}$  (rigid span). Especially, at a medium heave amplitude (about  $h/c = 1.0$ ), and a lower oscillating frequency  $\omega$  ( $0.2\pi$ ), the flukes hardly produced a positive thrust when both the chordwise and spanwise deflexion amplitude were set at 10% of chord and 10% half span respectively. Increasing either the heave amplitude, the oscillating frequency, or decreasing the swimming velocity will allow a larger degree of both chordwise and spanwise deflexion. In any case of a foil having a passive flexibility, there should be a large enough rigidity of an oscillating foil to yield a good propulsive performance in terms of both thrust and efficiency. However, when the phase angle  $\Phi_s$  was set at about  $180^\circ$ , at which value the flukes deflect downward when they heave upward and vice versa, both the efficiency  $\eta$  and thrust  $C_t$  had a substantial increase. Such active deflexion control mechanism (controllable flexibility), if it is possible for

an oscillating foil, can achieve a superior propulsive performance.

The amplitude of the spanwise deflexion factor  $\delta_{so}$  also had a noticeable effect on the efficiency  $\eta$  and thrust  $C_t$ . At a small angle of phase lag (about  $\Phi_s = 0^\circ$ ), the amplitude of a pure spanwise deflexion had little effect on the efficiency  $\eta$  and thrust  $C_t$ , and increasing the spanwise deflexion factor  $\delta_{so}$  decreased both the efficiency  $\eta$  and thrust  $C_t$ . A large chordwise deflexion amplitude  $\delta_{co}$  and spanwise deflexion amplitude  $\delta_{so}$  at a small heave amplitude produced a negative  $C_t$  (needed extra thrust to keep  $V_{flight}$ ). However, as it was mentioned before, if the spanwise deflexion phase angle  $\Phi_s$  changed to about more than  $90^\circ$ , a large spanwise deflexion amplitude  $\delta_{so}$  gave a much larger efficiency  $\eta$  and thrust  $C_t$ .

The propulsive performance for a rectangular semi-elastic foil was also predicted and the results were compared with a previous 2-D numerical study with a 3-D modification. The present method gave slightly higher values of the efficiency  $\eta$  and thrust  $C_t$ .

A fin whale's flukes was finally used to evaluate the oscillating propulsors' performance by using several carefully selected motion and flexibility parameters. A controllable spanwise flexibility being set at a phase angle of  $\pm 180^\circ$  (see figure B.35) gave a superior efficiency and thrust over the same planform with a passive deflexion (see figure B.37) which had about  $-60^\circ$  phase angle of spanwise deflexion. The fin whale, when an optimal active deflexion control (the phase angle of the spanwise deflexion was set at about  $\pm 180^\circ$ ) was employed, had an excellent efficiency ranging from 80% at 7.8 knots to 86% at 23 knots. The best efficiency, the same as any other planforms examined in this research, occurred at the maximum instantaneous angle of attack of about  $10^\circ$ .

## References

- [1] Abbott I. H. and von Doenhoff A. E. (1949). *Theory of Wing Sections*, Dover Publications, Inc., 693 p.
- [2] Acheson, D.J. (1990). *Elementary fluid dynamics*, Clarendon Press, Oxford, 397 p.
- [3] Albano, E. and Rodden, W.P. (1969). "A doublet-lattice method for calculating lift distribution on oscillating surfaces in subsonic flows," *AIAA Journal*, Vol. 7, No. 2, February, pp. 279 – 285.
- [4] Appa, K and Smith, M.J.C. (1989). "Evaluation of the constant pressure panel method for supersonic unsteady airloads prediction," *J. Aircraft*, vol. 26, No. 9, pp. 854 – 862.
- [5] Bachelor, G.K. (1967). *Fluid dynamics*, Cambridge University press, 615 p.
- [6] Banerjee, P.K. and Butterfield, R. (1981). *Boundary element methods in engineering science*, McGraw-Hill (UK), London, 452 p.
- [7] Barrett, R., Berry, M., Chan, T., Demmel, J., Donato, J., Dongarra J., Eijkhout, V., Pozo, R., Romine, C. and van der Vorst H. (1994). *Templates for the solution of linear systems: Building blocks for iterative methods*, Electronic book downloaded from [templatescs.utk.edu](http://templatescs.utk.edu), 113 p.
- [8] Basu, B.C. and Hancock, G.J. (1978). "The unsteady motion of a two-dimensional aerofoil in incompressible inviscid flow," *J. Fluid Mech.*, Vol. 87, Part 1, pp. 159 – 178.
- [9] Beker, J. (1973). "Interfering lifting surfaces in unsteady subsonic flow-comparison between theory and experiment," *AGARD Report No. 614*, North Atlantic Treaty Organization, Advisory Group for Aerospace Research and Development, 37th AGARD structures and materials panel meeting, The Hague, Netherlands, April 7-12, 1973, 15 p.
- [10] Bisplinghoff, R.L., Ashley, H. and Halfman, R.L. (1955). *Aeroelasticity*, Addison-Wesley publishing company, Inc., Reading, Massachusetts, 1955, 860 p.

- [11] Blair, M. and Williams, M.H. (1989). "A time domain method for wing," *AIAA Paper*, No. 89-1323, pp. 1417 – 1427.
- [12] Bosc, N. and Lien, J. (1989). "Propulsion of a fin whale (*Balaenoptera physalus*): why the fin whale is a fast swimmer," *Proc. R. Soc. Lond. B237*, pp. 175 – 120.
- [13] Bosc, N. and Lai, P. (1989). "Experimental Performance of a trochoidal propeller with high-aspect ratio blades," *Marine Technology*. Vol. 26 No. 3, pp. 192 – 201.
- [14] Bosc, N. (1993). "Propulsion performance of chordwise flexible oscillating foils using a time-domain panel method," 2nd Canadian Marine Dynamics Conference, Vancouver, August, 7 p.
- [15] Bosc, N., Lien, J. and Ahia, J. (1990). "Measurements of the bodies and flukes of several cetacean species: designs for fast and slow swimming," *Proc. R. Soc. Lond. B242*, pp. 163 – 174.
- [16] Bosc, N. (1992). "A time-domain panel method for analysis of foil in unsteady motion as oscillating propellers," *Eleventh Australian Fluid Mechanics Conference*, Holart, December, 1992, 4 p.
- [17] Brebbia, C.A. and Dominguez, J. (1989). *Boundary elements, An introductory course*, Computational Mechanics Publications, 293 p.
- [18] Brebbia, C.A. and Walker, S. (1978). "Introduction to boundary element methods," *Recent advances in boundary element methods*, ed. C.A. Brebbia, Pentech Press, Plymouth, London, pp. 1 – 43.
- [19] Bristow, D. R. (1980). "Development of panel methods for subsonic analysis and design," NASA CR-3234, 78 p.
- [20] Bristow, D. R. and Hawk, J. D. "Subsonic panel method for designing wing surfaces from pressure distributions," NASA CR-3713, July 1983, 52 p.
- [21] Chopra, M.G. (1974). "Hydromechanics of lunata-tail swimming propulsion. part 1," *J. Fluid Mech.*, Vol. 64, Part 2, pp. 375 – 391.
- [22] Chopra, M.G. and Kambe, T.K. (1977). "Hydromechanics of lunata-tail swimming propulsion. part 2," *J. Fluid Mech.*, Vol. 79, Part 1, pp. 46 – 69.
- [23] Clark, R.W. (1985). "A new iterative matrix solution procedure for three-dimensional panel methods," *Independent Research and Development of the McDonnell Douglas Co.*, 6 p.
- [24] Dane, A. (1992) "Wingships," *Popular Mechanics*, May, pp. 35 – 38.
- [25] Davies, D.E. (1965). "Calculation of unsteady generalised airforces on a thin wing oscillating harmonically in subsonic flow," *Aeronautical Research Council, R. & M.*, No. 3409, 52 p.

- [26] Falkner, V.M. (1943). "The calculation of aerodynamic load on surface of any shape," *Aeronautical Research Council, R. & M.*, No. 1910, 20 p.
- [27] Freund, R., Golub, G. and Nachtigal N. (1991). "Iterative solution of linear systems," *Acta Numerica*, 1991, pp. 57 – 100
- [28] Frydenlund, O. and Kerwin, J.E. (1977). "The development of numerical methods for the computation of unsteady propeller forces," *Norwegian Maritime Research*, No. 2, pp. 17 – 28.
- [29] Giesing, J.P. (1968). "Nonlinear two-dimensional unsteady potential flow with lift," *J. Aircraft*, Vol. 5, No. 2., pp. 135 – 143.
- [30] Glauert, H. (1926). *The elements of aerofoil and airscrew theory*, Second edition, reissued in 1983, Cambridge University Press, London, 299 p.
- [31] Hess, J.L. (1975). "Review of integral-equation techniques for solving potential-flow problems with emphases on the surface-source method," *Computer Methods in Applied Mechanics and Engineering*, Vol. 5. pp. 145 – 196.
- [32] Hess, J.L. and Smith, A.M.O. (1967). "Calculation of potential flow about arbitrary bodies," *Progress in Aeronautical Sciences (ed. D. Küchenmann)*, Vol. 8, Pergamon Press, pp. 1 – 139.
- [33] Hess, J.L. and Valarezo, W.O. (1985). "Calculation of steady flow about propellers by means of surface panel method," *Research and Technology Douglas Aircraft Company, Long Beach, Ca.*, 8 p.
- [34] Hoshino, T. (1989). "Hydrodynamic analysis of propellers in steady flow using a surface panel method," *Read at the Spring Meeting of the Society of Naval Architects of Japan*, May, pp. 55 – 70.
- [35] Hsiao, G.C. and Porter, J.F. (1989). "A coupling of BEM and FEM for the viscous flow problem," *Viscous/Separated Flows, Proceedings of the International Symposium on Boundary Element Methods: Advances in Solid and Fluid Mechanics*, East Hartford, Connecticut, pp. 105 – 111.
- [36] Hsin, C-Y, Kerwin, J.E. and Kinnas, S.A. (1991). "A panel method for the analysis of the flow around highly skewed propellers," *The propellers/shafting 91' symposium, SNAME*, Virginia Beach, Virginia, pp. 11.1 – 11.13.
- [37] Hunt, B. (1980). "The mathematical basis and numerical principles of the boundary integral method for incompressible potential flow over 3-d aerodynamic configuration," *Numerical Method in Applied Fluid Dynamics (ed. B. Hunt)*, Academic Press, pp. 49 – 135
- [38] Jennings, A. (1977). *Matrix computation for engineers and scientists*, John Wiley & Sons, 329 p.

- [39] Johnson, F. T., James, R.M., Bussolletti, J.E. and Woo, A.C. (1982). "A transonic rectangular grid embedded panel method," *AIAA-82-0953*, June, 20 p.
- [40] Johnson, F. T. (1980). "A general panel method for the analysis and design of arbitrary configurations in incompressible flows," *NASA CR-3079*, May, 20 p.
- [41] Johnson, O., executive editor, Dailey, V., associate editor, Reed, A., Bruno, W.E., Lyoris, D.M., contributing editors, Lee, F.II., and Scalza, R., manuscript editors. (1989). *The 1989 Almanac*, 976 p.
- [42] Johnston, G.W., Zingg, D.W. and Cameron, P.G. (1985). "An unsteady, non-linear, finite amplitude analysis procedure for hydrodynamic sections," Defence Research Establishment Atlantic, Contract No. 6AE977077 - 4 - 3832, 79 p.
- [43] Katz, J. and Weihs, D. (1989). "The effect of chordwise flexibility on the lift of a rapidly accelerated airfoil," *Aeronautical Quarterly*, February, pp. 360-369.
- [44] Katz J. and Plotkin A. (1991). *Low-speed aerodynamics*, McGraw-Hill, New York, 1991, 632 p.
- [45] Kerwin, J.E. and Lee, C.S. (1978). "Predictions of steady and unsteady marine propeller performance by numerical lifting-surface theory," *SNAME Transactions*, Vol. 86, pp. 218 - 253.
- [46] Kerwin, J.E., Kinnas, S.A. and Lee, J-T. (1987). "A surface panel method for the hydrodynamic analysis of ducted propellers," *SNAME Transactions*, Vol. 95, pp. 93 - 122.
- [47] Kinnas, S.A. and Hsin, C.Y. (1992). "Boundary element method for the analysis of the unsteady flow around extreme propeller geometries," *AIAA Journal*, Vol. 30, No. 3, pp. 688 - 696.
- [48] Kinnas, S.A. (1992). "A general theory for the coupling between thickness and loading for wings and propellers," *J. of Ship Research*, Vol. 36, No. 1 pp. 59 - 68.
- [49] Koyama, K., Kakugawa, A. and Okamoto, M. (1986). "Experiment investigation of flow around marine propeller theory," *16th Symposium on Naval Hydrodynamics*, Berkeley, July, pp. 289 - 309.
- [50] Lai, P.S.K. (1990) "Oscillating foil propulsion," *PhD thesis*, University of Glasgow, 410 p.
- [51] Lan, C.E. (1979). "The unsteady quasi-vortex-lattice method with applications to animal propulsion," *J. Fluid Mech.*, Vol. 93, Part 4, pp. 747 - 756.
- [52] Lan, C.E. (1974). "A quasi-vortex-lattice method in thin wing theory," *J. Aircraft*, Vol. 11, No. 9, pp. 518 - 527.

- [53] Lee, C.-S., Biskoup, B.A., Dong, S.-T., Glover, E.J., Grossi, L., Ikchata, M., Karacht, A., Peterson, F.B. (1990). "Propulsor Committee Report", *ITTC (International Towing Tank Conference)*, pp. 106 – 160.
- [54] Lighthill, M. J. (1986). *An Informal Introduction to Theoretical Fluid Mechanics*, Clarendon Press, Oxford, 260 p.
- [55] Lighthill, M.J. (1969). "Hydrodynamics of aquatic animal propulsion," *Annual Rev. Fluid Mech.*, Vol. 1, pp. 413 – 446.
- [56] Liu, P. (1991). "Three dimensional oscillating foil propulsion," *M. Eng. thesis*, Memorial University of Newfoundland, St. John's, Newfoundland, Canada, 157 p.
- [57] Liu, P. and Bose N. (1993). "Propulsive performance of three naturally-occurring oscillating propeller planforms," *Ocean Engineering*, Vol. 20, No. 1, pp. 57 – 75.
- [58] Liu, P. and Bose N. (1991). "Propulsion from an oscillating, finite-span foil of arbitrary planform," *Proceedings of the Marine Dynamics Conference 1991*, St. John's, Newfoundland, Canada, pp. 59 – 66.
- [59] Maskew, B. (1987). "Program VSAERO theory document," NASA CR-4023, September, 100 p.
- [60] Maskew, B. (1982). "Prediction of subsonic aerodynamic characteristics: A case for low-order panel methods," *J. Aircraft*, Vol. 19, No. 2, pp. 157 – 163.
- [61] Matthews, P., McCarthy, M.D., Young, M. and McWhirter, editors. (1993). *The Guinness book of records*, Bantam Books, New York, 847 p.
- [62] Milne-Thomson, L. M. (1958). *Theoretical Aerodynamics*, Dover Publications, Inc., 430 p.
- [63] Moran, J. (1984). *Theoretical and computational aerodynamics*, John Wiley & Sons, New York, 464 p.
- [64] Morino, L. (1989). "A unified approach for potential and viscous flows in fixed-wing and rotary aerodynamics," Viscous/Separated Flows, *Proceedings of the International Symposium on Boundary Element Methods: Advances in Solid and Fluid Mechanics*, East Hartford, Connecticut, pp. 68 – 74.
- [65] Morino, L. and Kuo, C.C. (1974). "Subsonic potential aerodynamics for complex configurations: A general theory," *AIAA Journal*, Vol. 12, No. 2, 1974, pp. 191 – 197.
- [66] Mracek, C.P. and Mook, D. (1988). "Numerical simulation of three-dimensional lifting flows by a vortex panel method," *AIAA Paper*, No. 88-4336, pp. 55 – 62.

- [67] Multhopp, H. (1950). "Methods for calculating the lift distribution of wings (subsonic lifting-surface theory)," *Aeronautical Research Council, R. & M.*, No. 2884, 96 p.
- [68] Newman, J.N. and Wu, T.Y. (1974). "Hydromechanical aspect of fish swimming," *Swimming and Flying in Nature*, vol. II, ed. T.Y. Wu, J. Brokaw, and C. Brennen, Plenum Press, pp. 615 – 634
- [69] O'Brien, J.L. and Geers, T.L. (1989). "Direct vs. indirect boundary element methods," *Elasticity, Proceedings of the International Symposium on Boundary Element Methods: Advances in Solid and Fluid Mechanics*, East Hartford, Connecticut, pp. 169 – 178.
- [70] Pankhurst, R.C. (1944). "A method for the rapid evaluation of Glauert's expressions for the angle of zero lift and the moment at zero lift," *Ministry of Aircraft Production, Aeronautical Research Committee, R&M*, 8p.
- [71] Patterson, M.T., Wu, J.C. and Wang, C.M. (1989). "Boundary element methods for the Navier-Stokes equations," *Viscous/Separated Flows, Proceedings of the International Symposium on Boundary Element Methods: Advances in Solid and Fluid Mechanics*, East Hartford, Connecticut, pp. 124 – 130.
- [72] Potze, W. (1986). "On optimum sculling propulsion," *Journal of Ship Research*, Vol. 30, No. 4, pp. 221 – 241.
- [73] Pyo, S. and Kinnas, S. (1994). "The flow adapted grid (FLAG) applied the analysis of propeller tip flows," *Propellers/Shafting '94 Symposium, The Society of Naval Architects and Marine Engineers*, Sept. 20-21, 10 p.
- [74] Richardson, J.R. (1955). "A method for calculating the lifting forces on wings (unsteady subsonic and supersonic lifting-surface theory)," *Aeronautical Research Council, Technical Report, R.& M.*, No. 3157, London, 30 p.
- [75] Richson, T.F. and Katz, J. (1993). "Unsteady panel method for flows with multiple bodies and various paths," *31st Aerospace Sciences Meeting & Exhibit*, Reno, NV., January, 9 p.
- [76] Rokhsaz, K., Selberg, B.P. and Eversman, W. (1989). "A vortex panel method for the solution of incompressible unsteady flow," *AIAA Paper*, No. 89-1284, 1989, pp. 1094 – 1104.
- [77] Rubbert, P.E. and Saaris, G.R. (1967). "A general method for determining the aerodynamic characteristics of fan-in-wing configurations," *Technical Report, USA AVLABS*, 15 p.
- [78] Rubbert, P.E. and Saaris, G.R. (1972). "Review and evaluation of a three-dimensional lifting potential flow analysis method for arbitrary configurations," *AIAA Paper*, No. 72-188, 15 p.

- [79] Ruiz-Calavera, L.P. and Geissler, W. (1988). "Thickness effects in the unsteady aerodynamics of interfering lifting surfaces." *ICAS-88-6.3.2.*, pp. 514 – 523.
- [80] Schlichting, H. Translated by Kestin, J. (1968). *Boundary layer theory*, 7th ed., McGraw-Hill, New York, 817 p.
- [81] Shaw, R.P. (1978). "Coupling boundary integral methods to 'other' numerical techniques," *Recent advances in boundary element methods*, ed. C.A. Brebbia, Pentech Press, Plymouth, London, pp. 137 – 144.
- [82] Simmons, G.F. (1985). *Calculus with analytical geometry*, McGraw-Hill, 950 p.
- [83] Theodorsen, T. (1935). "General theory of aerodynamic instability and the mechanism of flutter," *NACA Report*, No. 496, Washington D.C., pp. 413 – 433.
- [84] Thwaites, B. (1960). *Incompressible aerodynamics*, Dover Publications, Inc., 636 p.
- [85] Triantafyllou M. and Triantafyllou G. (1995). "An efficient swimming machine," *Scientific American*, March 1995, pp. 64 – 70.
- [86] Valarezo, W.O. and Liebeck, R.H. (1988). "Three dimensional calculation of windmill surface pressures," *AIAA-8-2533-CP*, pp. 168 – 173
- [87] van Dam, C.P. (1986). "Drag-reduction characteristics of aft-swept wing tips," *AIAA Paper 86-1824*, pp. 327 – 338.
- [88] van Dam, C.P. (1987). "Efficiency characteristics of crescent-shaped wings and caudal fins," *Nature*, Vol. 325, January 29, pp. 435 – 437.
- [89] van Manen, J.D. Jr. (1973). "Non-conventional propulsion devices," *International Shipbuilding Progress*, Vol. 20, No. 226, pp. 173 – 193.
- [90] von Kármán T. and Sears, W.R. (1938). "Airfoil theory for non-uniform motion," *J. of the Aeronautical Sciences*, Vol. 5, No. 10, p379 – p390.
- [91] von Kármán, T. and Burgers, J.M. (1935). "General aerodynamic theory, perfect fluids," *Aerodynamic theory*, Vol. II, 1976 edition, editor-in-chief Durand, W.F., Peter Smith Publisher, Inc., Gloucester, Mass., 498 p.
- [92] von Mises, R. (1945). *Theory of Flight*, Dover Publications, Inc. 1959, 629 p.
- [93] Watkins, C.E., Runyan, H.L. and Woolston, D.S. (1955). "On the kernel function of the integral equation relating the lift and downwash distributions of oscillating finite wings in subsonic flow," *National Advisory Committee for Aeronautics*, Report No. 1234, 16 p.
- [94] Watts, G.A. and Juang, J.C. (1989). "Triscent flow separation at high-angle-of-attack," *Viscous/Separated Flows. Proceedings of the International Symposium on Boundary Element Methods: Advances in Solid and Fluid Mechanics*, East Harford, Connecticut, pp. 112 – 118.

- [95] Wu, J.C. (1989). "Linkage between potential and viscous flows," *Viscous/Separated Flows, Proceedings of the International Symposium on Boundary Element Methods: Advances in Solid and Fluid Mechanics*, East Harford, Connecticut, pp. 75 – 86.
- [96] Wu, T.Y. (1971). "Hydromechanics of swimming propulsion. Part 1. Swimming of a two-dimensional flexible plate at variable forward speeds in an inviscid fluid," *J. Fluid Mech.* Vol. 46, part 2, pp. 337 – 355.
- [97] Wu, T.Y. (1971). "Hydromechanics of swimming propulsion. Part 2. Some optimum shape problems," *J. Fluid Mech.* Vol. 46, part 3, pp. 521 – 544.
- [98] Yamaguchi, H. (1992). "Hydrodynamic design of an oscillating foil propeller," *National Research Council Canada, IMD Report, LM-1992-19*, 18 p.
- [99] Yang, Y. and Xu, M. (1980). *Mathematical physics & special functions*, in Chinese, Defence Industry Publishing Services, Beijing, 383 p.
- [100] Yen, A., Mook, D.T. and Nayfeh, A.H. (1981). "A continuous- vorticity panel method for lifting surfaces," *AIAA Paper*, No. 81-1985, 10 p.
- [101] Youngren, H. H., Bouchard, E. E., Coppersmith, R. M., and Miranda, L. R. (1983). "Comparison of panel method formulations and its influence on the development of QUADPAN, an advance low-order method," *AIAA Paper*, No. 83-1827, 13 p.

# Appendix A

## Determination of doublet/source coefficient matrices

Reliability and accuracy of this method depend very much on how to program the related subroutines. Understanding the theory, making a mathematical model were only a part of the whole work. There were also many things to do with the programming. For engineering applications, the most important thing is to obtain the correct results.

As it was discussed in Chapter 3, Newman's (1986) formulation is for the panel based coordinates, for a simple mathematical formulation. To transfer inertia frame coordinates to the panel local coordinates, a Fortran subroutine called G12Lo.INC was written. <sup>1</sup> To save the DRAM, this subroutine did not declare any array. COMMON blocks, in WATCOM F77/386, though they have a fast data transfer rate, were not used for any array because they did not allow a program to declare any dynamic array.

The subroutine G12Lo yields the transferred panel local coordinates, the central point of a panel and some other measurements for velocity calculation. Figure (A.1) shows the geometry and the legends.

---

<sup>1</sup>The "INC" file extension for the OSFBEM was for 'included' subroutines. These subroutines were separated from the main program for a better structure and readability.

Panel no.	Corner Point 1	Corner Point 2	Corner Point 3	Corner Point 4
panel 1.	(0, 1, 0)	(0, -.5, .866)	(1, 0, 0)	(0, 1, 0)
panel 2.	(0, -.5, .866)	(0, -.5, -.866)	(1, 0, 0)	(0, -.5, .866)
panel 3.	(0, -.5, -.866)	(0, 1, 0)	(1, 0, 0)	(0, -.5, -.866)
panel 4.	(0, 1, 0)	(-1, 0, 0)	(0, -.5, .866)	(0, 1, 0)
panel 5.	(0, -.5, .866)	(-1, 0, 0)	(0, -.5, -.866)	(0, -.5, .866)
panel 6.	(0, -.5, -.866)	(-1, 0, 0)	(0, 1, 0)	(0, -.5, -.866)

Table A.1: Offsets of a 3-D body with 5 faces and six corner points.

Twelve values of the coordinate of four corner points on the world frame were inputted (see the subroutine below). This subroutine also take a triangle panel, in which case, coordinate of the fourth corner point are the same as that of the first point. It was noted that for triangle panels, the centroid of the panel cannot be evaluated by the way as it did for the quadrilateral panel or a numerical error would occur. The theory is simple but it is easy to be ignored.

At the early stage of the development of OSFBEM, it was noted that it was very important to obtain the correct doublet and source coefficient matrices. The proper values of these coefficient were hard to find for a verification. These could be very helpful to beginners who are doing a similar study. This appendix intended to serve for this purpose.

To verify the obtained doublet and source coefficient matrices, a 3-D body with six corner points and five equilateral triangle faces was used. The coordinates of the six panels are as follows:

The order of these six panels was arbitrary. A sample Fortran program is attached to this Appendix and the results are as follows:

#### Doublet coefficient Matrix

```

1.00000000  0.28124517  0.28125706  0.15207383  0.14271028  0.14271356
0.28125054  1.00000000  0.28125051  0.14271171  0.15207548  0.14271171
0.28125706  0.28124517  1.00000000  0.14271356  0.14271028  0.15207383

```

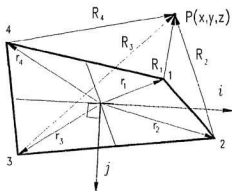


Figure A.1: Schematic diagram for coordinate transformation from the global frame to the panel local frame.

```

0.15207382  0.14271030  0.14271358  1.00000000  0.28124517  0.28125709
0.14271171  0.15207546  0.14271173  0.28125054  1.00000000  0.28125054
0.14271356  0.14271031  0.15207385  0.28125709  0.28124517  1.00000000

```

#### Source coefficient Matrix

```

-0.54000479 -0.23351721 -0.23352423 -0.21327470 -0.16198219 -0.16198614
-0.23352198 -0.54000056 -0.23352195 -0.16198525 -0.21327181 -0.16198523
-0.23352425 -0.23351724 -0.54000473 -0.16198614 -0.16198219 -0.21327470
-0.21327466 -0.16198222 -0.16198613 -0.54000473 -0.23351720 -0.23352422
-0.16198525 -0.21327186 -0.16198522 -0.23352197 -0.54000050 -0.23352197
-0.16198614 -0.16198221 -0.21327466 -0.23352422 -0.23351720 -0.54000473

```

#### Area A

```

0.96823448  0.96821743  0.96823448  0.96823448  0.96821743  0.96823448

```

The sample main program to find the matrices along with subroutine 'coeffphi' and 'gl2lo' are listed below. It is noted that a good programming practice is to use the dynamic array allocation, if the compiler has this option. A huge amount of time will be saved in creating the executable file frequently.

```

PROGRAM F_Matrix

IMPLICIT REAL*4 (A-H,O-Z)

      DIMENSION W1CornrB(6,12),CornerLo(6,12),
      &           W1ContrB(6,12),uk(6,3),ui(6,3),uj(6,3),area(6)
      DIMENSION SoMatrix(6,6)
      DIMENSION DoMatrix(6,6)

data ((W1CornrB(i,j),j=1,12),i=1,6)/0.,1.,0.,0.,-.5.,.866,
&     1.,0.,0.,0.,1.,0.,0.,-.5.,.866,0.,-.5.,-.866,1.,0.,0.,
&     0.,-.5.,.866,0.,-.5.,-.866,0.,1.,0.,1.,0.,0.,0.,-.5.,-.866,
&     0.,1.,0.,-1.,0.,0.,0.,-.5.,.866,0.,1.,0.,0.,-.5.,.866,
&     -1.,0.,0.,0.,-.5.,-.866,0.,-.5.,.866,0.,-.5.,-.866,
&     -1.,0.,0.,0.,1.,0.,0.,-.5.,-.866/

JobOut1=12
OPEN(JobOut1, file='ppppp.out', status='unknown')

WTPBody=6
DO i=1,WTPBody

      x1=W1CornrB(i,1)
      x2=W1CornrB(i,4)
      x3=W1CornrB(i,7)
      x4=W1CornrB(i,10)

      y1=W1CornrB(i,2)
      y2=W1CornrB(i,5)
      y3=W1CornrB(i,8)
      y4=W1CornrB(i,11)

      z1=W1CornrB(i,3)
      z2=W1CornrB(i,6)
      z3=W1CornrB(i,9)
      z4=W1CornrB(i,12)

CALL SL2LD(x1,x2,x3,x4,y1,y2,y3,y4,z1,z2,z3,z4,a,cs,cy,cz,
&         ukx,uky,ukz,uix,uiy,uiz,ujx,ujy,ujz,ChlaLng,
&         SpHaLng,Side2DJ,Side2DI)

      CornerLo(i,1)=x1
      CornerLo(i,4)=x2
      CornerLo(i,7)=x3
      CornerLo(i,10)=x4

```

```

CornerLo(i,2)=y1
CornerLo(i,5)=y2
CornerLo(i,8)=y3
CornerLo(i,11)=y4

CornerLo(i,3)=x1
CornerLo(i,6)=x2
CornerLo(i,9)=x3
CornerLo(i,12)=x4

area(i)=a

W1ContrB(i,1)=cx
W1ContrB(i,2)=cy
W1ContrB(i,3)=cz

uk(i,1)=ukx
uk(i,2)=uky
uk(i,3)=ukz

uj(i,1)=ujx
uj(i,2)=ujy
uj(i,3)=ujz

ui(i,1)=uix
ui(i,2)=uiy
ui(i,3)=uiz

END DO

WRITE (*,*) 'Finished transformation of coordinates'

WRITE (JobOut1,*) 'Finished transformation of coordinates'

DO i=1,NTPBody
DO j=1,NTPBody

cx=W1ContrB(j,1)
cy=W1ContrB(j,2)
qx=W1ContrB(i,1)
qy=W1ContrB(i,2)
cz=W1ContrB(j,3)
qz=W1ContrB(i,3)

rx=qx-cx ! (control point)-panel, initial setting
ry=qy-cy

```

```

rz=rq-cz

xw=rz*xi(j,1)+ry*xi(j,2)+rz*xi(j,3) ! Find the relative x,y, and
yw=rz*xj(j,1)+ry*xj(j,2)+rz*xj(j,3) ! z to panel local coordinates
zw=rz*xk(j,1)+ry*xk(j,2)+rz*xk(j,3)

* write(JobOut1,*) 'Relative coordinates x,y,z',x,y,z

x1=CornerLo(j,1)
x2=CornerLo(j,4)
x3=CornerLo(j,7)
x4=CornerLo(j,10)

y1=CornerLo(j,2)
y2=CornerLo(j,5)
y3=CornerLo(j,8)
y4=CornerLo(j,11)

z1=CornerLo(j,3)
z2=CornerLo(j,6)
z3=CornerLo(j,9)
z4=CornerLo(j,12)

CALL coeffphi(x1,x2,x3,x4,y1,y2,y3,y4,x,y,z,
A
i,j,FiDoublet,FiSource)

DoMatrix(i,j)=2.*FiDoublet
SoMatrix(i,j)=2.*FiSource

WRITE(JobOut4) FiSource
WRITE(JobOut5) FiDoublet

END DO
END DO

WRITE(JobOut1,*)'Finish Doublet/Source matrices determination'

write(JobOut1,*)'Doublet coefficient Matrix'
DO I=1,NTPBody
write(JobOut1,'(GF12.B)') (DoMatrix(i,j),j=1,NTPBody)
END DO
write(JobOut1,*)
write(JobOut1,*)'Source coefficient Matrix'
DO I=1,NTPBody
write(JobOut1,'(GF12.B)') (SoMatrix(i,j),j=1,NTPBody)
END DO

```

```

write(JobOut1,*)'Area A'
write(JobOut1,'(6F12.8)') (area(i),i=1,NTPBdy)
close(JobOut1)
STOP
END
*
-----
*
SUBROUTINE GL2LO(x1,x2,x3,x4,y1,y2,y3,y4,z1,z2,z3,z4,a,cx,cy,
& cz,ukx,uky,ukz,uix,uiy,uiz,uix,uiz,uiz,uiz,ChMalng,
& SpMalng,Side2DJ,Side2DI)

IMPLICIT REAL*4 (A-H,O-Z)

*/ x1-4, y1-4 and z1-4 are the global coordinates of the corner */
*/ points. X1-4 and y1-4 will be replaced by the new local */
*/ coordinate values. z1-4 should be about zeros. a is the area */
*/ of the panel. cx, cy and cz are the centroid ordinates of the */
*/ panel. ukx, uky and ukz are the components of the unit normal */
*/ vector to the panel or to the mean plane for twist panel. */

dxi=x3-x1 ! The x component of the first diagonal of the panel
dx2=x4-x2
dy1=y3-y1
dy2=y4-y2
dz1=z3-z1
dz2=z4-z2

crd_x=dy1*dz2-dy2*dz1 ! Vector CRD is cross product of d1 and d2
crd_y=dz2*dz1-dx1*dz2
crd_z=dx1*dy2-dx2*dy1

crd_mod=SQRT(crd_x*crd_x+crd_y*crd_y+crd_z*crd_z)

a=crd_mod/2. ! Area of the panel

ukx=crd_x/crd_mod ! The components of the unit normal vector UK
uky=crd_y/crd_mod
ukz=crd_z/crd_mod

sd1=SQRT((x2-x1)**2+(y2-y1)**2+(z2-z1)**2)
sd2=SQRT((x3-x2)**2+(y3-y2)**2+(z3-z2)**2)
sd3=SQRT((x4-x3)**2+(y4-y3)**2+(z4-z3)**2)
sd4=SQRT((x1-x4)**2+(y1-y4)**2+(z1-z4)**2)

```

```

IF (sd1.LT.0.000001) THEN
cx=(x2+x3+x4)/3. ! The centroid of the the (mean) panel
cy=(y2+y3+y4)/3.
cz=(z2+z3+z4)/3.
ELSE IF (sd2.LT.0.000001) THEN
cx=(x1+x3+x4)/3. ! The centroid of the (mean) panel
cy=(y1+y3+y4)/3.
cz=(z1+z3+z4)/3.
ELSE IF (sd3.LT.0.000001) THEN
cx=(x1+x2+x4)/3. ! The centroid of the (mean) panel
cy=(y1+y2+y4)/3.
cz=(z1+z2+z4)/3.
ELSE IF (sd4.LT.0.000001) THEN
cx=(x1+x3+x2)/3. ! The centroid of the (mean) panel
cy=(y1+y3+y2)/3.
cz=(z1+z3+z2)/3.
ELSE
cx=(x1+x2+x3+x4)/4. ! The centroid of the (mean) panel
cy=(y1+y2+y3+y4)/4.
cz=(z1+z2+z3+z4)/4.
END IF
vjx=(x3+x4)/2.-cx
vjy=(y3+y4)/2.-cy
vjz=(z3+z4)/2.-cz

vj=SQRT(vjx*vjx+vjy*vjy+vjz*vjz) ! Modulus of the middle point
! vector vj
ujx=vjx/vj ! Components of the unit vector Uj,
ujy=vjy/vj
ujz=vjz/vj

uix=ujy*ukx-uky*ujz ! Components of the unit vector Ui
uiy=ukx*ujz-ujx*ukz
uiz=ujx*uky-ukx*ujy

```

- The followings are the local quantities

```

rx1=x1-cx ! Components of the corner vectors based on cx,xy and cz.
rx2=x2-cx
rx3=x3-cx
rx4=x4-cx
ry1=y1-cy
ry2=y2-cy
ry3=y3-cy
ry4=y4-cy

```

```

r1=r1-cz
r2=r2-cz
r3=r3-cz
r4=r4-cz

x1=r1*ux+ry1*uy+rz1*uz ! X of corner vector projected on UI
x2=r2*ux+ry2*uy+rz2*uz
x3=r3*ux+ry3*uy+rz3*uz
x4=r4*ux+ry4*uy+rz4*uz

y1=r1*ujx+ry1*ujy+rz1*ujz
y2=r2*ujx+ry2*ujy+rz2*ujz
y3=r3*ujx+ry3*ujy+rz3*ujz
y4=r4*ujx+ry4*ujy+rz4*ujz

z1=r1*ukx+ry1*uky+rz1*ukz ! The skew of the panel at point I
z2=r2*ukx+ry2*uky+rz2*ukz
z3=r3*ukx+ry3*uky+rz3*ukz
z4=r4*ukx+ry4*uky+rz4*ukz

SpHaLgX=(x3+x4)/2.
SpHaLgY=(y3+y4)/2.
SpHaLgZ=(z3+z4)/2.

ChHaLgX=(x3+x2)/2.
ChHaLgY=(y3+y2)/2.
ChHaLgZ=(z3+z2)/2.

SpHaLg=SQR(SpHaLgX*SpHaLgX+SpHaLgY*SpHaLgY+
& SpHaLgZ*SpHaLgZ)

ChHaLg=SQR(ChHaLgX*ChHaLgX+ChHaLgY*ChHaLgY+
& ChHaLgZ*ChHaLgZ)

Side2D1=ABS(ChHaLgY)
Side2D1=ABS(ChHaLgX)

RETURN
END

*
-----
-
*
SUBROUTINE coeffphi(x1,x2,x3,x4,y1,y2,y3,y4,x,y,z,
& i,j,FIDoublet,FISource)

```

```

IMPLICIT REAL*4 (A-H,O-Z)

*/ This subroutine calculates the induced velocity potential at */
*/ point P(x,y,z) due to an infinite number of uniformly */
*/ distributed dipoles over a quadrilateral panel. Numerical */
*/ interpretation was used according to J. Newman's formulation */
*/ (Distributions of sources and normal dipoles over a */
*/ quadrilateral panel, Journal of Engineering Mathematics, 20, */
*/ 1966). Note: the sequence of the four corner points is in CCW; */
*/ so that the result need to add a negative sign. */
*/
*/

dx1=x2-x1 ! Precalculate values that will be used more then
dx2=x3-x2 ! one place to save the CPU time
dx3=x4-x3
dx4=x1-x4
dy1=y2-y1
dy2=y3-y2
dy3=y4-y3
dy4=y1-y4

sd1=SQRt(dx1*ds1+dy1*dy1)
sd2=SQRt(dx2*ds2+dy2*dy2)
sd3=SQRt(dx3*ds3+dy3*dy3)
sd4=SQRt(dx4*ds4+dy4*dy4)

r1=sqrt((x-x1)*(x-x1)+(y-y1)*(y-y1)+z*z)
r2=sqrt((x-x2)*(x-x2)+(y-y2)*(y-y2)+z*z)
r3=sqrt((x-x3)*(x-x3)+(y-y3)*(y-y3)+z*z)
r4=sqrt((x-x4)*(x-x4)+(y-y4)*(y-y4)+z*z)

*BEGIN{Block 1} Doublet calculation
IF (i.e.j) THEN
  FIDoublet=0.5
ELSE IF (ABS(z).LT.0.000001) THEN
  FIDoublet=0.0
ELSE
  xz1=(x-x1)*(x-x1)+z*z
  xz2=(x-x2)*(x-x2)+z*z
  xz3=(x-x3)*(x-x3)+z*z
  xz4=(x-x4)*(x-x4)+z*z

  xy1=(x-x1)*(y-y1)
  xy2=(x-x2)*(y-y2)
  xy3=(x-x3)*(y-y3)
  xy4=(x-x4)*(y-y4)

```

```
IF (sd1.le.0.000001) THEN
Dt1=0.
ELSE
s11=dy1*xz1-dx1*xy1
c11=r1*x*dx1
s12=dy1*xz2-dx1*xy2
c12=r2*x*dx1
ss1=s11*c12-s12*c11
cc1=c11*c12+s11*s12
Dt1=atan2(ss1,cc1)
END IF
```

```
IF (sd2.le.0.000001) THEN
Dt2=0.
ELSE
s21=dy2*xz2-dx2*xy2
c21=r2*x*dx2
s22=dy2*xz3-dx2*xy3
c22=r3*x*dx2
ss2=s21*c22-s22*c21
cc2=c21*c22+s21*s22
Dt2=atan2(ss2,cc2)
END IF
```

```
IF (sd3.le.0.000001) THEN
Dt3=0.
ELSE
s31=dy3*xz3-dx3*xy3
c31=r3*x*dx3
s32=dy3*xz4-dx3*xy4
c32=r4*x*dx3
ss3=s31*c32-s32*c31
cc3=c31*c32+s31*s32
Dt3=atan2(ss3,cc3)
END IF
```

```
IF (sd4.le.0.000001) THEN
Dt4=0.
ELSE
s41=dy4*xz4-dx4*xy4
c41=r4*x*dx4
s42=dy4*xz1-dx4*xy1
c42=r1*x*dx4
ss4=s41*c42-s42*c41
cc4=c41*c42+s41*s42
```

```

Dt4=atan2(ss4,cc4)
END IF
FiDoublet=(Dt1+Dt2+Dt3+Dt4)/12.56637061 ! Add a '-' sign for CCW

ENDIF
*END(Block 1) Doublet Calculation *****
-----
*BEGIN(Block 2) Source Calculation *****

  IF (sd1.le .0.000001) THEN
    St1=0.
  ELSE
    St1=((x-x1)*dy1-(y-y1)*dx1)/sd1*LOG((r1+r2+sd1)/(r1+r2-sd1))
  END IF

  IF (sd2.le .0.000001) THEN
    St2=0.
  ELSE
    St2=((x-x2)*dy2-(y-y2)*dx2)/sd2*LOG((r2+r3+sd2)/(r2+r3-sd2))
  END IF

  IF (sd3.le .0.000001) THEN
    St3=0.
  ELSE
    St3=((x-x3)*dy3-(y-y3)*dx3)/sd3*LOG((r3+r4+sd3)/(r3+r4-sd3))
  END IF

  IF (sd4.le .0.000001) THEN
    St4=0.
  ELSE
    St4=((x-x4)*dy4-(y-y4)*dx4)/sd4*LOG((r4+r1+sd4)/(r4+r1-sd4))
  END IF

  FiSource=(St1+St2+St3+St4)/12.56637061-z*FiDoublet
*END(Block 2) Source Calculation *****

END

```

## **Appendix B**

### **Graphical presentation of some oscillating propellers in motion**

This Appendix lists a number of graphics obtained numerically for different oscillating foil planforms with different parameters. The first series of graphics described the fin whale flukes with 19 combinations of deflexion equations; the second list is for a rectangular half elastic foil in terms of the chordwise deflexion phase angle.

#### **B-A Instantaneous positions and wake paths of a fin whale's flukes**

Six chordwise and three spanwise deflexion equations were used. Including the zero deflexion in both directions, there are 19 combinations in the selection of equations.

It is noted that C1 stands for the chordwise deflexion equation number one and S1 for the first spanwise function, and so on in ascending order of the exponent  $c$ .

As it was mentioned before, the time step sizes used in the graphic presentation is much larger than the actual values that were inputted to the computer program, to keep the validity of the steady Kutta condition for a reliable prediction.

In these figures, foil swimming velocity towards the negative x-direction, and z-axis points upward. The values of the view point indicate the directional vector pointing from the origin to the viewer.

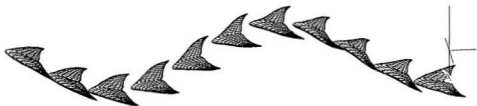


Figure B.1: Deflexion of a fin whale's flukes by a combination of  $C0$  and  $S0$ , where  $C0$  and  $S0$  stand for a rigid planform (no deflexion). View point is at  $(-1, -10, 3)$ .



Figure B.2: Deflexion of a fin whale's flukes by a combination of  $C1$  and  $S1$ , where  $C1$  and  $S1$  stand for  $\epsilon = 1.5$  and  $c = 0$  in eqn. 7.1 and eqn. 7.3, respectively. View point is at  $(-1, -10, -3)$ .



Figure B.3: Deflexion of a fin whale's flukes by a combination of  $C1$  and  $S2$ , where  $C1$  and  $S2$  stand for  $\epsilon = 1.5$  and  $\epsilon = 0.5$  in eqn. 7.1 and eqn. 7.3, respectively. View point is at  $(-1, -10, 3)$ .



Figure B.4: Deflexion of a fin whale's flukes by a combination of  $C1$  and  $S3$ , where  $C1$  and  $S3$  stand for  $\epsilon = 1.5$  and  $\epsilon = 1$  in eqn. 7.1 and eqn. 7.3, respectively. View point is at  $(-1, -10, -3)$ .



Figure B.5: Deflexion of a fin whale's flukes by a combination of  $C2$  and  $S1$ , where  $C2$  and  $S1$  stand for  $\epsilon = 2$  and  $\epsilon = 0$  in eqn. 7.1 and eqn. 7.3, respectively. View point is at  $(-1, -10, -3)$ .



Figure B.6: Deflexion of a fin whale's flukes by a combination of  $C2$  and  $S2$ , where  $C2$  and  $S2$  stand for  $\epsilon = 2$  and  $\epsilon = 0.5$  in eqn. 7.1 and eqn. 7.3, respectively. View point is at  $(-1, -10, -3)$ .



Figure B.7: Deflexion of a fin whale's flukes by a combination of  $C2$  and  $S3$ , where  $C2$  and  $S3$  stand for  $\epsilon = 2$  and  $\epsilon = 1$  in eqn. 7.1 and eqn. 7.3, respectively. View point is at  $(-1, -10, -3)$ .



Figure B.8: Deflexion of a fin whale's flukes by a combination of  $C3$  and  $S1$ , where  $C3$  and  $S1$  stand for  $\epsilon = 2.5$  and  $\epsilon = 0$  in eqn. 7.1 and eqn. 7.3, respectively. View point is at  $(-1, -10, -3)$ .



Figure B.9: Deflexion of a fin whale's flukes by a combination of  $C3$  and  $S2$ , where  $C3$  and  $S2$  stand for  $\epsilon = 2.5$  and  $\epsilon = 0.5$  in eqn. 7.1 and eqn. 7.3, respectively. View point is at  $(-1, -10, -3)$ .



Figure B.10: Deflexion of a fin whale's flukes by a combination of  $C3$  and  $S3$ , where  $C3$  and  $S3$  stand for  $\epsilon = 2.5$  and  $\epsilon = 1$  in eqn. 7.1 and eqn. 7.3, respectively. View point is at  $(-1, -10, -3)$ .



Figure B.11: Deflexion of a fin whale's flukes by a combination of  $C4$  and  $S1$ , where  $C4$  and  $S1$  stand for  $\epsilon = 3$  and  $\epsilon = 0$  in eqn. 7.1 and eqn. 7.3, respectively. View point is at  $(-1, -10, 4)$ .



Figure B.12: Deflexion of a fin whale's flukes by a combination of  $C4$  and  $S2$ , where  $C4$  and  $S2$  stand for  $\epsilon = 3$  and  $\epsilon = 0.5$  in eqn. 7.1 and eqn. 7.3, respectively. View point is at  $(-1, -10, -4)$ .



Figure B.13: Deflexion of a fin whale's flukes by a combination of  $C4$  and  $S3$ , where  $C4$  and  $S3$  stand for  $\epsilon = 3$  and  $\epsilon = 1$  in eqn. 7.1 and eqn. 7.3, respectively. View point is at  $(-1, -10, 4)$ .



Figure B.14: Deflexion of a fin whale's flukes by a combination of  $C5$  and  $S1$ , where  $C5$  and  $S1$  stand for  $\epsilon = 3.5$  and  $\epsilon = 0$  in eqn. 7.1 and eqn. 7.3, respectively. View point is at  $(-1, -10, -4)$ .



Figure B.15: Deflexion of a fin whale's flukes by a combination of  $C5$  and  $S2$ , where  $C5$  and  $S2$  stand for  $\epsilon = 3.5$  and  $\epsilon = 0.5$  in eqn. 7.1 and eqn. 7.3, respectively. View point is at  $(-1, -10, 4)$ .



Figure B.16: Deflexion of a fin whale's flukes by a combination of  $C5$  and  $S3$ , where  $C5$  and  $S3$  stand for  $\epsilon = 3.5$  and  $\epsilon = 1$  in eqn. 7.1 and eqn. 7.3, respectively. View point is at  $(-1, -10, 3)$ .



Figure B.17: Deflexion of a fin whale's flukes by a combination of  $C6$  and  $S1$ , where  $C6$  and  $S1$  stand for  $\epsilon = 4$  and  $\epsilon = 0$  in eqn. 7.1 and eqn. 7.3, respectively. View point is at  $(-1, -10, -4)$ .



Figure B.18: Deflexion of a fin whale's flukes by a combination of  $C6$  and  $S2$ , where  $C6$  and  $S2$  stand for  $\epsilon = 4$  and  $\epsilon = 0.5$  in eqn. 7.1 and eqn. 7.3, respectively. View point is at  $(-1, -10, 4)$ .



Figure B.19: Deflexion of a fin whale's flukes by a combination of  $C6$  and  $S3$ , where  $C6$  and  $S3$  stand for  $c = 4$  and  $c = 1$  in eqn. 7.1 and eqn. 7.3, respectively. View point is at  $(-1, -10, -4)$ .

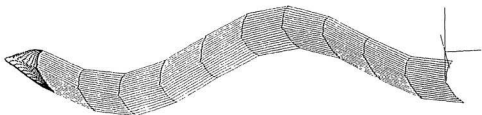


Figure B.20: Path of the flukes with their wake by a combination of  $C0$  and  $S0$ , where  $C0$  and  $S0$  stand for a rigid planform (no deflexion). View point is at  $(-1, -10, 4)$ .

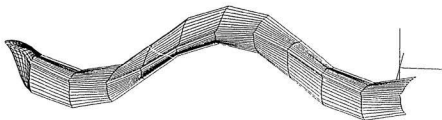


Figure B.21: Path of the flukes with their wake by a combination of  $C1$  and  $S1$ , where  $C1$  and  $S1$  stand for eqn. 7.1 and eqn. 7.3 at  $\epsilon = 1.5$  and  $\epsilon = 0$ , respectively. View point is at  $(-1, -10, -4)$ .



Figure B.22: Path of the flukes with their wake by a combination of  $C1$  and  $S2$ , where  $C1$  and  $S2$  stand for eqn. 7.1 and eqn. 7.3 at  $\epsilon = 1.5$  and  $\epsilon = 0.5$ , respectively. View point is at  $(-1, -10, 4)$ . The wake path plots for other combinations of equations are looked similar to this one so that they are omitted.

## B-B Variation of phase angle of chordwise deflexion

The following foil geometry and motion parameters were used for graphics in this section:

- Section thickness distribution is NACA 63A015.
- Span is 49 m and chord is 7 m and hence aspect ratio is  $At = 7$ .
- Spanwise deflexion is  $\delta_s = 0.0$ .
- Oscillating frequency is  $\omega = 1.3468$ .
- Equation of chordwise deflexion is  $(\delta_c)_i(2x - 1)^3$ .
- Deflexion starting  $x = 50\% \sim 100\%$  is referring to the local chord.
- The maximum deflexion factor is  $\delta_{co} = 0.2$ .
- Chordwise deflexion phase lag is  $-30^\circ$ .
- Heave amplitude factor is  $h_o = 0.7$ .
- Phase angle (pitch leading heave) is  $\Phi_{phase} = 104^\circ$ .
- Pitch amplitude is  $\alpha_o = 19.7^\circ$ .

Again, the actual time step size in the computations for efficiency and thrust is much smaller than shown.



Figure B.23: Instantaneous positions of a rectangular foil with a semichord deflexion at  $0^\circ$  phase lag. View point is at  $(0, -1, 0)$ .



Figure B.24: Instantaneous positions of a rectangular foil with a semichord deflexion at  $-20^\circ$  phase lag. View point is at  $(0, -1, 0)$ .



Figure B.25: Instantaneous positions of a rectangular foil with a semichord deflexion at  $-40^\circ$  phase lag. View point is at  $(0, -1, 0)$ .

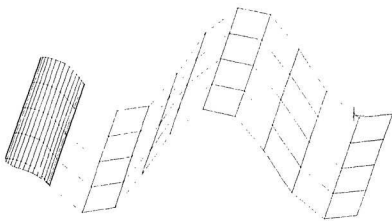


Figure B.26: Wake and path of a rectangular foil with a semichord deflexion at  $0^\circ$  phase lag. View point is at  $(1, -10, 3)$ .

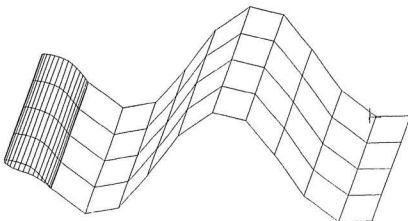


Figure B.27: Wake and path of a rectangular foil with a semichord deflexion at  $-20^\circ$  phase lag. View point is at  $(1, -10, 3)$ .

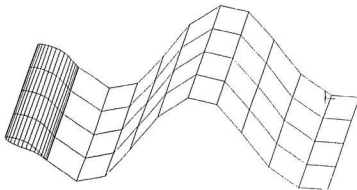


Figure B.28: Wake and path of a rectangular foil with a semichord deflexion at  $-40^\circ$  phase lag. View point is at  $(1, -10, 3)$ .

## B-C Variation of phase angle of spanwise deflexion

### B-C-1 Small change in phase angle for a rectangular foil

To simulate the phase lag of the spanwise deflexion of a rectangular oscillating propulsor, the following parameters were used:

- oscillating frequency  $\omega = 1.3468$  rad/sec.
- equation of spanwise deflexion being  $D_{span} [2 * (y/l)^2 \mp \frac{4}{3}(y/l)^3 + \frac{1}{3}(y/l)^4]$ .
- maximum deflexion factor  $\delta_{so} = 0.2$  and  $\delta_s = \delta_{so} * l$ , where  $l$  is the semispan length.
- sectional thickness distribution using NACA 63A015
- span  $S = 49$  m, chord  $C_r = 7$  m and aspect ratio  $AR = 7$ .
- chordwise deflexion amplitude  $\delta_c = 0.0$ , no deflexion.
- heave amplitude  $h_o = 0.7$ .
- phase angle (pitch leading heave) is  $\Phi_{phase} = 104^\circ$ .
- pitch amplitude is  $\alpha_o = 19.7^\circ$ .
- spanwise deflexion phase lag  $\Phi_s$  ranging from  $0^\circ \sim 50^\circ$ .
- number of total time step of 10.
- time step size  $\delta_t = T_{period}/8 = 2\pi/\omega/8 = 0.5831$  sec.

A number of total chordwise panels was taken as 20 and spanwise panels as 10.

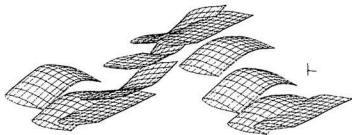


Figure B.29: Instantaneous positions of a rectangular foil with a spanwise deflexion at  $0^\circ$  phase lag. View point is at  $(1, -5, 0.5)$ .

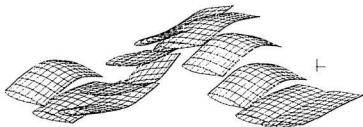


Figure B.30: Instantaneous positions of a rectangular foil with a spanwise deflexion at  $-30^\circ$  phase lag. View point is at  $(1, -5, 0.5)$ .

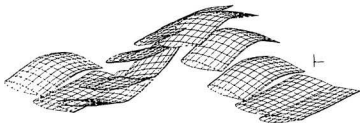


Figure B.31: Instantaneous positions of a rectangular foil with a spanwise deflexion at  $-50^\circ$  phase lag. View point is at  $(1, -5, 0.5)$ .

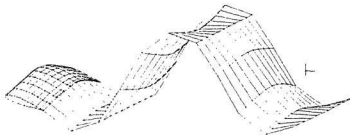


Figure B.32: Wake and path of a rectangular foil with a spanwise deflexion at  $0^\circ$  phase lag. View point is at  $(1, -5, 0.5)$ .

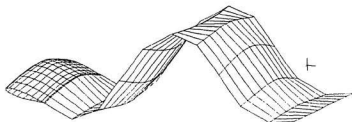


Figure B.33: Wake and path of a rectangular foil with a spanwise deflexion at  $-30^\circ$  phase lag. View point is at  $(1, -5, 0.5)$ .

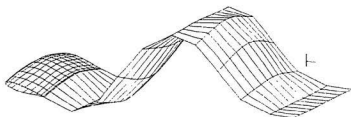


Figure B.34: Wake and path of a rectangular foil with a spanwise deflexion at  $-50^\circ$  phase lag. View point is at  $(1, -5, 0.5)$ .

### B-C-2 Large change in spanwise deflexion phase angle for a fin whale's flukes

To simulate the phase angle of the spanwise deflexion of a fin whale's flukes as an oscillating propulsor, the following parameters were used:

- oscillating frequency  $\omega = 0.2\pi$  rad/sec.
- equation of spanwise deflexion being  $D_{span}[2 * (y/l)^2 \mp \frac{4}{3}(y/l)^3 + \frac{1}{3}(y/l)^4]$ .
- maximum deflexion factor  $\delta_{so} = 0.1$  and  $\delta_s = \delta_{so} * l$ , where  $l$  is the semispan length.
- sectional thickness distribution being the same as that of a real fin whale's flukes.
- chordwise deflexion amplitude  $\delta_c = 0.0$ , no deflexion.
- heave amplitude  $h_o = 1.0$ .
- phase angle (pitch leading heave) is  $\Phi_{phase} = 90^\circ$ .
- pitch amplitude is  $\alpha_o = 20^\circ$ .
- spanwise deflexion phase lag  $\Phi_s$ , ranging from  $-180^\circ \sim 180^\circ$ .
- number of total time step of 10.
- time step size  $\delta_t = T_{period}/10 = 2\pi/\omega/10 = 1.0$  sec.

A number of total chordwise panels was taken as 20 and spanwise panels as 10.

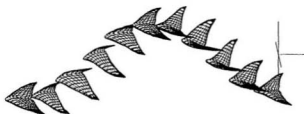


Figure B.35: Instantaneous positions of a fin whale's flukes with a spanwise deflexion at  $-180^\circ$  phase angle. View point is at  $(-1, -10, 4)$ .



Figure B.36: Instantaneous positions of a fin whale's flukes with a spanwise deflexion at  $-120^\circ$  phase angle. View point is at  $(-1, -10, 4)$ .



Figure B.37: Instantaneous positions of a fin whale's flukes with a spanwise deflexion at  $-60^\circ$  phase angle. View point is at  $(-1, -10, 4)$ .

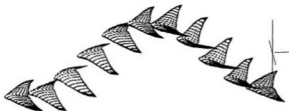


Figure B.38: Instantaneous positions of a fin whale's flukes with a spanwise deflexion at  $0^\circ$  phase angle. View point is at  $(-1, -10, 4)$ .



Figure B.39: Instantaneous positions of a fin whale's flukes with a spanwise deflexion at  $60^\circ$  phase angle. View point is at  $(-1, -10, 4)$ .

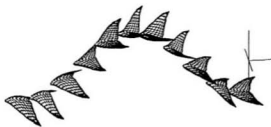


Figure B.40: Instantaneous positions of a fin whale's flukes with a spanwise deflexion at  $120^\circ$  phase angle. View point is at  $(-1, -10, 4)$ .

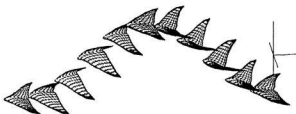


Figure B.41: Instantaneous positions of a fin whale's flukes with a spanwise deflexion at  $180^\circ$  phase angle. View point is at  $(-1, -10, 4)$ .



Figure B.42: Wake and its path of a fin whale's flukes with a spanwise deflexion at  $-180^\circ$  phase angle. View point is at  $(-1, -10, 4)$ .

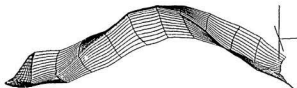


Figure B.43: Wake and its path of a fin whale's flukes with a spanwise deflexion at  $-120^\circ$  phase angle. View point is at  $(-1, -10, 4)$ .



Figure B.44: Wake and its path of a fin whale's flukes with a spanwise deflexion at  $-60^\circ$  phase angle. View point is at  $(-1, -10, 4)$ .

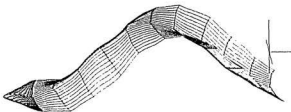


Figure B.45: Wake and its path of a fin whale's flukes with a spanwise deflexion at  $0^\circ$  phase angle. View point is at  $(-1, -10, 4)$ .



Figure B.46: Wake and its path of a fin whale's flukes with a spanwise deflexion at  $60^\circ$  phase angle. View point is at  $(-1, -10, 4)$ .



Figure B.47: Wake and its path of a fin whale's flukes with a spanwise deflexion at  $120^\circ$  phase angle. View point is at  $(-1, -10, 4)$ .

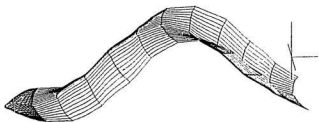


Figure B.48: Wake and its path of a fin whale's flukes with a spanwise deflexion at  $180^\circ$  phase angle. View point is at  $(-1, -10, 4)$ .

## Bibliography

- [1] Ahmadi, A.R. and Widnall, S.E. (1986). "Energetics and optimum motion of oscillating lifting surfaces of finite span," *J. Fluid Mech.*, vol. 162, pp. 261 – 282.
- [2] Ahmadi, A.R. and Windall, S.E. (1985). "Unsteady lifting-line theory as a singular perturbation problem," *J. Fluid Mech.*, Vol. 153, pp. 51 – 80.
- [3] Abramowitz M. and Stegun, I.A. (1970). *Handbook of mathematical functions*, Dover publications, Inc., New York, 1046 p.
- [4] Arsuffi, D. Guj, G. and Morino, L. (1989). "BEM for the analysis of unsteady aerodynamics of windmill rotors in the presence of yaw," Rotary-wing Aerodynamics, *Proceedings of the International Symposium on Boundary Element Methods: Advances in Solid and Fluid Mechanics*, East Hartford, Connecticut, pp. 169 – 178.
- [5] Ashby, D., Dubley, M. and Iguchi, S. (1988). "Development and validation of an advanced low-order panel method," NASA TM-101024, October, 44p.
- [6] Ashley, H. (1968). "Subsonic oscillatory or steady airloads on wings with control surface and other discontinuities," *Dept. of Aeronautics and Astronautics*, Stanford University, AFOSR – 68 – 0419, 46 p.
- [7] Atta, E.H., Kandil, O.A., Mook, D.T. and Nayfeh, A.H. (1976). "Unsteady flow past wings having sharp-edge separation," *Vortex-lattice Utilization*, Langley Research Center, Hampton, Virginia, pp. 407 – 421.
- [8] Bainbrige, R. (1958). "The speed of swimming of fish as related to size and to the frequency and amplitude of the tail beat," *J. Exp. Biol.*, Vol. 35, pp. 109 – 133.
- [9] Bose, N. and Lien, J. (1990). "Energy absorption from ocean waves: a free ride for cetaceans," *Proc. R. Soc. Lond. B240*, pp. 591 – 605.
- [10] Brett, J.R. (1964). "The respiratory metabolism and swimming performance of yawing sockeye salmon," *J. Fish. Res. Bd. Canada*, Vol. 21, pp. 1183 – 1226.

- [11] Browne, L. and Katz, J., "Application of panel methods to wind-tunnel wall interference corrections," AIAA Paper, No. 90-0007, January 1990, 7 p.
- [12] Carr, L.W., "Progress in analysis and prediction of dynamic stall," *AIAA Paper*, No. 85-1796, 1985, 17 p.
- [13] Casciola, C.M., Lancia, M.R. and Piva, R. (1989). "A general approach to unsteady flows in aerodynamics: Classical results and perspectives," *Unsteady Aerodynamics, Proceedings of the International Symposium on Boundary Element Methods: Advances in Solid and Fluid Mechanics*, East Harford, Connecticut, pp. 58 - 67.
- [14] Char, B.W., Geddes, K.O., Gonnert, G.H., Geong, B.L., Monagan, M.B., and Watt, S.M., *Maple V Language Reference Manual*, Springer-Verlag, New York, 1991, 267 p.
- [15] Cheng, H.K. and Murillo, L.E. (1984). "Lunate-tail swimming propulsion as a problem of curved lifting line in unsteady flow, Part 1, Asymptotic theory" *J. Fluid Mech.*, Vol. 143, pp. 327 - 350.
- [16] Chopra, M.G. (1976). "Large amplitude lunate-tail theory of fish locomotion," *J. Fluid Mech.*, Vol. 74, Part 1, pp. 161 - 182.
- [17] Commerford, D.L. (1974). "Unsteady aerodynamic response of a two-dimensional airfoil at high reduced frequency," *AIAA Journal*, Vol. 12, No. 1, pp. 43 - 48.
- [18] Crow, S.C. (1970). "Stability theory for a pair of trailing vortices," *AIAA Journal*, Vol. 8, No. 12, pp. 2172 - 2179.
- [19] Delaurier, J.D. and Harris, J.M. (1982). "Experimental study of oscillating-wing propulsion," *J. Aircraft*, Vol. 19, No. 5, pp. 368 - 373.
- [20] Dengler, M.A. and Goland, M. (1952). "The subsonic calculation of circulatory spanwise loading for oscillating airfoils by lifting line theory," *J. Aeronautical Sciences*, pp. 751 - 759.
- [21] Destuynder, R. and Tijdeman, H. (1973). "An investigation of different techniques for unsteady pressure measurements in compressible flow and comparison with lifting surface theory," *AGARD Report No. 617*, North Atlantic Treaty Organization, Advisory Group for Aerospace Research and Development, the 37th AGARD structures and materials panel meeting, The Hague, Netherlands, April 7-12, 1973, 29 p.
- [22] DeYong, J. (1976). "Historical evolution of vortex-lattice method," *Vortex-lattice Utilization*, NACA SP-405, N76-28163-N76-28168, Langley Research Center, Hampton, Virginia, pp. 1 - 9.

- [23] Edwards, J.M. (1988). "Computational unsteady aerodynamics for lifting surfaces," *VKI Lecture Series: Computational Fluid Dynamics*, Vol. 2, von Kármán Institute for Fluid Dynamics, Rhode-Stgenese, Belgium, 119 p.
- [24] Eskinazi, S. (1968). *Principles of Fluid Mechanics*, Second edition, Allyn and Bacon, Inc., 538 p.
- [25] Fleeter, S. (1979). "Trailing edge condition for unsteady flows at high reduced frequency," AIAA Paper, No. 79-0152, January, 6 p.
- [26] Fung, Y.C. (1945). *An introduction to the theory of aeroelasticity*, 1969 edition, Dover publications, Inc., New York, 498 p.
- [27] Garner, H.C., Hewitt, B.L. and Labrujere, F.E. (1969). "Comparison of three methods for the evaluation of subsonic lifting-surface theory," *Aeronautical Research Council Report and Memoranda*, No. 3597, Ministry of Technology, London, 41 p.
- [28] Guernond, J.L. and Sellier, A. (1990). "A unified unsteady lifting-line theory," *C. R. Acad. Sci.*, Paris, t. 311, Série II, pp. 21 - 26.
- [29] Guernond, J.L. (1988). "About collocation methods for marine propeller design," *The Society of Naval Architects and Marine Engineers*, Sept., 1988, pp. 8.1 - 8.9.
- [30] Harvald, S.A. (1983). *Resistance and propulsion of ships*, John Wiley & Sons, Inc., New York, 353 p.
- [31] Hedman, S.G. (1965). "Vortex-lattice method for calculation of quasi-steady state loadings on thin elastic wings in subsonic flow," *Flygtekniska Försöksanstalten*, Meddelande 105, Stockholm, 17 p.
- [32] Hertel, H. (1963). *Structure-form-movement*, Reinhold Publishing Co., New York, 251 p.
- [33] Hertel, H., (1968). "Biotechnique of oscillating propulsors system and their integration into the body," *Chapter 5-1, AGARD Principles and Practice of Bionics*, Technische University, Berlin, pp. 341 - 369.
- [34] Hess, J.L. (1990). "Recent advances in surface panel methods with emphasis on propeller problems," *Advances in boundary elements methods in Japan and USA*, ed. M. Tanaka, C.A. Brebbia and R. Shaw, Computational Mechanics Publications, Boston, pp. 253 - 268.
- [35] Hoerner, Dr.-Ing. S. F. and Borst, H.V., *Fluid-dynamic lift*, second edition, published by Hoerner, L.A., Albuquerque, N.M., 1985, 488 p.
- [36] International Business Machines Corporation, *Program guide*, VS Fortran version 2, 1987, 606 p.

- [37] International Business Machines Corporation, *Language and library reference*, VS Fortran version 2, 1987, 595 p.
- [38] Jones, R.J. (1940). "The unsteady lift of a wing of finite aspect ratio," *National Advisory Committee for Aeronautics*, Report No. 681, 9 p.
- [39] Küessner, H.G. (1954). "A general method for solving problems of the unsteady lifting surface theory in the subsonic range," *J. of Aeronautical Science*, pp. 17 - 27.
- [40] Kálmán, T.P., Gicsing, J.P. and Rodden, W.P. (1970). "Spanwise distribution of induced drag in subsonic flow by the vortex lattice method," *J. Aircraft*, Vol. 7, pp. 574 - 576.
- [41] Kamemoto, K. and Suzuki, T. (1989). "A vortex, method for predicting unsteady flow and boundary layer development around an airfoil," *Unsteady Aerodynamics, Proceedings of the International Symposium on Boundary Element Methods: Advances in Solid and Fluid Mechanics*, East Hartford, Connecticut, pp. 51 - 57.
- [42] Karpouzian, G., Spedding, G. and Cheng, H.K. (1990). "Lunate-tail swimming propulsion. Part 2. Performance analysis," *J. Fluid Mech.*, vol. 210, pp. 329 - 351.
- [43] Katz, J. and Weihs, D. (1981). "Wake rollup and the Kutta condition for airfoils oscillating at high frequency," *AIAA Journal*, vol. 19, No. 12, Technical Notes, AIAA 81-4329, pp. 1604 - 1606.
- [44] Katz, J. and Weihs, D. (1978). "Hydrodynamic propulsion by large amplitude oscillation of an airfoil with chordwise flexibility," *J. Fluid Mech.*, Vol. 88, part 3, pp. 485 - 497
- [45] Kelly, H.R., Rentz, A.W. and Seikmann, J. (1964). "Experimental Studies on the motion of a flexible hydrofoil," *J. Fluid Mech.*, Vol. 19, Part 1, pp 30 - 49.
- [46] Kubota, A., Kudo, T., Kato, H. and Yamaguchi, H. (1984). "Study on propulsion by partially elastic oscillating foil (2nd Report)," *Read at the Meeting of the Society of Naval Architects of Japan*, Fall, pp. 92 - 101.
- [47] Kwon, O.J. and Hodges, D.H. (1989). "Application of panel method aerodynamics to rotor aeroelasticity in hover," *AIAA Paper*, No. 89-1234, pp. 670 - 681.
- [48] Lai, P.S.K., McGregor, R.C. and Bose, N. (1989). "Experimental investigation of oscillating foil propellers," *22th American towing tank conf.*, ATTC conf., St. John's. Newfoundland, Canada., 7 p.
- [49] Lan, C.E. (1975). "The induce drag of oscillating airfoils in linear subsonic compressible flow," *KU - FRL - 400*, Kansas, 60 p.

- [50] Lai, P.S.K., McGregor, R.C. and Bose, N. (1989). "On the flexible fin propeller," *4th International symp. on practical design of ships & mobile units*, Bulgarian Ship Hydrodynamic Center, PRADS, VARNÁ, 8 p.
- [51] Lamarre, F. and Paraschivoiu, I. (1991). "Efficient panel method for vortex sheet roll-up," *J. Aircraft*, Vol. 29, No. 1, pp. 28 - 33.
- [52] Lan, C.E. (1976). "Some application of the quasi-vortex-lattice method in steady and unsteady aerodynamics," *Vortex-lattice Utilization*, Langley Research Center, Hampton, Virginia, pp. 385 - 406.
- [53] Lan, C.E. and Lamar, J.E. (1977). "On the logarithmic-singularity correction in the kernel function method of subsonic lifting-surface theory," NASA, TN, D - 8513, 53 p.
- [54] Landhal, M.T. (1966). "Kernel function for nonplanar oscillating surface in a subsonic flow," *AIAA J.* Vol. 5, No. 5, pp. 1045 - 1046.
- [55] Lawrence, H.R. and Gerber, E.H. (1952). "The aerodynamic forces on low aspect ratio wings oscillating in an incompressible flow," *J. of Aeronautical Science*, pp. 699 - 781.
- [56] Le Méhauté, B. (1976). *Introduction to Hydrodynamics and Water Waves*, Springer-Verlag, New York, 315 p.
- [57] Liebeck, R.H. (1973). "A class of airfoils designed for high lift in incompressible flow," *J. Aircraft*, Vol. 10, No. 10, pp. 610 - 617.
- [58] Liebeck, R.H. (1978). "Design of subsonic airfoils for high lift", *J. Aircraft*, Vol. 15, No. 9, pp. 547 - 561.
- [59] Lighthill, M.J. (1960). "Note on the swimming of slender fish," *J. Fluid Mech.*, Vol. 9, pp. 305 - 317.
- [60] Lighthill, M.J. (1970). "Aquatic animal propulsion of high hydromechanical efficiency," *J. Fluid Mech.* Vol. 44, pp. 256 - 301.
- [61] Luis, R.M. (1982). "A perspective of computational aerodynamics from the viewpoint of airplane design applications," *AIAA Paper*, No. 82-0018, 17 p.
- [62] Mastroddi, F. and Morino, L. (1989). "Time and frequency domain aerodynamics for flutter and helicopter rotors in hover," *Rotary-wing Aerodynamics, Proceedings of the International Symposium on Boundary Element Methods: Advances in Solid and Fluid Mechanics*, East Hartford, Connecticut, pp. 8 - 14.
- [63] McCroskey, W.J. (1981). "The phenomenon of dynamic stall," *NASA TM*, No. 81264, 27 p.
- [64] McCroskey, W.J. (1982). "Unsteady airfoil," *Ann. Rev. Fluid Mech.*, 14 : 285 - 311.

- [65] McGroskey, W. J., McAlister, K. W., Carr, L. W., Pucci, s. L., Lambert, O., and Indergrand, R.F. (1981). "Dynamic stall on advanced airfoil sections," *Journal of the American Helicopter Society*, July, pp. 40 - 50.
- [66] Merbt, H. and Landahl, M. (1953). "Aerodynamic forces on oscillating low aspect ratio wing in compressible flow," *Technical Report, Royal Institute of Technology*, Division of Aeronautics, Stockholm 70, Sweden, 30 p.
- [67] Ohmi, K., Coutanceau, M., Loc, T.P. and Dulieu, A. (1990). "Vortex formation around an oscillating and translating airfoil at large incidence," *J. Fluid Mech.*, Vol. 211, pp. 37 - 60.
- [68] Ruyaan, H.L. and Woolston, D.S. (1957). "Method for calculating the aerodynamic loading on an oscillating finite wing in subsonic and sonic flow," *National Advisory Committee for Aeronautics*, Report No. 1322, 30 p.
- [69] Sarpkaya, T. (1989). "Computational methods with vortices-The 1988 Freeman Scholar Lecture", *Journal of Fluids Engineering*, Vol. 111, pp. 5 - 52.
- [70] Satyanarayna, B. and Davis, S. (1978). "Experimental studies of unsteady trailing edge conditions", *AIAA Journal*, Vol. 16, No. 2, pp. 125 - 129.
- [71] Scherer, J.O. (1968). "Experimental and theoretical investigation of large amplitude oscillating foil propulsion systems," U.S. Army Engineering Research and Development Laboratories, *DA - 44 - 009 - amc - 1759(t)*, 56 p.
- [72] Shen, S.F. (1953). "Effect of structural flexibility on aircraft loading, part X - A new lifting-line theory for the unsteady lift of a swept or unswept wing in an incompressible fluid," *U.S. Air Force Material Command: Air Force Technical Rept.*, No. 6538, 41 p.
- [73] Shevell, R.S. (1983). *Fundamentals of Flight*, Prentice-Hall, Inc., Englewood Cliffs, N.J., U.S.A., 405 p.
- [74] Smith, A.M.O. (1975). "High lift aerodynamics", *J. Aircraft*, Vol. 12, No. 6, pp. 501 - 530.
- [75] Watkins, C.E., Woolston, D.S. and Cunningham, H.J. (1959). "A systemic kernel function procedure for determining aerodynamic forces on oscillating or steady finite wings at subsonic speed," *National Aeronautics and Space Administration*, Technical Report *R - 48*, 21 p.
- [76] Wilmott, P. (1988). "Unsteady lifting-line theory by the method of matched asymptotic expansions," *J. Fluid Mech.*, vol. 186, pp. 303 - 320.
- [77] Woodward, F.A., Tinoco, E.N., and Larsen, J.W. (1967). "Analysis and design of supersonic wing-body combinations, including flow properties in the near field," Part I-theory and application, *NACA CR - 73106*, pp. 219 - 221.

- [78] Wu, T.Y. (1972). "Extraction of flow energy by a wing oscillating in waves," *J. Ship Research*, March, 1972, pp. 66 – 78.
- [79] Yates, E.C. (1966). "A kernel function formulation for nonplanar lifting surfaces oscillating in subsonic flow," *AIAA J.* Vol. 4, No. 8, pp. 1486 – 1488.







